A Trojan horse route to emergent active and stable platinum nanoparticles from a perovskite system

Maadhav Kothari

A thesis submitted for the degree of PhD
at the
University of St Andrews

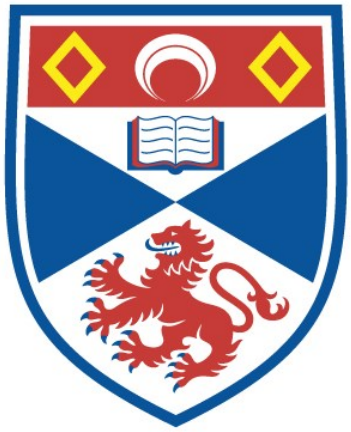

2021

Candidate's declaration

I, Maadhav Kothari, do hereby certify that this thesis, submitted for the degree of PhD, which is approximately 30,000 words in length, has been written by me, and that it is the record of work carried out by me, or principally by myself in collaboration with others as acknowledged, and that it has not been submitted in any previous application for any degree. I confirm that any appendices included in my thesis contain only material permitted by the 'Assessment of Postgraduate Research Students' policy.

I was admitted as a research student at the University of St Andrews in September 2015.

I received funding from an organisation or institution and have acknowledged the funder(s) in the full text of my thesis.

Date 10/06/2021 Signature of candidate

Supervisor's declaration

I hereby certify that the candidate has fulfilled the conditions of the Resolution and Regulations appropriate for the degree of PhD in the University of St Andrews and that the candidate is qualified to submit this thesis in application for that degree. I confirm that any appendices included in the thesis contain only material permitted by the 'Assessment of Postgraduate Research Students' policy.

Date Signature of supervisor

Permission for publication

In submitting this thesis to the University of St Andrews we understand that we are giving permission for it to be made available for use in accordance with the regulations of the University Library for the time being in force, subject to any copyright vested in the work not being affected thereby. We also understand, unless exempt by an award of an embargo as requested below, that the title and the abstract will be published, and that a copy of the work may be made and supplied to any bona fide library or research worker, that this thesis will be electronically accessible for personal or research use and that the library has the right to migrate this thesis into new electronic forms as required to ensure continued access to the thesis.

I, Maadhav Kothari, confirm that my thesis does not contain any third-party material that requires copyright clearance.

The following is an agreed request by candidate and supervisor regarding the publication of this thesis:

Printed copy

No embargo on print copy.

Electronic copy

No embargo on electronic copy.

Date 10/06/2021 Signature of candidate

Date Signature of supervisor

Underpinning Research Data or Digital Outputs

Candidate's declaration

I, Maadhav Kothari, understand that by declaring that I have original research data or digital outputs, I should make every effort in meeting the University's and research funders' requirements on the deposit and sharing of research data or research digital outputs.

Date 10/06/2021 Signature of candidate

Permission for publication of underpinning research data or digital outputs

We understand that for any original research data or digital outputs which are deposited, we are giving permission for them to be made available for use in accordance with the requirements of the University and research funders, for the time being in force.

We also understand that the title and the description will be published, and that the underpinning research data or digital outputs will be electronically accessible for use in accordance with the license specified at the point of deposit, unless exempt by award of an embargo as requested below.

The following is an agreed request by candidate and supervisor regarding the publication of underpinning research data or digital outputs:

Embargo on underpinning research data or digital outputs.

Date 10/06/2021 Signature of candidate

Date Signature of supervisor

TABLE OF CONTENTS

Table of Contents

ABSTRACT

Platinum (Pt), generally dispersed on a solid oxide support, has been widely used for catalytic chemical reactions in automobile, petroleum and energy industries. During the reactions, Pt is exposed to severe conditions, for example, heat and impurities, that cause Pt agglomeration and poisoning, respectively, resulting in activity/stability decrease [1-2]. Here, perovskite materials are designed with Pt for significant catalytic properties through novel doping and exsolution methods.

Perovskite structured materials (ABO_3) are selected because these are basically stable at heat and redox environments with coke/sulfur resistances at the catalytic or electrochemical conditions [3]. When perovskite oxides are employed as supporting frameworks, certain catalysts like Pt can be incorporated as cations on the B site of the perovskite lattice under oxidizing conditions (*doping*). By tailoring the stoichiometry of the doped perovskite materials, the dopants can be partly exsolved as nanoparticles (NP) on subsequent reductions, which provides the possibility of the in situ growth of NP (*emergence*) [4-5]. As shown in Figure 1, this method can improve the catalytic property of Pt by less loading, proper size, high dispersion, unique active sites and strong bonding structure with the perovskite.

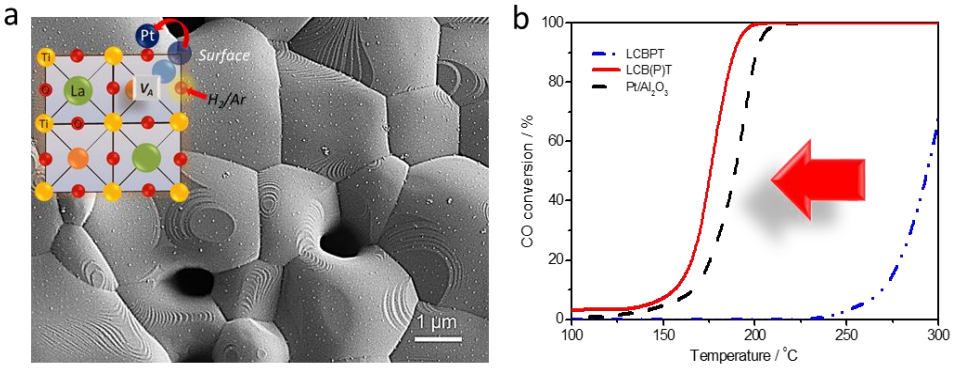

Figure 1: (a) SEM image on Pt emerged on perovskite catalyst, LCB(P)T, and (b) its catalytic applications on CO oxidations.

Because only a few studies have been carried out due to the difficulty in the handling of Pt, the goal is to develop an innovative Pt perovskite catalyst to use in various catalytic applications.

References

Y. Nie, L. Li, Z. Wei, *Chem. Soc. Rev.*, 2015, 44, 2168-2201

[1] J. Jones, H. Xiong, A.T. DeLaRiva, E.J. Peterson, H. Pham, S.R. Challa, G. Qi, S. Oh, M.H. Wiebenga, X.I.P. Hernández, Y. Wang, A.K. Datye, *Science*, 2016, 353, 150–154.

[2] J. Hwang, R.R. Rao, L. Giordano, Y. Katayama, Y. Yu, Y. Shao-Horn, *Science*, 2017, 358, 761–756.

[3] D. Neagu, G. Tsekouras, D. N. Miller, H. Menard, J.T.S. Irvine, *Nat. Chem.*, 2013, 5, 916–923.

[4] J. Myung, D. Neagu, D. N. Miller, J.T.S. Irvine, *Nature*, 2016, 537, 528–531.

ACKNOWLEDGEMENTS

This Thesis is dedicated to Dr David Wails my industrial supervisor (Johnson Matthey) who tragically in the summer of 2020 was taken from our community by an act of cowardice and murder by an extremist. His memory will not be forgotten and we as scientists will strive to always better ourselves, find the truth and encourage acceptance and progress within society. David you were a brilliant scientist. Your endeavours will not be forgotten.

I would like to thank Professor John Irvine for his excellent support throughout the project and for giving me the opportunity to study within his esteemed group, without whom I would not have pushed myself to investigate scientific principals and novelties and would have most certainly not had the confidence to question and explore materials chemistry.

Special thanks must be given to Dr Yukwon Jeon for his brilliance, advice as well as consistent collaboration and dialogue throughout the project.

Thank you also to David Miller for teaching me how to use the Microscopy suite to its full extent. Thanks to Janet Fischer and David Wails from JM for their continued input into this project. Thanks to Andrea Pascui and Jhon Kilmartin from JM for help with catalysis experiments. Thanks to Professor Alan Chadwick and Dr Silvia Ramos for their continued help with XANES/EXAFS, support within Diamond and teaching me core principals.

Thank you to my parents, family and Monty the dog for everything they have done to help me achieve my full potential.

Finally, thank you to the EPSRC for an industrial CASE scholarship with Johnson Matthey.

CONTRIBUTIONS

Dr David Wails and Dr Janet Fisher for guidance at Sonning Common

Dr David Miller for TEM and SEM guidance and teaching me how to use the instruments

Dr Silvia Ramos for teaching XANES/EXAFS fitting on Athena

Prof. Alan Chadwick for advice and running B18 Bag Run samples alongside Dr Gianantonio Cibini

Prof. John Irvine for consistent comment contribution and dedication to the project

Dr Yukwon Jeon for catalytic knowledge, setting up MFC controllers and GC-MS calibration

Ms. Candice Mitchell for all her endeavours and help with administrative tasks.

ABBREVIATIONS AND NOMENCLATURE

XRD- X-ray diffraction

PXRD- Powder X-ray diffraction

SEM- Scanning Electron Microscopy

HR-TEM-High Resolution Transmission Electron Microscopy

XANES- X-ray near edge absorption spectra

EXAFS X-ray extended edge absorption spectra

TGA- Thermogravimetric analysis

CO:NO- Carbon monoxide: Nitrous Oxide

CO- Carbon monoxide

NH_3- Ammonia

$Ba_3Pt_2O_7$- Barium Platinate

DOC- Diesel Oxidation Catalysis

TWC- Three Way Catalysis

CO-DRIFT- Carbon monoxide-diffuse reflectance infrared Fourier transform spectroscopy

NP- Nanoparticle

NP's- Nanoparticles

Pt- Platinum

Pt@LCT- A-site deficient perovskite of $La_{0.4}Ca_{0.3925}Ba_{0.0075}Pt_{0.005}Ti_{0.995}O_3$

Pt@LST- A-site deficient perovskite of $La_{0.4}Sr_{0.3925}Ba_{0.0075}Pt_{0.005}Ti_{0.995}O_3$

Pt+LCT Reduced A-site deficient perovskite of $La_{0.4}Ca_{0.3925}Ba_{0.0075}Pt_{0.005}Ti_{0.995}O_3$

Pt+LST Reduced A-site deficient perovskite of $La_{0.4}Sr_{0.3925}Ba_{0.0075}Pt_{0.005}Ti_{0.995}O_3$

LCT non doped $La_{0.4}Ca_{0.3925}Ba_{0.0075}TiO_3$

LST- non doped $La_{0.4}Sr_{0.3925}Ba_{0.0075}TiO_3$

LBST- $La_{0.2}Ba_ySr_{0.7-y}TiO_3$

Pt/Al_2O_3- Platinum on Alumina

$Pt/\gamma Al_2O_3$- Platinum on gamma Alumina

CHAPTER 1 BACKGROUND

1.1 The global energy context

A greener future

A more sustainable and greener world is necessary in order to combat climate change and the ever-increasing demand on finite resources, such as fossil fuels, as well as an increasing global human population.[1–3] As the consumption of fossil fuels has increased over the last millennium, the resultant amount of CO_2 due to the combustion of hydrocarbons has been released (as shown in Fig. 1-1), resulting in a global warming of the climate.[4] The energy demand must be met through the use of renewable energy and improved chemical processes through catalysis.

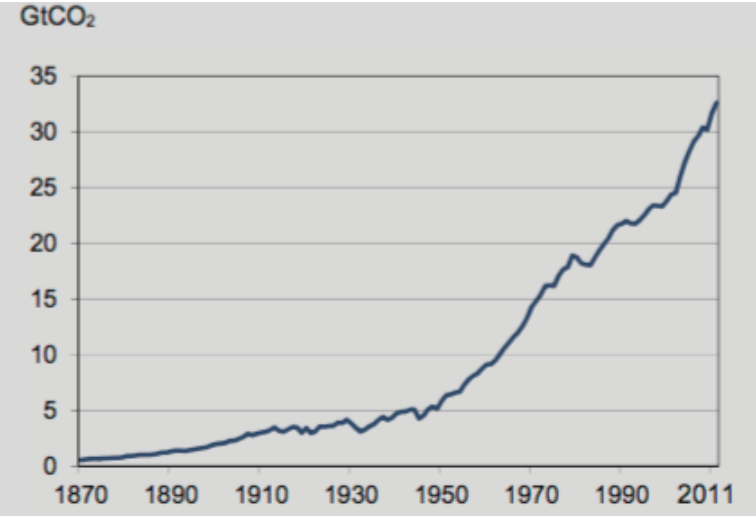

Figure 1-1 shows an exponential rise in CO_2 emissions[1].

In order to meet such increased demand, it is necessary to develop new catalysts and catalytic technologies that can remediate current challenges by rational design of novel catalysts. By following a few rules for catalytic design of exsoluting perovskite, it should be possible to tailor the catalyst for the desired reactions. The current focuses on shifting overall energy

consumption away from fossil fuels to renewable alternatives, such as biofuels, wind and solar energy, is progressing rapidly, however, this requires additional technological development in order to be price-competitive with current energy alternatives, such as oil, coal and natural gas.[5] Industrially, exsoluting perovskite catalysts have the ability to provide not only a cheaper alternative, but also a greener solution for many mixed-oxide-based catalytic reactions. This is due to the incorporation of cheaper ceramic bulk and the use of less (weight) costly transition metals such as platinum and nickel. Possible applications include the oxidation of methanol and ammonia over platinum and silver, the possibility to compete with acidic-alumina-silica-based materials such as zeolites and the potential use in automotive catalysis, which demonstrate that a valuable opportunity lies in this research.

1.2 Automotive catalysis; Diesel and gasoline

A brief history of automotive catalysis

The 1970 clean air act (CAA) in the USA kick-started a revolution in automotive emissions control technology. The requirement to reduce hydrocarbon (HC), carbon monoxide (CO) and, later, nitrous oxide (NO_x) polluting gasses was imposed upon car companies and catalyst manufactures to solve the growing pollution crisis in California at the time. By 1974, gasoline vehicles were fitted with two-way catalytic converters for CO and unburnt HC[67]. Further regulation required NO_x to be removed in 1979, which was done by coupling two monoliths in series: the first in lean conditions reducing NO_x in a fuel rich atmosphere followed, by a second monolith with an excess of air resulting in rich (oxidising) conditions to catalyse CO and HC's.

Typically, Pd was used as the NO_x reducing catalyst in the early days; however, it was found that Rh was more suited for NO_x reduction.

By 1983, three-way catalytic converters (TWC) were introduced, and the use of lead-free (antiknock agent tetraethyl) fuel was more widespread, resulting in better catalytic performance and the ability for NO_x, CO and HC to be catalysed in fluctuating rich and lean conditions, rather than just lean environments[6]. The introduction of PO_2 and fuel injection control sensors enables the air-to-fuel ratio to be controlled, allowing for optimum catalytic conditions. Noble metals Pd and Pt were initially chosen due to their ability to catalyse CO, HC and NO_x at lower temperatures and their ability to catalyse all components of pollutants. Early catalytic converters were a distribution of high wt% up to 5%wt noble metals (Pt/Pd) on alumina pellets or a monolith, and although the concept of the catalytic converter itself has not changed, consistent improvements and technological developments have resulted in better efficiency and considerable advancements in reducing all forms of pollutants from exhaust streams[8–10].

Diesel vehicles also required catalytic converters, although they were different in design. In the early 1960s, diesel forklift trucks, mining equipment and even ice rink scrubbers were fitted with PTX (exhaust purifiers), which were early crude Pt/Al_2O_3 coated monolith[7,11,12]. Due to the nature of combustion, diesel vehicles operated at lower temperatures and emitted CO, NO_x SO_2, HC and particulate matter (PM, also known as soot). Diesel engines operate under rich conditions, thus resulting in higher O_2 concentrations in the exhaust gas. Using a TWC is ineffective for this gas stream due in part to the concentration of PM, HC and O_2. The introduction of oxidation catalysts in the early 1990s resulted in the ability to control CO and HC, and furthermore, in the early 2000s, the development of particulate filters and NO_x removal resulted in further emissions reduction from diesel exhaust streams[13,14].

Automotive catalysis is a major user of PGM (platinum group metals), and in 2018, $25 billion of Pt, Pd and Rh were used within the industry[15]. The motivation to use less PGM stems from the metal scarcity, pricing and projected increase in automobile usage. The increasing use of automobiles, the growing world population and government and market demands for stringent emissions controls have resulted in an increase in demand for the precious metals and their uses as catalysts.

Catalyst support and their interaction with PGMs

As catalysis of exhaust gas occurs on the surface of dispersed metal particles on a support coated to a monolith, metal particles within the bulk are unable to catalyse any reaction and are therefore wasted. This is also enhanced by the effect of coarsening and the possible coalescence of two metal particles moving and joining together over time, resulting in a loss in activity. Due in part to the nature of noble metals reducing and thermodynamically driven coarsening resulting in a loss of activity through reduced surface area and changes in oxidation makeup of metallic nanoparticles, the industry has aimed to reduce the amount of noble metals used and deploy thermally stable and chemically favourable support materials to aid in the catalysis of CO, NO_x, HC and PM.

A typical catalyst support material is made up of a refractory oxide such as γ-Al_2O_3 which has strong sintering resistant properties, a high surface area and is able to operate under harsh conditions and redox environments. The transformation of γ-Al_2O_3 to α-Al_2O_3 occurs at between 875-1000°C, with the latter having a lower surface area. In order to mitigate this, the addition of stabilising mixed oxides are added, such as LaO_2, BaO_2, ZrO_2 and CeO_2[13,16].

By tailoring the perovskite mixed oxide stoichiometry, it is possible to create an anchored, evenly dispersed metal. It is no surprise, therefore, automotive companies such as Daihatsu,

GM and Johnson Matthey are heavily investigating the development of novel perovskite-based automotive three-way catalysts[17–19].

Gasoline exhaust catalysis; Three-way catalytic converter (TWC)

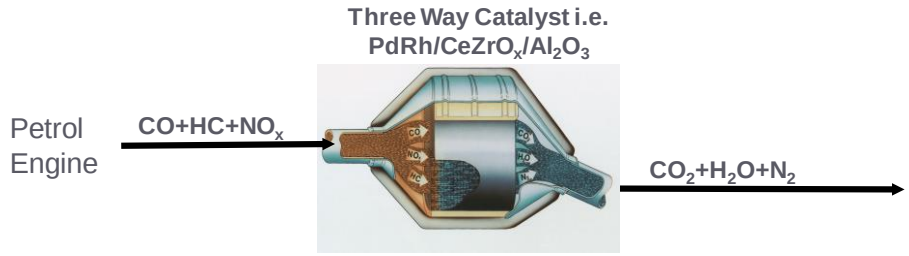

Figure 1-2 shows the gas components of a petrol engine, the mixed oxide material primarily used in TWC converters (Pd, Rh) and their substrate support material such as oxygen storage support $CeZrO_x$ and Al_2O_3

A TWC is comprised active metal nanoparticles (0.2-0.5 wt.%) Pd/Rh supported on rugous Al_2O_3 or CeO_2/ZrO_2 wash coated onto a cordierite monolith and then sealed in a housed metallic container. A typical operating temperature is between 400-800°C. Three catalytic conversions are taking place simultaneously in a lambda-operated TWC:

$$\text{CO oxidation over Pt/Pd: } 2CO(g) + O_2(g) \rightarrow 2CO_2(g)$$

$$\text{Hydrocarbon oxidation over Pt/Pd: } C_8H_{18}(g) + 12½O_2(g) \rightarrow 8CO_2(g) + 9H_2O(g)$$

$$\text{NO reduction (CO) over Rh: } 2NO(g) + 2CO(g) \rightarrow N_2(g) + 2CO_2(g)$$

In TWC for the gasoline exhaust stream, CeO_2 is used as a support material for Pd-supported metal nanoparticles and acts as an oxygen storage support capacity (OSC). The CeO_2 support provides a larger stochiometric operating range by increasing the air-to-fuel equivalence ratio and provides an oxygen environment during rapid redox cycles as shown in Figure 1-3. CeO_2 combined with ZrO_2 (up to 30%) can provide extended thermal stability and increase oxygen storage capacity.

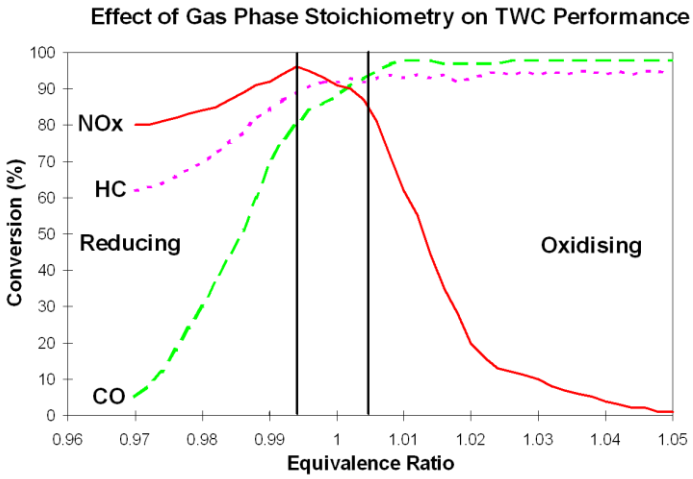

Figure 1-3: The operating ratio of a TWC converter is increased significantly with the addition of $CeZrO_x$ allowing the conversion of NO_x, HC and CO in more reductive conditions. This is due to the oxygen storage properties of the substrate.

Diesel exhaust catalysis

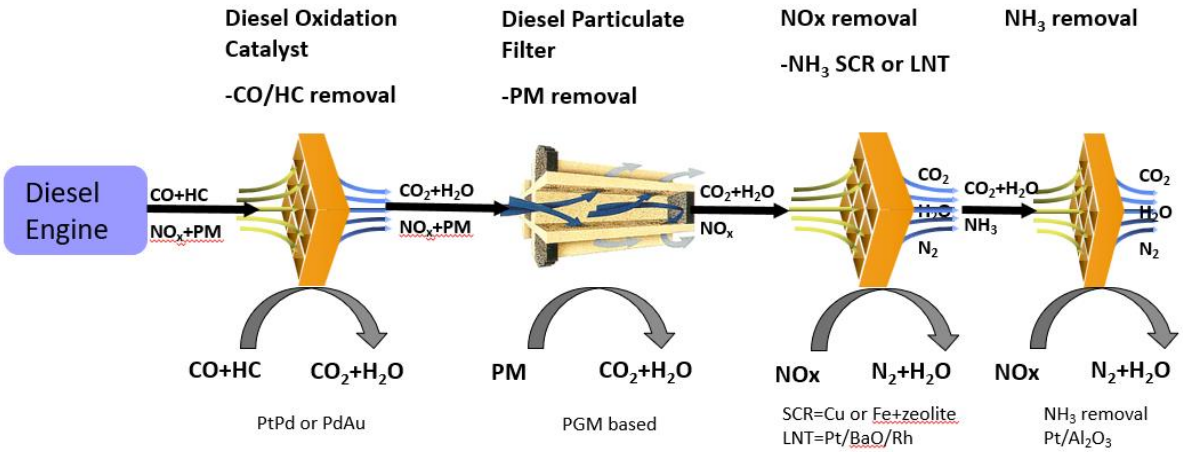

Figure 1-4: An overview of a diesel catalytic system with four major components, the diesel oxidation unit, the diesel particulate filter, NO_x removal and NH_3 removal.

A diesel exhaust operates under rich conditions, a higher equivalence ratio and a lower temperature in comparison to a gasoline exhaust. This poses its own problems for successful catalytic conversion of gasses, such as more PM. For a diesel exhaust aftertreatment, a TWC would be ineffective due to the O_2-rich exhaust gas environment, as low O_2 is required in order to reduce NO_x. If the fuel were to be fully combusted, there would therefore be an increased production of NO_x in a tailored autocat system a trade off on total combustion of the fuel under heavy loads is restricted to reduce NO_x.

Firstly, a diesel oxidation (DOC) catalyst comprised of Pd/Pt or Pd/Au acts as an oxidising catalyst, operating between 180-300°C, catalysing CO and some HC due to the incomplete combustion of the fuel. Secondly, a diesel particulate filter (DPF) comprised of $Pt/Pd/BaCO_3$ removes unburnt HC at a high temperature (700-900°C). Thirdly, a selective catalytic reduction unit (SCR) removes NO_x by reduction with either NH_3 over a Cu zeolite or $Pt/BaO/Rh\text{-}\gamma Al_2O_3$ (the selection of which is usually dependant on the engine size). Finally, if NH_3 has been used, an ammonia slip unit (ACS) is required to remove excess NH_3 that has not been fully catalysed.

For DOC, Pt and Pd bimetallic, or a combination of both metals, are used on γAl_2O_3 in order to facilitate both NO_x oxidation over Pt and CO conversion over Pd. A certain amount of NO_2 is needed in the second DPF stage in order to facilitate the catalysis of carbon in a passive regeneration step[20].

Carbonaceous soot particles are caught onto the porous monolith of the DPF whilst still allowing hot gas to flow through interpore channels within the monolith. Both Pd and Pt are deployed to catalyse the same reactants as the DOC and DPF. Due to the harsh temperature range and pressures in the DPF, the design of the monolith and the washcoat are important factors in controlling consistent catalytic activity. Carbonaceous soot particles are catalysed in

an oxidation reaction with N_2O, and therefore the DOC step is critical to keeping a good pressure of N_2O in order to correctly catalyse carbon soot particles.

Ad-blue, Blue-tec, and Blue-motion are all commercial names for the same reaction[21]. The selective catalytic reduction of NO_x to N_2 takes place with the help of NH_3 as the reactant over a Cu chabazite (zeolite) catalyst. There are multiple reactions occurring in an SCR, and it is important for the ratio of NO to NO_2 to be 1:1.

DOC:

$$CnH_2m + (n + ½ m)\ O_2 \rightarrow nCO_2 + mH_2O$$

$$CO + ½O_2 \rightarrow CO_2$$

$$NO + ½\ 2O_2 \rightarrow NO_2$$

DPF:

$$NO_2 + C \rightarrow CO + NO$$

SCR:

$$4NO + 4NH_3 + O_2 \rightarrow 4N_2 + 6H_2O$$

$$6NO_2 + 8NH_3 \rightarrow 7N_2 + 12H_2O$$

$$NO + NO_2 + 2NH_3 \rightarrow 2N_2 + 3H_2O$$

Nanoparticle stabilisation

The interaction between metallic nanoparticle and oxide support is crucial to automotive catalysis. In order for catalysis to take place effectively, a nanoparticle must remain a nanoparticle and the support must stay as it is without degradation to the structure. A catalytically active nanoparticle must either be firmly embedded within the support material or pinned by a specific contact angle in order to prevent coarsening and the movement of

nanoparticles toward one another, forming large agglomerations and therefore losing surface area or being lost from the support material entirely. A strong physical interaction between nanoparticle and oxide support is necessary, but not one where the active nanoparticle loses its electronic and chemical properties to the supporting oxide, thus losing catalytic activity.

Ostwald ripening, coalescence and migration are the major coarsening mechanisms resulting in reduced catalytic activity. Nanoparticles, given enough thermal energy, will move toward one another and sinter, resulting in a reduced surface area and a larger agglomeration of metallic nanoparticles and reduced catalytic activity[22–24].

Otswald ripening is a thermodynamically driven process whereby an atom from a small nanoparticle redeposits upon another atom on a larger nanoparticle and grows each diffusion event, resulting in larger particles and smaller particles. Smaller nanoparticles in comparison to larger nanoparticles are less stable due to the higher surface area and radius of the curvature of the particles, thus resulting in more atoms diffusing and redepositing upon a larger, more favourable, particle. This eventually results in a cluster of lager particles rather than smaller nano-sized particles on the substrate. Single, unstable atoms known as adatoms are less stable and susceptible to movement due to the difference in free energy. Particle coalescence and migration are caused by the random movement of particles on the surface support material (migration), as well as the agglomeration of nanoparticles (coalescence).

The interaction of the support material upon metallic nanoparticles is important. There are two types of interaction: non-participating support and support-dependant. Non-participating support interaction results in a material that simply acts as a holder, or vessel, for a catalyst and plays no part in the stabilisation. Support-dependant not only acts as a holder or vessel, but is also modified by the nanoparticle either chemically or physically – for example, chemical atomic pinning or anchoring and embedding. Strong metal support interactions (SMSI) are an

example of chemical pinning. When reduced, TiO_1 is known to migrate to the surface and atomically form a protective oxide later around a metallic oxide nanoparticle, pinning it to the surface of the support. Pt-CeO_2 will also form a metallic oxide Pt-O-Ce bond that results in less migration of Pt nanoparticles in comparison to Al_2O_3.

PGM coordination and chemisorption

Platinum group metals exhibit excellent properties for certain catalysis, especially for automotive applications. The partially occupied 4d and 5d orbitals PGMs display certain catalytic traits for oxidation reactions, more so than other 3d-filled orbital noble metals, such as Ni, Co and Fe.

The Daihatsu intelligent catalyst

In 2001, Daihatsu Motor Corporation developed a stoichiometric $LaFe_{0.57}Co_{0.38}Pd_{0.05}O_3$ containing perovskite[25,26] with the ability to reversibly incorporate precious metal oxide palladium and precipitate Pd metal to the surface of the stoichiometric perovskite structure. This was coined 'the intelligent catalyst'[1–10], 'the self-regenerative catalyst'[3] and, later, 'the super intelligent catalyst'.[34] The intelligence of the catalysts comes from the reported ability of the host perovskite structure to precipitate Pd^0 to the surface of the crystalline perovskite host and, upon subsequent re-oxidation, the dissolution and burrowing of the same metallic particle to the bulk of the perovskite structure as an oxide form $Pd^{2\text{-}4+}$. This was revolutionary in the field, as the ability to prevent coarsening and Oswald ripening of catalytically active metallic nanoparticles is key to the longevity of automotive applications which are exposed to harsh temperature environments of up to 800°C and rapidly switching cyclical redox environments between lean and rich conditions, which lead to the degradation of catalytically active

nanoparticles. The interactions between the perovskite bulk, the support and the crystalline surface all play a vital role in the formation and dissolution of the PGM nanoparticles which do not form agglomerations nor disperse from the support, due to the strong metallic support interactions reported.

The preparation method of the materials was made through the co-precipitation of metal nitrate precursors through the alkoxide process, resulting in a crystalline powder. Characterisation and analysis of the data was mainly carried out by X-ray diffraction (XRD), X-ray absorption near-edge structure (XANES), extended X-ray absorption fine-structure (EXAFS) and X-ray photoelectron spectroscopy (XPS), with limited focus on structural behaviour through observing the microstructure with transmission electron microscopy (TEM) and scanning electron microscopy (SEM) microscopy. This showed the change in the oxidation state of the B site Pd cation from metallic Pd^0 to Pd^{4+} and Pd^{2+} with the transition between the surface and the bulk and back again after multiple redox cycles under simple air ageing conditions. In summary, the mechanism reported showed that Pd exists on the B site upon preparation and oxidation in an ionic state between Pd^{2-4+} and, upon reduction, migrates to the surface of the material and exists as a metallic Pd^0 nanoparticle that is resistant to the effects of oxidative ageing. This results in a reversible stable nanoparticle on the surface of the crystalline perovskite, in stark comparison to the nature of Pd-Al_2O_3 which forms large agglomerations of Pd^0 in the same redox conditions.[32]

Later work focused on $LaFe_{0.95}Pd_{0.05}O_3$[30,31] which was found to have better crystallinity and catalytic activity than that of the previously reported Co-containing composition. A series of redox conditions[33,35] were tested. The oxidative dissolution of perovskite was reported at 400°C, and the redox activity of the Pd species was between 200-400°C ,a low temperature for oxidative metallic metamorphosis. Interestingly, the Pd bonding dynamic EXAFS revealed the

change from Pd-O bonding straight to Pd-Pd bonds instantly, within seconds of reduction. The interpretation of this result is difficult, as it would suggest a dynamic mechanism previously unknown whereby oxidised Pd can transform from the bulk of the perovskite to the surface, instantly forming dispersed metallic Pd^0 on the surface. The energetics of this process further need explaining, in order to instantly form nanoparticles from the bulk with a range of 20-100nm. To cover even for single cation diffusion would result in faster diffusion than the grain boundary or even surface transport and coarsening. Daihatsu then went to study the effect of Rh, Pd and Pt in $CaTiO_3$[36,37,38] with the same intelligent catalyst effect observed by primarily X-ray spectroscopy. Varying ratios of Rh, Pd and Pt were explored, cyclical ageing testing was carried out in air on $CaTi_{0.98}Pt_{0.02}O_3$ and reported cluster growth of the nanoparticles was no more than 3nm over 100hr in real engine exhaust conditions, compared to 100nm for Pt-Al_2O_3. Interestingly, $SrZrO_3$ and $BaZrO_3$ had an inability for Pt in a solid solution, Rh displayed an inability for $SrZrO_3$ and Pd had an inability for $CaTiO_3$. TEM images of Pt in the $CaTiO_3$ system do show definitive Pt particles within the host structure; however, the determination of whether they are in the bulk of the perovskite or the surface is dubious due to the nature of Pt molecular weight in comparison to $CaTiO_3$. Controversy surrounded the intelligent catalyst, and debate as to whether particles were actively moving in and out of the lattice was extensive. Recently work has been carried out by M.B.Katz,[39,40] which has strongly counteracted the theory of the intelligent catalyst. A comprehensive TEM study was carried out on all of Daihatsu's published intelligent perovskite materials.[41] Katz indicated that the Pd, Pt and Rh particles are not evenly dispersed on the surface of the catalyst after reduction and are not of the same size, resulting in apparent coarsening, which indicates that the redox effect of the nanoparticles and their movement between the bulk and surface is not instantaneous and prevalent. The process of reversibility was confirmed to a lesser extent;[40] however, it was

confirmed only upon the harsh reduction condition, which was found to increase particle stability due to an embedded cavity forming between the perovskite bulk and nanoparticle. Notably, the particle size of Pd ranged from 100-10nm rather than the reported 3nm. The mechanism itself has been reported to be a surface segregation whereby a dual phase exists, upon which the metallic B site cation exists (LaPdO3) about the perovskite bulk (LaFeO3), thus facilitating the diffusion of metallic nanoparticles to the surface over a shorter distance.[42]

Considering both cases, the dissolution of nanoparticles back and forth between the bulk and surface of the perovskite has been confirmed by both Katz and Tanaka. However, this is not throughout the crystal structure, and occurs only in sporadic clusters. It is a surface-activated interaction between perovskite and metallic nanoparticles, and the intelligence of the catalyst itself seems to be the sintering resistance of the nanoparticle clusters rather than its ability to kinetically diffuse between bulk and surface instantly. The reporting of surface rich PGM phases suggests that a segregation of catalytically active metal oxide and the reported particle size after redox treatment in air had been strongly contested.

1.3 Objectives of this dissertation

The objectives of this dissertation are to first and foremost research non-stoichiometric perovskite structures via solid state synthesis. In order to determine a route for incorporation of platinum group metals into the crystal structure.

Characterise, understand and tailor the crystal structure of said PGM perovskite system to be compatible with known automotive catalytic routes with Johnson Matthey (industrial sponsor).

Fully characterise the oxidation structure of nanoparticles and correlate to automotive catalytic applications including Diesel Oxidation, and Three way catalytic applications.

Perovskite Oxide Structure

The common stoichiometric formulae for perovskite is ABO_3, which is a mixed oxide where A and B are cations. Perovskites are ceramic materials with both metallic and non-metallic elements (oxygen), and they can be applied to a variety of applications, including capacitors, catalysis and, more recently, photovoltaic processes. $CaTiO_3$ is known classically as a perovskite. It was first reported by Gustav Rose in 1839 and was named after the Russian mineralogist Count Lev Aleksevich von Perovskite.[43] Perovskites are generally crystalline cubic structures with a space group of Pm3m, although they can range in structure from tetragonal, orthorhombic, rhombohedral, monoclinic and triclinic (examples of which can be seen in Table 1-1). The radius of the A site cation which is coordinated to 12 oxygen anions is often larger in size in order to accommodate the smaller B site cation within the lattice structure. A site cations can be categorized into rare earth, alkaline and alkali metals, such as Lanthanum, Barium and Sodium. B site cations are usually transition elements, characterized by their ability to fit into the perovskite lattice occupying octahedral interstices surrounded by six anion oxygen atoms within the framework. [44,45]

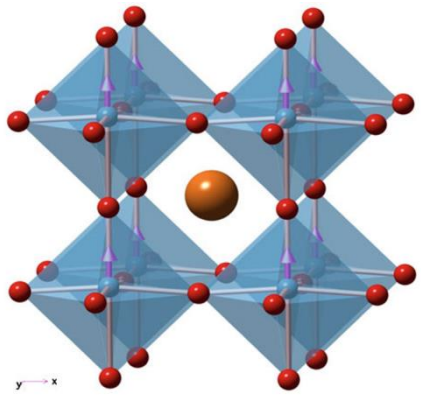

Figure 1-5 depicts a cubic perovskite lattice, with the central orange sphere representing an A site cation, and the central blue sphere representing a B site cation surrounded by 6 red oxygen anions.[46]

Cubic	$SrTiO_3$,$BaMnO_3$,$La_{0.4}Sr_{0.6}CoO_3$,$BaTiO_3$ (>120°C)
Tetragonal	$BaTiO_3$ (at room temperature), $BiAlO_3$,$PbTiO_3$
Rhombohedral	$LaAlO_3$,$LaNiO_3$,$LaCOO_3$,$BaFeO_3$
Orthorhombic	$GdFeO_3$,$CaTiO_3$,$LaRhO_3$
Monoclinic	$PbSnO_3$,$BiCrO_3$
Triclinic	$BiMnO_3$

Table 1-1: A table of typical perovskite structures with different crystal structures

The Goldschmidt tolerance factor (t) relates to the quantity of crystal defects which is applicable to all perovskite cells of which the stability of the phase is governed by Equation (1):[47]

$$t = r\frac{(r_A + r_0)}{\sqrt{2}(r_B + r_0)}$$

Goldschmidt first reported on $YAlO_3$ and $LaFeO_3$ indicating that the calculated tolerance factor t must be in the range of 0.75-0.1.[48] $SrTiO_3$ is an undistorted cubic perovskite having a tolerance factor of 1. As the tolerance factor is a measure of the geometry of the perovskite cell, it is a measure between two cations r_A and r_B in order to create a cubic cell, as can be seen in figure 1-6.[46] As the tolerance factor increases beyond t>1, the radius of cation A (r_A) becomes too large for the perfect cubic cell and thus displays a distorted octahedra which can lead to in-phase and out-of-phase tilting or, in some cases, both.[49,50,51] This distortion of the octahedra can lead to more stable structures forming, such as orthorhombic or rhombohedral structures. If the tolerance factor t exceeds 1, then the structure forms a hexagonal ilmenite ($FeTiO_3$); however, the tolerance factor alone is not enough to predict the cubic structure of a perovskite.[52]

r_A,r_B and r_0 represent the empirical atomic radii of the A and B cations and the oxygen anion obtained from X-ray diffraction data conducted by R.D. Shannon.[53]

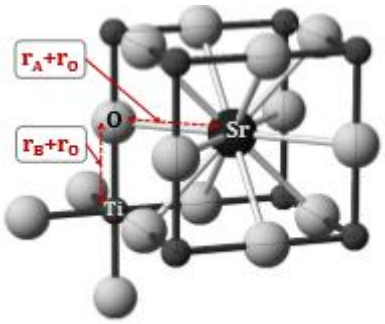

Figure 1-6 shows the distance between atoms r_A and r_B in relation to the cubic structure of the perovskite $SrTiO_3$.

The level of dopant and what cations can be chosen for the A and B site are dependent upon the ionic radii and the charge of the atom. If the atomic radii of the A site atom is too large, then the structure of the perovskite will distort, leading to either a change in structure or composition of phases. A site cations have a higher ionic radii and a larger coordination number from 8-12 in comparison to the B site cations. A comparison of ionic radius size between A and B site cations can be seen in Table 1-2.[52]

dodecahedral A site			octahedral B site		
ion	radius (Å)[a]	radius (Å)[b]	ion	radius (Å)[a]	radius (Å)[b]
Na^{+}	1.06	1.32? (IX)	Li^{+}	0.68	0.74
K^{+}	1.45	1.60?	Cu^{2+}	0.72	0.73
Rb^{+}	1.61	1.73	Mg^{2+}	0.66	0.72
Ag^{+}	1.40	1.30 (VIII)	Zn^{2+}	0.74	0.75
Ca^{2+}	1.08	1.35	Ti^{3+}	0.76	0.67
Sr^{2+}	1.23	1.44	V^{3+}	0.74	0.64
Ba^{2+}	1.46	1.60	Cr^{3+}	0.70	0.62
Pb^{2+}	1.29	1.49	Mn^{3+}	0.66	0.65
La^{3+}	1.22	1.32?	Fe^{3+}	0.64	0.64
Pr^{3+}	1.10	1.14 (VIII)	Co^{3+} (LS)		0.52
Nd^{2+}	1.09	1.12(VIII)	Co^{3+} (HS)	0.63	0.61
Bi^{3+}	1.07	1.11(VIII)	Ni^{3+} (LS)		0.56
Ce^{4+}	1.02	0.97(VIII)	Ni^{3+} (HS)	0.62	0.60
Th^{4+}	1.09	1.04(VIII)	Rh^{3+}	0.68	0.66
			Ti^{4+}	0.68	0.60
			Mn^{4+}	0.56	0.54
			Ru^{4+}	0.67	0.62
			Pt^{4+}	0.65	0.63
			Nb^{5+}	0.69	0.64
			Ta^{5+}	0.69	0.64
			Mo^{6+}	0.62	0.60
			W^{6+}	0.62	0.60

Table1-2 represents a variety of A and B site cations and their corresponding ionic radii. With permission from the handbook of industrial chemistry with permission from the handbook of industrial chemistry[66].

Non stoichiometry and exsolution

Although perovskites have the stoichiometry of ABO_3, they also display non-stoichiometry for all three sites (ABO). Non-stoichiometry of the B site cation is not common; however, sub-stoichiometry $A_1-\alpha BO_3$, ABO_{3-y} and super stoichiometry $A_1+\alpha BO_3$, ABO_{3+y} are possible. Non-stoichiometry is incredibly important and is the essential aspect of exsolution. By harnessing the ability to tailor sub-stoichiometric perovskites it is possible to change the defect chemistry of the catalyst dependent upon doping levels of both the A and B site cations. Compounds with both A site and O deficiency are dependent upon the nature of the B site cation.

Exsolution of the B site cation is due to tailoring of the sub-stoichiometric defect chemistry by changing both A and B site cations so the charge is balanced. When these materials are exposed to reduction at a high temperature (above 600 °C), oxygen anions are removed from the lattice structure, leading to electron and oxygen deficiency.[54] Exsolution offers an alternative to common catalytic techniques such as chemical vapour deposition or impregnation. This is because the B site cation is anchored to the lattice rather than deposited.[55] Unlike deposited metal particles, it is possible, through careful reduction conditions, to control the particle size and reduce agglomeration of coked particles as a result show in Figure 1-6.

The term ‘exsolution’ is not widely used for the movement of B site metal particles in and out of the lattice upon reduction and oxidation. Recent papers have primarily focused on methane combustion and materials for anodes.[56–62]

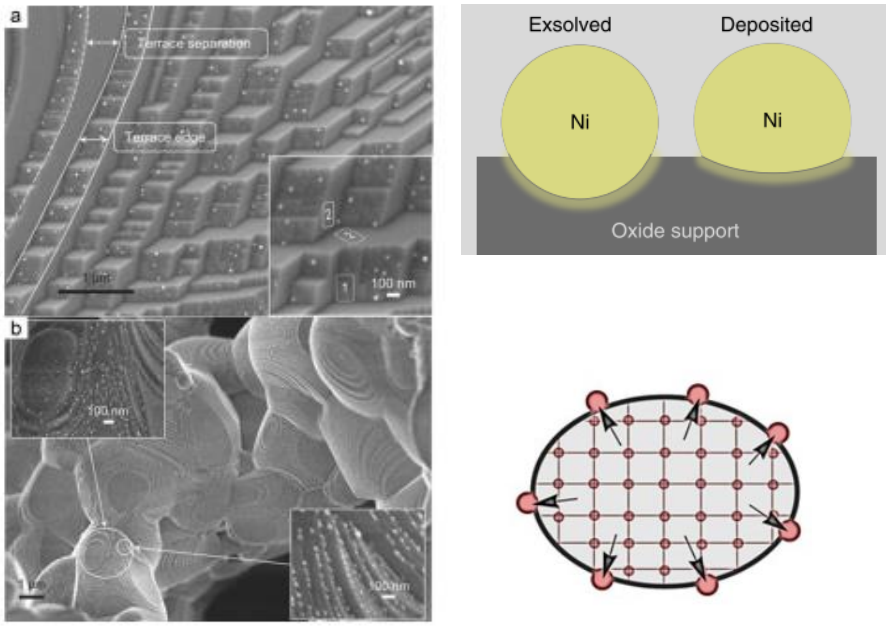

Figure 1-7 with permission from D. Neagu: a) terraced view of exsolved nano Ni particles b) cleaved surface revealing decorated NI nanoparticles.

Sub-stoichiometric, charge-balanced A and B site cations are incredibly important for exsolution in catalysis, the applications of which are expansive, ranging from oxidation and refining processes to hydrogenation.

Role of perovskites as catalysts

The global catalyst business is worth roughly $16.3 billion dollars per year (as shown in Table 1-3), and the subsequent value of chemicals and fuels derived from that in 1991 was $900 billion dollars per year.[63] Over 90% of all industrial chemicals and polymer production is produced with the help of catalysts. Catalysis plays a key societal role in producing fuels and

polymers and in pollution control.[63] Previously, perovskite-type mixed oxides have been reported in 1971[11] as highly catalytically active, with $Sr_{0.2}La_{0.5}CoO_3$ perovskite rivalling platinum. Further ground-breaking studies were carried out in the early 1970s on novel perovskites used as catalysts for reactions such as NOx reduction[64] and CO oxidation.[65]

	2010	*2015*	*CAGR (%)[b]*
Petroleum Refining	**4.03**	**4.81**	**4**
Hydroprocessing[c]	2.08	2.62	5
Fluid catalytic cracking[c]	1.23	1.41	3
Alkylation, reforming, and others[c]	0.72	0.78	2
Chemical Processing	**5.20**	**7.02**	**6**
Polyolefins	1.24	1.52	4
Adsorbents	1.30	1.52	3
Chemical catalysts	2.67	3.98	8
Oxidation, ammoxidation, and oxychlorination[d]	1.11	1.61	8
Hydrogen, ammonia, and methanol synthesis[d]	0.81	1.30	10
Hydrogenation[d]	0.17	0.25	7
Dehydrogenation[d]	0.12	0.18	9
Organic synthesis[d]	0.46	0.64	7
Mobile Emission Control	**4.81**	**8.58**	**12**
Heavy-duty diesel	0.72	2.87	32
Motorcycles	0.20	0.42	16
Light-duty	3.90	5.29	6
Total Catalyst Demand	**14.04**	**20.41**	**8**

Table 1-3 shows the global catalyst demand forecast by application in US$ (Billions)/year.[66]With permission from the handbook of industrial chemistry

Perovskites, as mixed-oxide materials, display the robustness and thermal stability required by current heterogeneous catalysts and are capable of being used in many catalytic applications (as shown in Table 1-4). As a ceramic material, perovskites can be synthesised by both solid-state and soft chemistry routes, further supporting its flexibility to act as a tailored catalyst for selected reaction processes.

Catalytic reaction	Examples of perovskite catalyst
Complete oxidation (catalytic combustion) of CO, hydrocarbons, and alcohols	(La, Sr)CoO_3, (La, Sr) MnO_3
Elimination of NO_x (reduction, decomposition, absorption)	(La, Sr)MnO_3 $YBa_2Cu_3O_x$, La_2CuO_4
Oxidative coupling of methane	$PbTiO_3$, $LaMnO_3$
Electrode (oxygen)	(La, Sr)CoO_3
Gas sensor Alcohol, CO, oxygen, humidity	(La, Sr)CoO_3, $LaNiO_3$
Membrane reactor CH_4 to CO, H_2	(La, Sr) (Ga, Fe)O_x (Ba, Sr) (Fe, Mn)O_x

Table 1-4 shows a list of various catalytic reactions where perovskites are already used, taken with permission for the handbook of industrial chemistry.[67]

When designing novel exsoluting perovskite catalysts, we must bear in mind the core principals of industrial catalysis and the major properties of the catalyst and model reactions chosen, which are listed below:

1. Activity
    a. moderate conditions
    b. rate of reaction
    c. turnover number: number of molecules produced by an active site per given time
    d. space time yield: determination of reactor size for a given reaction
    e. space velocity: gas flow per hour through a catalyst bed

2. Selectivity and yield
    a. to desired product
    b. limiting factors involved such as % conversion rate in relation to catalyst degradation
    c. the recyclability of feedstock (for example, in hydrocarbon cracking)
    d. adaptability in minor changes to feedstock

3. Stability
    a. loss in activity over time
    b. operational lifetime
    c. thermal influences
    d. consistency of feedstock
    e. effect of regeneration (such as calcination/removal of coke)
    f. poisoning of catalyst due to inconsistent feedstock (such as sulphur)

4. Strength
    a. shape and size of catalyst, is it the right size for the operation
    b. coking formation from feedstock
    c. disintegration due to pressure in reaction

Catalyst support

Surface area and porosity comprise two major areas of study for heterogeneous catalysis. Porous exsoluting catalysts, that have previously been reported in literature, are primarily related to SOFC (solid oxide fuel cell). Reported uses have extended to methane reforming[68] and steam electrolysis.[69–72]Typically exsoluting perovskites have been made as dense bulk materials with little or no porosity, but by incorporating meso, micro or macro porosity, the diversity and applications of exsoluting perovskites increases dramatically. Perovskite-type mixed oxides lack in the porosity needed for many shape-selective reactions. Novel ways of overcoming non-porous materials have been pioneered by solid-state, sol-gel, hydrothermal synthesis, co-precipitation, reactive grinding, microemulsion and nanocasting methods in order to create a well-defined nanoparticle size, and thereby improving porosity.

Summary

Work by Daihatsu and furthermore more recent work in the area of nano-particle emergence from PGM perovskite systems[8,73–76,76–79] have all shown that the incorporation of Pt, Pd and Rh through sol-gel synthesis routes is possible, however the stabilisation of the nanoparticles grown are not as previously reported by Daihatsu (Tanka et al). This leaves a large area to be explored, one where the crystal structure is fully characterised, non-amorphous and high temperature stable perovskite systems must first be studied to understand the phenomenon fully. There is yet to be any publication or work in the area of solid state synthesis of Platinum perovskite systems with a crystalline structure and use in automotive catalysis.

References

1. Galassi, G. & Spada, G. Sea-level rise in the Mediterranean Sea by 2050: Roles of terrestrial ice melt, steric effects and glacial isostatic adjustment. *Glob. Planet. Change* **123**, 55–66 (2014).

2. Rowley, R. J., Kostelnick, J. C., Braaten, D., Li, X. & Meisel, J. Risk of Rising Sea Level to Population and Land Area. *Eos, Trans. Am. Geophys. Union* **88**, 105 (2007).

3. Alley, R. B., Clark, P. U., Huybrechts, P. & Joughin, I. Ice-sheet and sea-level changes. *Science* **310**, 456–60 (2005).

4. Cox, P. M., Betts, R. A., Jones, C. D., Spall, S. A. & Totterdell, I. J. Acceleration of global warming due to carbon-cycle feedbacks in a coupled climate model. *Nature* **408**, 184–187 (2000).

5. Corma, A. & López Nieto, J. M. *The Role of Rare Earths in Catalysis*. *Handbook on the Physics and Chemistry of Rare Earths* **29**, (Elsevier, 2000).

6. GE Dolber. *System for removing nitrogen oxide from automotive ehaust. US Patent 3,767,764, (1973).*

.powered by internal combustion engines. *Environ. Health Perspect.* **10**, 159–164 (1975).

8. Farrauto, R. J., Deeba, M. & Alerasool, S. journey to cleaner air. *Nat. Catal.* **2**, 603–613 (2021).

9. Eastwood, P. *Critical topics in exhaust gas aftertreatment*. (Research Studies Press, 2000).

10. Summers, J. C., Sawyer, J. E. & Frost, A. C. The 1990 Clean Air Act and Catalytic Emission Control Technology for Stationary Sources. in *Catalytic Control of Air Pollution* **495**, 8–98 (American Chemical Society, 1992).

11. Libby, W. F. Promising Catalyst for Auto Exhaust. *Science (80-.).* **171**, 499–500 (1971).

12. Twigg, M. V. Progress and future challenges in controlling automotive exhaust gas emissions. *Appl. Catal. B Environ.* **70**, 2–15 (2007).

13. Russell, A., Epling, W. S., Russell, A. & Epling, W. S. Diesel Oxidation Catalysts Diesel Oxidation Catalysts. **4940**, (2011).

14. Twigg, M. V. Catalytic control of emissions from cars. *Catal. Today* **163**, 33–41 (2011).

15. Matthey, J. Johnson Matthey Annual Report 2018 - customers. (2018).

16. Misono, M. Mixed Oxides as Catalyst Supports. **176**, 157–173 (2013).

17. Tanaka, H. & Misono, M. Advances in designing perovskite catalysts. *Curr. Opin. Solid State Mater.* (2001).

18. Tanaka, H. *et al.* Design of the intelligent catalyst for Japan ULEV standard. *Top. Catal.* **30/31**, 389–396 (2004).

19. Screen, T. Platinum Group Metal Perovskite Catalysts. *Platin. Met. Rev.* **51**, 87–92 (2007).

20. Russell, A. & Epling, W. S. Diesel Oxidation Catalysts. *Catal. Rev.* **53**, 337–423 (2011).

21. Kröcher, O. *et al.* Investigation of the selective catalytic reduction of NO by NH3 on Fe-ZSM5 monolith catalysts. *Appl. Catal. B Environ.* **66**, 208–216 (2006).

22. Prasad, D. H. *et al.* Effect of nickel nano-particle sintering on methane reforming activity of Ni-CGO cermet anodes for internal steam reforming SOFCs. *Appl. Catal. B Environ.* **101**, 531–539 (2011).

23. Prasad, D. H. *et al.* Effect of steam content on nickel nano-particle sintering and methane reforming activity of Ni–CZO anode cermets for internal reforming SOFCs. *Appl. Catal. A Gen.* **411**–**412**, 160–169 (2012).

24. Deng, J., Cai, M., Sun, W., Liao, X. & Chu, W. Oxidative Methane Reforming with an Intelligent Catalyst: Sintering-Tolerant Supported Nickel Nanoparticles. (2013).

25. Nishihata, Y. *et al.* Self-regeneration of a Pd-perovskite catalyst for automotive emissions control. *Nature* **418**, 164–167 (2002).

26. Tanaka, H. *et al.* An intelligent catalyst. -*SOCIETY Automot. Eng. JAPAN* (2001).

27. Kajita, N., Uenishi, M., Tan, I., Tanaka, H. & Kimura, M. Regeneration of Precious Metals in Various Designed Intelligent Perovskite Catalysts. (2002).

28. Sato, N., Tanaka, H., Tan, I., Uenishi, M. & Kajita, N. Design of a practical Intelligent catalyst. *SAE Trans.* (2003).

29. Nishihata, Y., Mizuki, J., Tanaka, H., Uenishi, M. & Kimura, M. Self-regeneration of palladium-perovskite catalysts in modern automobiles. in *Journal of Physics and Chemistry of Solids* (2005).

30. Tanaka, H. An intelligent catalyst: the self-regenerative palladium–perovskite catalyst for automotive emissions control. *Catal. Surv. from Asia* (2005).

31. Uenishi, M., Tanaka, H., Taniguchi, M., Tan, I. & Sakamoto, Y. The reducing capability of palladium segregated from perovskite-type LaFePdO x automotive catalysts. *Appl. Catal. A* (2005).

32. Nishihata, Y., Mizuki, J., Tanaka, H. & Uenishi, M. Self-regeneration of palladium-perovskite catalysts in modern automobiles. *J. Phys.* (2005).

33. Tanaka, H., Tan, I., Uenishi, M., Taniguchi, M. & Nishihata, Y. The Intelligent Catalyst: Pd-Perovskite Having the Self-Regenerative Function in a Wide Temperature Range. *Key Eng. Mater.* (2006).

34. Taniguchi, M. *et al.* The self-regenerative Pd-, Rh-, and Pt-perovskite catalysts. in

Topics in Catalysis (2007).

35. Taniguchi, M., Uenishi, M., Tan, I., Tanaka, H. & Kimura, M. Thermal Properties of the Intelligent Catalyst. (2004).

36. Tanaka, H. *et al.* Self-Regenerating Rh- and Pt-Based Perovskite Catalysts for Automotive-Emissions Control. *Angew. Chemie Int. Ed.* **45**, 5998–6002 (2006).

37. Hamada, I., Uozumi, A., Morikawa, Y., Yanase, A. & Katayama-Yoshida, H. A density functional theory study of self-regenerating catalysts LaFe1-xMxO3-y(M = Pd, Rh, Pt). *J. Am. Chem. Soc.* **133**, 18506–18509 (2011).

38. Tanaka, H. & Kaneko, K. Method for producing perovskite-type composite oxide. *US Pat. 7,381,394* (2008).

39. Katz, M. B. *et al.* Reversible precipitation/dissolution of precious-metal clusters in perovskite-based catalyst materials: Bulk versus surface re-dispersion. *J. Catal.* **293**, 145–148 (2012).

40. Malamis, S. A. *et al.* Comparison of precious metal doped and impregnated perovskite oxides for TWC application. *Catal. Today* **258**, 535–542 (2015).

41. Katz, M. Advanced Transmission Electron Microscopy Studies of Induced Interactions of Metallic Species with Perovskite Oxide Hosts. (2013).

42. Jarrige, I. *et al.* Toward optimizing the performance of self-regenerating Pt-based perovskite catalysts. *ACS Catal.* **5**, 1112–1118 (2015).

43. Hazen, R. M. Perovskites. *Scientific American* **258**, 74–81 (1988).

44. Keav, S., Matam, S., Ferri, D. & Weidenkaff, A. Structured Perovskite-Based Catalysts and Their Application as Three-Way Catalytic Converters—A Review. *Catalysts* **4**, 226–255 (2014).

45. Tejuca, L. G., Fierro, J. L. G. & Tascón, J. M. D. Structure and Reactivity of Perovskite-Type Oxides. *Adv. Catal.* **36**, 237–328 (1989).

46. Neagu, D. Materials and Microstructures for High Temperature Electrochemical Devices through Control of Perovskite Defect Chemistry Dragos Neagu. 1–257 (2012).

47. Goldschmidt, V. M. Die gesetze der krystallochemie. (1926).

48. Peña, M. A. & and J. L. G. Fierro*. Chemical Structures and Performance of Perovskite Oxides. *Chem. Rev.* **101**, 1981–2018 (2001).

49. Chynoweth, A. G. {\it Ferroelectricity in crystals} by H. D. Megaw. *Acta Crystallogr.* **11**, 754–755 (1958).

50. Allan, N. L., Dayer, M. J., Kulp, D. T. & Mackrodt, W. C. Atomistic lattice simulations of the ternary fluorides AMF3(A = Li, Na, K, Rb, Cs; M = Mg, Ca, Sr, Ba). *J. Mater. Chem.* **1**, 1035–1039 (1991).

51. Neagu, D. & Irvine, J. T. S. *Perovskite Defect Chemistry as Exemplified by Strontium Titanate*. *Comprehensive Inorganic Chemistry II* (Elsevier Ltd., 2013).

52. Duprez, D. *et al.* Perovskites as Substitutes of Noble Metals for Heterogeneous

Catalysis : Dream or Reality Se b. *Chem. Rev.* **114**, 10292 (2014).

53. Shannon, R. D. Revised effective ionic radii and systematic studies of interatomic distances in halides and chalcogenides. *Acta Crystallogr. Sect. A* **32**, 751–767 (1976).

54. Neagu, D., Tsekouras, G., Miller, D. & Ménard, H. In situ growth of nanoparticles through control of non-stoichiometry. *Nat. Chem.* (2013).

55. Neagu, D. & Irvine, J. T. S. Enhancing electronic conductivity in strontium titanates through correlated A and B-site doping. *Chem. Mater.* **23**, 1607–1617 (2011).

56. Oh, T., Rahani, E., Neagu, D. & Irvine, J. Evidence and Model for Strain-Driven Release of Metal Nanocatalysts from Perovskites during Exsolution. *J.* (2015).

57. Zhu, Y. *et al.* Promotion of oxygen reduction by exsolved silver nanoparticles on a perovskite scaffold for low-temperature solid oxide fuel cells. *Nano Lett.* (2015).

58. Liu, S., Chuang, K. & Luo, J. Double layered perovskite anode with in-situ exsolution of Co-Fe alloy to cogenerate ethylene and electricity in proton conducting ethane fuel cell. *ACS Catal.* (2015).

59. Tsvetkov, D., Ivanov, I. & Malyshkin, D. Oxygen content, cobalt oxide exsolution and defect structure of the double perovskite PrBaCo 2 O 6− δ. *J. Mater.* (2016).

60. Thalinger, R., Gocyla, M. & Heggen, M. Ni–perovskite interaction and its structural and catalytic consequences in methane steam reforming and methanation reactions. *J.* (2016).

61. Miller, E. Synthesis, Characterization, and Optimization of Novel Solid Oxide Fuel Cell Anodes. (2015).

62. Liu, S., Chuang, K. & Luo, J. Erratum to "Double Layered Perovskite Anode with in Situ Exsolution of Co–Fe Alloy To Cogenerate Ethylene and Electricity in Proton-Conducting Ethane Fuel Cell". *ACS Catal.* (2016).

63. Armor, J. N. A history of industrial catalysis. *Catal. Today* **163**, 3–9 (2011).

64. Voorhoeve, R. J. H., Remeika, J. P. & Johnson, D. W. Rare-Earth Manganites: Catalysts with Low Ammonia Yield in the Reduction of Nitrogen Oxides. *Science (80-.).* **180**, 62–64 (1973).

65. Gallagher, P. K., Johnson, D. W. & Schrey, F. Studies of some supported perovskite oxidation catalysts. *Mater. Res. Bull.* **9**, 1345–1352 (1974).

66. Bravo-Suárez, J. J., Chaudhari, R. V & Subramaniam, B. Design of Heterogeneous Catalysts for Fuels and Chemicals Processing: An Overview. in *Novel Materials for Catalysis and Fuels Processing* 3–68, (2013).

67. Misono, M. Catalysis of Perovskite and Related Mixed Oxides. *Stud. Surf. Sci. Catal.* **176**, 67–95 (2013).

68. Neagu, D., Oh, T., Miller, D., Ménard, H. & Bukhari, S. Nano-socketed nickel particles with enhanced coking resistance grown in situ by redox exsolution. *Nat. Commun.* (2015).

69. Xu, S. *et al.* Perovskite chromates cathode with resolved and anchored nickel nano-

particles for direct high-temperature steam electrolysis. *J. Power Sources* (2014).

70. Tsekouras, G., Neagu, D. & Irvine, J. Step-change in high temperature steam electrolysis performance of perovskite oxide cathodes with exsolution of B-site dopants. *Energy Environ. Sci.* (2013).

71. Li, Y., Wang, Y., Doherty, W., Xie, K. & Wu, Y. Perovskite chromates cathode with exsolved iron nanoparticles for direct high-temperature steam electrolysis. (2013).

72. Sun, Y., Li, J., Zeng, Y., Amirkhiz, B. & Wang, M. A-site deficient perovskite: the parent for in situ exsolution of highly active, regenerable nano-particles as SOFC anodes. *J. Mater.* (2015).

73. Prabha, I. Current Status of Platinum Based Nanoparticles : Physicochemical Properties and Selected Applications – A Review. 122–133 (2019).

74. Da, Y. *et al.* Catalytic oxidation of diesel soot particulates over Pt substituted LaMn 1-x Pt x O 3 perovskite oxides. *Catal. Today* **327**, 73–80 (2019).

75. Li, X. *et al.* In situ exsolution of PdO nanoparticles from non-stoichiometric LaFePd0.05O3+Δ electrode for impedancemetric NO2 sensor. *Sensors Actuators, B Chem.* **298**, (2019).

76. Gao, Y. *et al.* Energetics of Nanoparticle Exsolution from Perovskite Oxides. *J. Phys. Chem. Lett.* **9**, 3772–3778 (2018).

77. Fang, C. *et al.* Highly Dispersed Pt Species with Excellent Stability and Catalytic Performance by Reducing a Perovskite-Type Oxide Precursor for CO Oxidation. *Trans. Tianjin Univ.* **24**, 547–554 (2018).

78. Fierro, J. L. G. Chemical Structures and Performance of Perovskite Oxides. (2017).

79. Zhang, S. In-situ and Ex-situ Microscopy and Spectroscopy Study of Catalytic Materials by. 217 (2017).

80. Glazer, A. M. The classification of tilted octahedra in perovskites. *Acta Crystallogr. Sect. B* **28**, 3384–3392 (1972).

81. Howard, C. J. & Stokes, H. T. Group-Theoretical Analysis of Octahedral Tilting in Perovskites. *Acta Crystallogr. Sect. B* **54**, 782–789 (1998).

82. Neagu, D., Tsekouras, G., Miller, D. D. N., Ménard, H. & Irvine, J. T. S. In situ growth of nanoparticles through control of non-stoichiometry. *Nat. Chem.* **5**, 916–923 (2013).

83. G. ROUSSEAU. No Title. *Acad. Sci. Paris* **109**, 144 (1889).

84. Statton, W. O. The phase diagram of the BaO-TiO2system. *J. Chem. Phys.* **19**, 33–40 (1951).

85. Randall, J. J. & Ward, R. The Preparation of Some Ternary Oxides of the Platinum Metals. *J. Am. Chem. Soc.* **81**, 2629–2631 (1959).

86. Haradem, P. S., Chamberland, B. L., Katz, L. & Gleizes, A. A structural model for barium platinum oxide, Ba3Pt2O7. *J. Solid State Chem.* **21**, 217–223 (1977).

87. Chaston, J. C. Reactions of Oxygen with the Platinum Metals; II-OXIDATION OF RUTHENIUM, RHODIUM, IRIDIUM AND OSMIUM. *Platin. Met. Rev.* **9**, 51–56 (1965).

88. Sharma, P. A., Brown-Shaklee, H. J. & Ihlefeld, J. F. Oxygen partial pressure dependence of thermoelectric power factor in polycrystalline n-type SrTiO3: Consequences for long term stability in thermoelectric oxides. *Appl. Phys. Lett.* **110**, (2017).

89. Kuklja, M. M., Mastrikov, Y. A., Jansang, B. & Kotomin, E. A. The intrinsic defects, disordering, and structural stability of Ba xSr 1-xCo yFe 1-yO 3-δ perovskite solid solutions. *J. Phys. Chem. C* **116**, 18605–18611 (2012).

90. Nur, A. S. M. *et al.* Phase-Dependent Formation of Coherent Interface Structure between PtO2 and TiO2 and Its Impact on Thermal Decomposition Behavior. *J. Phys. Chem. C* **122**, 662–669 (2018).

CHAPTER 2 METHOD

2.1 Method

A variety of methods have been used to both synthesise and characterise the perovskite mixed-oxide materials made. Solid-state synthesis and solution combustion synthesis will be covered in the following section.

Solid-State Synthesis of A-site deficient perovskite

Solid-state synthesis is the main focus of the materials made in this report. Due to characterisation techniques, it is more reliable from a characterisation perspective compared with sol-gel synthesis this is due to the crystalline nature of solid state synthesised A-site deficient perovskite materials, sol-gel produces a more amorphous less crystalline material and thus making it difficult to charecterise. In order to make a single phase crystal perovskite structure, initial stoichiometry should be studied. This is explained in chapter 3 Tailoring the Stoichiometry.

Using the various precursors dependent upon the composition (La_2O_3,TiO_2,$BaCO_3$,$SrCO_3$) carbonates, nitrates and mixed oxides were dried at various temperatures in order to remove water-bound molecules from the precursor material. The precursor material was weighed hot at 250 ºC in order to preserve the stoichiometric nature of the perovskite and accurately measure the correct amount of precursor materials.

The oxide precursors were then quantitatively transferred to a glass beaker, and acetone was then added to the beaker in order to whet the samples and act as a solvent for the copolymer dispersant (Hypermer KD-1, a polyester copolymer surfactant). The mixture was then pulse sonicated using an ultrasonic probe (Heilscher UP200S) in order to homogenise and reduce the particle size of the various precursors,

which allowed for a more homogeneous sample to be prepared rather than using conventional solid-state synthesis routes, such as grinding with a mortar or pestle. Fowling dispersion, acetone is then evaporated from the homogeneous solution using a magnetic stirring plate at room temperature. Once the acetone has evaporated from the mixture, the compositional mixture is then transferred to an aluminium crucible and calcined in a muffle furnace at 1000 ºC for 12 hours. Calcination at 1000 ºC allows for the decomposition of any nitrates of carbonates, as well as further removing any solvent impurities, copolymer and water-bound molecules. During calcination, the perovskite phase is partially formed, resulting in the seeding crystallisation of the perovskite phase. After calcination, the powder is weighed and should equal that of the calculated weight expected as a result of removed carbonates and nitrates (if calculated for 10g, approximately 9-9.5g of powder should be present).

Following calcination, the powder is then ball milled with acetone at 300rpm for 2 hours in a planetary ball mill, using 1 mm zirconia balls. The powder is then dried in an evaporator dish.

Precursors

The high purity oxide and carbonate precursors, such as La_2O_3 (Pi-Kem, >99.99%) and TiO_2 (Alfa Aesar, >99.6%), $BaCO_3$ (Alfa Aesar, >99%), $CaCO_3$ (Fisher Chemical, >99%) and $SrCO_3$ (Aldrich, >99.9%), are dried at 300 ºC (La_2O_3 at 800 ºC) in order to remove water-bound molecules from the precursors for a correct stoichiometric nature of the perovskites. PtO_2 (Alfa Aesar, anhydrous) and Pt nitrate solution (Johnson Matthey, 16.17 wt% Pt) are used as Pt precursors, and $\gamma{-}Al_2O_3$ (Sasol, Particle size $\leq$ 5 mm, S_{BET} 138−158 m^2/g) is purchased.

Trojan horse co-precursor $Ba_3Pt_2O_7$

The Trojan horse co-precursors necessity in the solid state synthesis is a significant step in the production of a single phase Pt containing perovskite. The nature of the trojan horse is explained in detail in Chapter 3 Barium Platinate.

$BaCO_3$ and PtO_2 are weighted and mixed together by the correct stoichiometric amount in a Pt crucible, and then fired in a static air furnace with a ramp rate of 5ºC/min to 1000°C for 12 hrs.

Pt doped Perovskite synthesis

A-site deficient perovskites of $La_{0.4}Ca_{0.3925}Ba_{0.0075}Pt_{0.005}Ti_{0.995}O_3$ ($LaCaBaPtTiO_3$ or Pt@LCT) and $La_{0.4}Sr_{0.3925}Ba_{0.0075}Pt_{0.005}Ti_{0.995}O_3$ ($LaSrBaPtTiO_3$ or Pt@LST) are designed by containing 0.5 wt% of Pt. Non-doped perovskites of $La_{0.4}Ca_{0.4}TiO_3$ ($LaCaTiO_3$), $La_{0.4}Sr_{0.4}TiO_3$ ($LaSrTiO_3$), $La_{0.4}Ca_{0.3925}Ba_{0.0075}TiO_3$ ($LaCaBaTiO_3$ or LCT) and $La_{0.4}Sr_{0.3925}Ba_{0.0075}TiO_3$ ($LaSrBaTiO_3$ or LST) are prepared as references. Carefully calculated precursors are quantitatively transferred to a glass beaker, and acetone is then added to the beaker with a copolymer dispersant (Hypermer KD-1, a polyester copolymer surfactant). The mixture is pulse sonicated using an ultrasonic probe (Heilscher UP200S) in order to homogenise and reduce the particle size of the precursors. Following dispersion of the powders in acetone, acetone is evaporated from the homogeneous solution, and the compositional mixture is then calcined in a muffle furnace at 1000 ºC for 12 hrs to partially form the perovskite phase for seeding crystallisation. Following calcination, the sample is ball milled with acetone at 300 rpm for 2 hrs in a planetary ball mill, using 1 mm zirconia balls. Then, the sample is dried in an evaporator dish at room temperature.

O_2-rich sintering process

Sintering in an oxygen rich environment is crucial to the formation of a single-phase perovskite system. In part to hold the reduction of Pt-O to Pt metal. Pellets are prepared by pressing the sample powders and then firing them under O_2-rich sintering conditions to properly produce the pure perovskite phase at the relatively lower temperature. Pellets are fired for 12 hrs at 1200 ºC with a ramp rate of 5 ºC/min at an O_2-rich gas atmosphere of 100% O_2 and 100 $ml \cdot min^{-1}$.

In-situ emergence process

To emerge the Pt NPs onto the perovskite surface, samples are chemically reduced in a controlled atmosphere furnace at 700 ºC for 12 hrs with heating and cooling rates of 5 °C·min^{-1} under continuous flow of 5% H_2/Ar (20 ml·min^{-1}). The emerged Pt perovskites are denoted as Pt+LCT and Pt+LST. The reduction process occurs within a tube furnace which is a non-porous ceria ceramic.

Reference samples

For a comparison, Pt impregnated LCT (Pt/LCT) and Pt/γ−Al_2O_3 catalysts are synthesized by the incipient wetness method. Constant Pt concentration of 0.5 wt% was impregnated to the supports by a Pt nitrate solution, then dried at 110 °C for 24 hrs and calcined at 550 °C for 3 hrs in air. The Pt/LCT and Pt/γ−Al_2O_3 samples are then reduced in 5% H_2/Ar flow for 12 hrs at 500 ºC and 700 ºC, respectively.

Pellet forming and sintering

Pellets were prepared by pressing the powder obtained from ball milling and then firing them under sintering conditions. The pellets were then fired for 12 hours between 1200-1400 ºC, with a ramp rate of 5 ºC/minute. The density of the pellets was dependant on the composition of the perovskite. The pressing of the pellets and ball milling allows for controlled particle size as well as partial uniformity. Reduction within a planetary ball mill can occur, therefore it is vitally important to control the revolutions as well as the time.

Initially, during the first phase of sintering, necking occurs between voids of particles as a result of reduction in particle size due to the removal of excess carbonates or nitrates. Further densification takes

place as the particle size decreases and as particles become fused to one another. The voids between the particles that have not fused are known as pores. During sintering, vapour phases interconnect with one another, resulting in grain boundaries forming, which then result in pores. The stability of the pore is dependent upon the number of grain boundaries supporting it, which can be controlled through temperature and the time spent in sintering conditions. This is critical to controlling the stability of the material, especially when tailoring the perovskite material for catalytic applications.

Reduction

In order to promote defect chemistry and exsolution of B site nanoparticles, reducing conditions with a low oxygen partial pressure are used between 500-900°C. An ad gas mixture of 5%H_2Ar has been used to promote oxygen vacancies and a strongly reducing atmosphere.

Primary Characterization

Powder X-ray diffraction

X-ray diffraction is a common characterisation technique that is non-destructive for inorganic solid samples. One can primarily obtain the crystallinity and the purity of a sample, as well as differentiate between different phases. Microstructural characterisation can also determine the crystal size and lattice parameters as can be seen in Figure 2-1.

Atoms with specific periodic spacing from one another diffract X-rays, creating a unique diffraction pattern. Radiation of a specific wavelength to that atom is emitted upon excitation of an X-ray. An interference pattern is generated if the wavelength (λ) emitted is the same order of magnitude as the interatomic distances (d) and the angle of the X-ray (θ), as can be shown by Bragg's law:

$$n\lambda = 2d \sin\theta$$

Powder X-ray diffraction was carried out at room temperature using a PANalytical Empyrean diffractometer at an X-ray angle from 20-90θ using CuKα1 radiation (1.54056Å) using Bragg-Brentano geometry. The CuKα1 radiation produced by the copper in the X-ray tube passes through a monochromator crystal in order to remove the Kα doublet. In the case of laboratory-made precursor materials, such as $Ba_3Pt_2O_7$, the Inorganic Structural Database (ICSD) was used in order to gain a reference diffraction pattern for the sample prepared. STOE WinXPOW software was used to analyse the diffraction pattern and interoperate the crystal structure and cell parameter. GSAS open-source refinement software was used for carrying out Rietveld refinement of the samples.

Figure 2-1

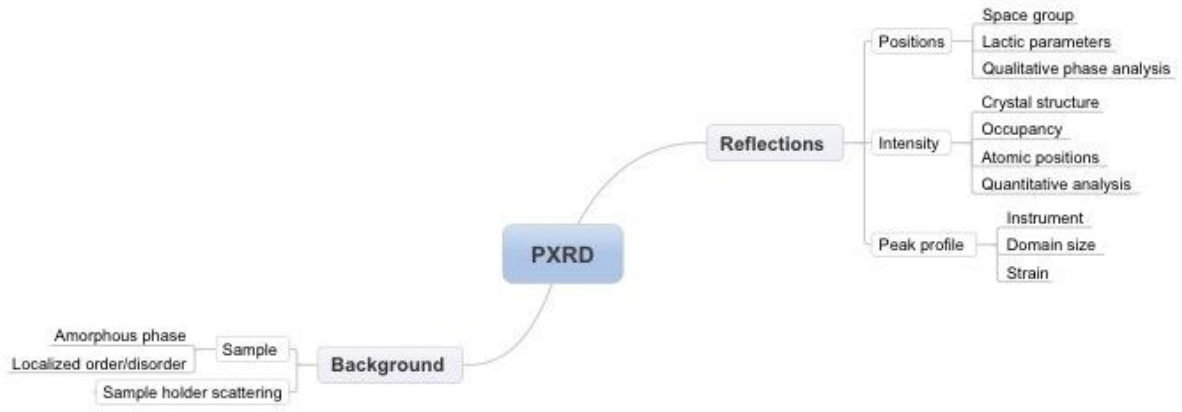

Figure 2-1: A variety of data can be collected from an XRD pattern, including symmetry, lattice parameters and quantitative data.

XRD measurements are carried out at room temperature with an X-ray angle from 10-90° by using a PANalytical Empyrean diffractometer with CuKα1 radiation (1.54056Å) and Bragg-Brentano geometry operated in reflection mode. STOE WinXPOW software is used to analyse the diffraction

pattern and interoperate the crystal structure and cell parameter. GSAS open-source refinement software is applied for carrying out Rietveld refinement of the results to ascertain the original perovskite phase and structural changes. The structural information is then used to construct the crystal structure by using CrystalMaker for Windows software.

Scanning Electron Microscopy

Scanning electron microscopy is a powerful tool used in the characterization of heterogeneous catalysis. This technique allows for the study of both microstructure, nanoparticle identification and qualitative elemental mapping of selected areas of study using element dispersive x-ray diffraction.

A JEOL JSM-5600 scanning electron microscope (SEM), a JEOL JSM-6700 field emission gun scanning electron microscope (FEG-SEM) and a FEI Scios electron microscope equipped with secondary and backscattered electron detector was used to acquire high-resolution micrographs for investigating surface morphology and phase homogeneity, especially the Pt NPs distributed on the sample surfaces. To track the Pt NPs, the number, size and particle size distribution histograms of the Pt NPs on the surfaces are calculated from the adequately magnified images using Image-Pro Plus software. The selected SEM images are converted to binary images where particles are distinguished by the pixel contrast. Particle sizes are calculated by a calibration of the SEM image scale between pixel and nm, where the particles are assumed to be a hemispheric as seen in Figure 2-2.

Figure 2-2

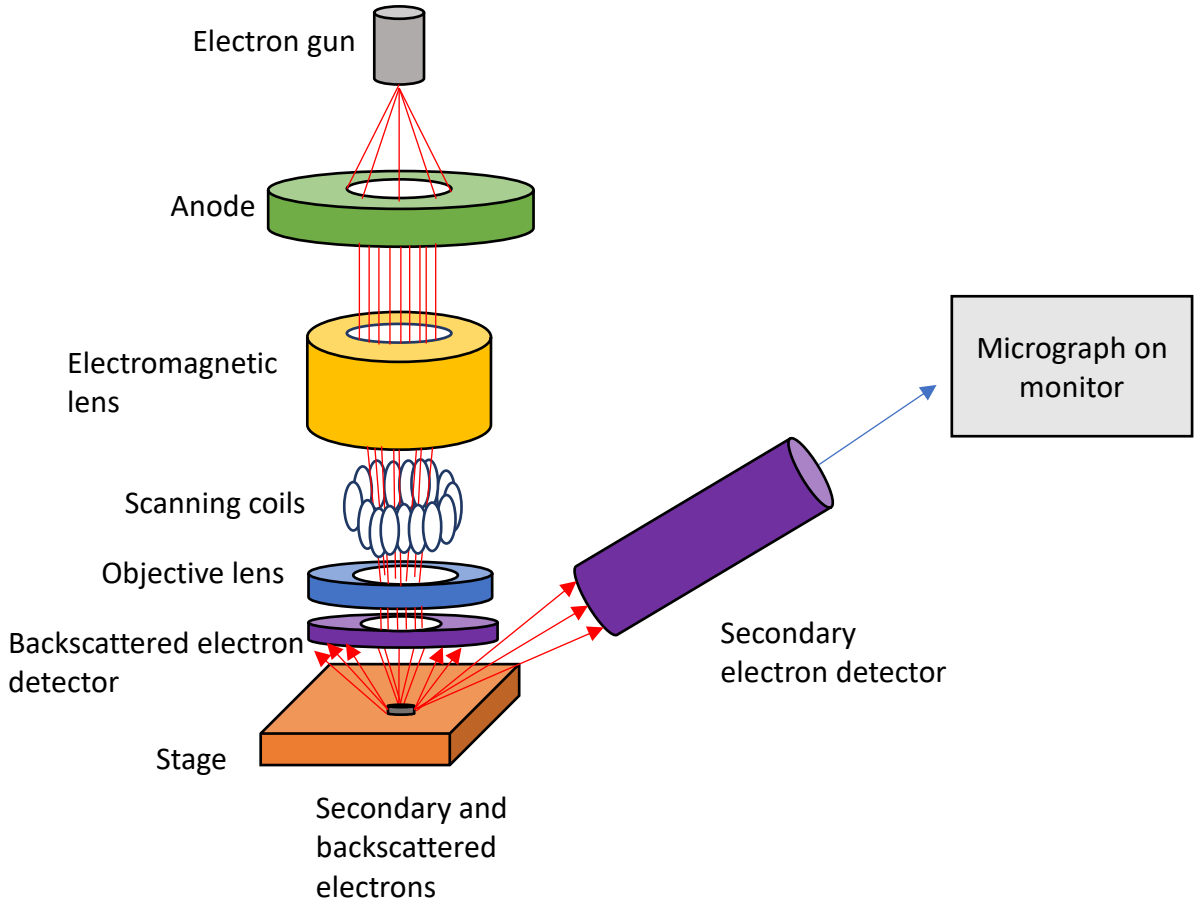

Figure 2-2: Schematic of a Scanning Electron Microscope. Energy dispersive X-ray (EDX) analysis was used in order to analyse various particle morphology and determine the elemental composition of the samples.

High-resolution transmission electron microscopy (HR-TEM)

High-resolution TEM allows for the study of nanoparticles, crystal structure, atomic diffraction and quantitative elemental mapping using energy dispersive x-ray.

To analyse in greater detail the morphological and elementary study of the Pt on the sample, HR-TEM imaging is carried out by the FEI Titan Themis instrument, using a 25 keV He^+ beam with 0.2 pA beam current. The elementary study through the energy dispersive X-ray (EDX) are also performed by spot and mapping analysis to distinguish the Pt NPs on the sample surface compared to the desired perovskite compositions (La, Ca, Ba, Pt, Ti and O).

Physisorption

'Physisorption' is the term used to describe the physical adsorption of gas molecules onto the surface of a material. Often in the case of heterogeneous catalysis, nitrogen physisorption is used in order to determine the surface area, micro-, meso- and macro-porosity, as well as the ordered/disorder porous nature of the sample itself. Nitrogen is used, as the temperature of adsorption for most solid-state oxide materials is below freezing point. The adsorption isotherm is the measurement of the amount adsorbed versus adsorptive pressure at constant temperature.

A micrometrics TRISTAR II 3020 was used in order to determine porosity, and each sample was calcined at 150°C under a vacuum in order to remove any water-bound molecules from the sample. A nitrogen isothermal data set for adsorption and desorption was collected at -195°C.

Thermal gravimetric analysis

Thermogravimetric analysis determines the weight change of a sample by changing the thermal profile in a selected atmosphere. Thermogravimetric analysis of samples was performed using a NETZSCH TG1000M in an argon flow atmosphere at 3°C/min using Proteus thermal analysis software.

Thermogravimetric analysis (TGA)

TGA measurements are carried out on a NETZSCH STA 449 C instrument using Proteus thermal analysis software. The initial weight of the sample is about 20 mg. The buoyancy effect is corrected using empty crucible blank runs under corresponding chemical reduction gas atmosphere of flowing 5% H_2/Ar (30 ml/min). First, the sample is heated to 1000 °C with a heating rate of 5 °C min^{-1}. Second, the sample is heated to 700 °C with a heating rate of 5 °C min^{-1} and kept for 15 hrs.

XANES EXAFS

X-ray absorption spectra (XAS)

The X-ray absorption near edge structure (XANES) is technique local to elemental structure. Its main uses is for understanding the elemental valence state and oxidation chemistry. The technique can only be performed with high energy X-ray's and therefore takes place in synchatrons.

The X-ray absorption near edge structure (XANES) and extended X-ray absorption fine structure (EXAFS) of the Pt L_{III}-edge for selected samples are collected at ambient temperature, on the B18 station at the Diamond Light Source national synchrotron facility, UK. Measurements are carried out using a Si(111) monochromator at Pt L_{III}-edge with a Pt monometallic foil (10 μm) used as an energy calibrant. Samples are pressed into 13 mm pellets, and high Pt loaded samples are diluted using the appropriate amount of cellulose binder. Pt foil and PtO_2 are used as references for Pt^0 and Pt^{4+}, respectively. XAS data analysis was carried out with the software of Athena and Artemis.

EXAFS fitting

The EXAFS functions were Fourier transformed in the *k* range of 3–13.86 $Å^{-1}$ and multiplied by a Hanning window. The basic structural model was a (fcc) Pt metal core from the ICSD code of 243678. The structure refinement was carried out using ARTEMIS software (IFFEFIT). Moreover, the

theoretical backscattering amplitudes and phases were calculated by FEFF 6.0. Then, the theoretical data corresponding to the first Pt–Pt shell were adjusted to the experimental spectra by a least square method in R-space from 1.8 to 3.12 Å. The amplitude reduction factors (S_0^2) were calculated using the Pt foil model, based on the coordination number (*N*) of 12. The other fitting parameters were σ^2 (Debye-Waller factor: mean square deviation of interatomic distances); *R* (Average interatomic distance, R_{eff}: 2.77410 for Pt-Pt); and ΔE0 (Energy shifts: inner potential correction between the samples and the FEFF calculation). The R-factor represents the absolute misfit allowed for the data range that were fitted between theory and experiment. The number of the independent points according to the Nyquist criterion was 8.86, and the number of the fitting parameters was 4.

XPS

The O 1s XPS spectra are collected by a thermo Scientific K-Alpha instrument equipped with a monochromatic Al X-ray source (Al Kα, 1486.6 eV), using a hemispherical energy analyser. The samples are fixed on carbon tape, and all binding energies are calibrated using C 1s (284.8 eV). The results are analysed and fitted using Fityk software by a linear type background subtraction and appropriate curve shape fitting.

Initial lab-scale tests on catalytic CO oxidation and stability aging

The catalytic performances of as-synthesised samples for CO oxidation are evaluated in a laboratory scale fixed–bed quartz reactor (internal d8 mm) under atmospheric pressure. The temperature is controlled by the K-type thermocouple at the centre of the reaction zone, and gas flows are controlled by the electronic mass-flow controllers (MFC, ALICAT scientific). Approximately 200 mg of samples are grounded and sieved to 40-60 mesh to load into the reactor by quartz wool at each side. The samples are pre-treated in-situ with 5% H_2/Ar at 300 ^oC for 1 hr, and then purged with N_2 for 30 minutes to remove the residual H_2. After cooling to 70 ^oC, a feed mixture gas of 20,000 ppm CO, 10.0 vol.% O_2

from air (21% O_2 and 79% N_2) at N_2 balance is introduced with a total gas flow rate of 200 ml·min^{-1} (GHSV=60,000/hr). The light-off experiments are measured at the range of 70-300 ^oC with a ramp rate of 3 $^oC \cdot min^{-1}$, with sampling performed every 10 ^oC. At a fixed CO concentration and GHSV, the oxygen partial pressures for CO oxidation reaction are varied by 1, 5 and 10 vol.% O_2 from air (21% O_2 and 79% N_2). The composition of the effluent gas products is measured by on-line TCD gas chromatography (GC-2014, SHIMADZU) equipped with a molecular sieve 5A (60-80 mesh) column. The CO conversion is calculated by the change of the CO concentrations. In-situ aging tests for the initially tested catalysts are performed at 800 ^oC under an air gas flow of 50 ml·min^{-1} for over 2 weeks (around 350 hrs). The aged samples are then re-run through light-off experiments at the same reaction conditions. Post-characterizations of the aged samples are carried out by SEM analysis and particle tracking.

Real car exhaust conditions

To evaluate the catalysts in realistic environments, CO+NO redox, diesel oxidation and ammonia slip reactions are tested. The CO+NO redox model reaction was designed to evaluate the materials for the three-way catalytic converters. The tests were carried out in a temperature-programmed, fixed-bed reactor by ramping up the temperature from 90 °C to 500 °C at a rate of 10 °C/min and using 0.2 g of catalyst mixed with 0.2 g of cordierite. The inlet concentrations were fixed to the concentrations of 4000 ppm CO and 4000 ppm NO, respectively, at a total flow of 12 L/min at N_2 balance. A diesel oxidation catalyst (DOC) model reaction was used to evaluate the use of the materials for real automotive catalytic converters. The tests were carried out in a steady state temperature-programmed reactor at the temperature range of 150 °C to 330 °C with a 10 minute hold at each temperature stage. The total flow was 12 L/min at N_2 balance with the gas composition of 1450 ppm CO, 105 ppm propylene (C_3H_6), 125 ppm NO, and 4.5% CO_2, 10% O_2 and 5% H_2O (steam). The purpose of the ammonia slip reaction is to evaluate the possibility on removing excess NH_3 from the non-catalysed NH_3. Steady state temperature-programmed reactions *were* carried out from 150 °C up to 330 °C with

a 10 minute hold at each temperature stage. Inlet conditions were 550 ppm NH_3, CO 220 ppm with 4.5% CO_2, 10% O_2 and 5% H_2O (steam) at the N_2 balanced total flow of 12 L/min. For the gas products analysis on each reaction, both inlet and outlet gases were measured by an MKS MG2000 multi-gas analyser using a FT-IR detector. The conversions are calculated by the change of each gas concentration, and the light-off curves were plotted from the conversion values at each temperature stage.

CHAPTER 3 CRYSTAL STRUCTURE

3.1 Studying crystallinity to form a Pt-containing perovskite

Outline, task and storyline

As previously discussed, it is very hard to incorporate Platinum (Pt) into the crystal structure of a perovskite, although previous research has suggested that Pt can be incorporated into a host lattice, it has been noted in this work that it is hard to stabilise Pt metal, especially by using solution chemistry synthesis (through combustion synthesis).

In order to design and tailor a perovskite that can host Pt metal within its crystal structure, a simple methodology was devised as shown in Figure 3-1:

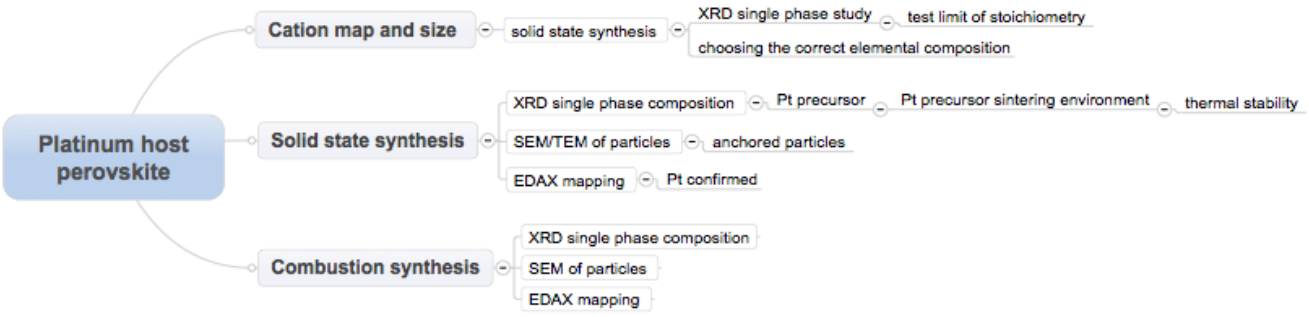

Figure 3-1: The following characterization methodology was devised to study the compositions made.

Tailoring the stoichiometry

In order to achieve a host perovskite lattice with the ability to exsolve/migrate B site cations to the surface of the material, a sub-stoichiometric host lattice was developed based on previous work by Dragos Neagu.[51] A-site deficient $La_{0.4}Sr_{0.4}TiO_3$ was used as the base composition to begin working with initially, due to its widely-studied characteristics and its reported composition shown in previous work by the Daihatsu Motor Corporation. Three new, well characterised compositions were created during

this work and will be discussed at length: $La_{0.4}(Ca/Sr)_{0.3925}Ba_{0.0075}Pt/Pd_{0.005}Ti_{0.995}O_3$ (noted as Pt@L(C/S)T or Pd@LCT).

Sub-stoichiometric or non-stoichiometric perovskite display a proven advantageous defect chemistry that can aid in catalytic chemistry. Cation substitution and the exposure of the material to various conditions such as partial O_2 pressure and temperatures result in the ability to widely tailor the ABO_3 perovskite formulae to sub-stoichiometric A-site deficient $A_{1-\alpha}BO_3$ renders A-site deficient perovskite the ability to have a wide array of properties that can be formulated are endless. Doping both the A and B site with charge balance between the sites can result in an A-site deficient oxygen stoichiometric material $La_xSr_{1-3x/2}Pt_yTi_{1-y}O_3$. Reduction in low p_{O2} (in H_2 atmospheres) and high temperature (above 500°C) oxide ions can migrate B site cations to the surface of the material and be semi-hosted in the lattice by intramolecular forces, resulting in oxygen vacancies. The B site cation in the studied compositions supported two oxidation states, Pt^{2+} and Ti^{4+}, resulting in a reduction that allowed the perovskite to develop oxygen vacancies but hold its electron structure during reduction.

Cation map, size and perovskite host cation tolerance

The oxidation states (charge) of selected cations and the radius size of the A and B site dopant are major factors when considering the tailoring of an A-site deficient composition's structure. The cation size is a direct indication of A and B site occupancy. Generally, B site cations are significantly smaller than A site cations as can be seen in Figure 3-2. A site cations are categorically larger and generally have a higher co-ordination number, whilst B site cations are smaller and occupy lower co-ordination numbers.

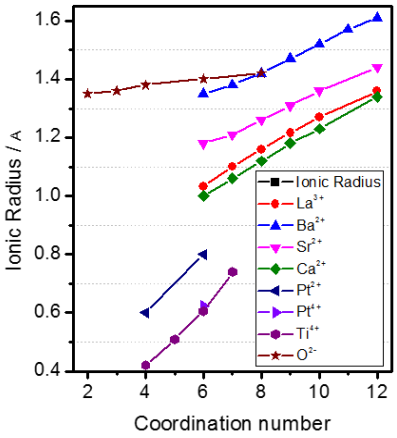

Figure 3-2: The cation map of selected cations shows the size of A and B site cations selected in this study. Notably Pt cations are considerably large for A and B site occupancy, indicating a large unit cell size is needed to accommodate Pt. Ba a large A site cation was chosen as an expansion cation in order to accommodate this.

With the aim to eventually incorporate Platinum onto the B site cation, barium was chosen as a good A site cation to complement the change in unit cell size. Perovskite stoichiometry $La_xBa_ySr_{(1-3x/2)-y}Ti_1O_{3-\delta}$ was chosen to determine the levels of barium doping that can be achieved, with the view to then using barium platinate ($Ba_3Pt_2O_7$) as a co-precursor to incorporating both platinum and barium on the A and B sites, respectively.

As platinum has a larger coordination number than that of most B site cations, it is important to tailor the larger A site cation to create a large enough unit cell that will eventually fit the larger B site Pt cation within it. Figure 3-2 shows the larger ionic size of barium compared with both lanthanum and strontium. Due to barium's overall larger ionic size, it is important to study the unit cell of $La_xBa_ySr_{(1-3x/2)-y}Ti_1O_{3-\delta}$ to determine both the distorted cell size and the phase purity, as well as the limit at which we can incorporate Ba.

Crystallographic determination and structure solving from X-ray diffraction

The identification of crystal structures for XRD spectra had been based on the notations described by Glazer.[80] The ideal pervoksite is cubic in structure; however, this can change based on the octahedral tilting and the cation displacement and mismatch. Glazer noted 23 possible octahedral tilt systems and duly gave them a memorable method to work out and describe each one through three letters noting the

pseudo cubic axes [100], [010] and [001] (abc) and direction of tilt through superscript '+', 'o' or '-' (positive phase, no phase and negative phase). In the case of unequal tilting, ***abc*** would be the notion; for equal amounts of tilt, ***aac*** would be the notion. '+' in-phase tilting around a given system indicates all the octahedra would be tilted on the same axis and direction; '-' out-of-phase tilting would result in the opposite. An example of in-phase tilting on three separate axes would be $\boldsymbol{a^+b^+c^+}$**.** Howard and Stokes later reviewed and modified the 23 classified tilt systems by Glazer, narrowing down the range to 15 tilt systems shown in Table 3-1.[81]

Glazer tilt system	Space group	Degrees of freedom
Group A: *High-symmetry*		
$a^0a^0a^0$	$Pm\bar{3}m$	1
$a^-a^-a^-$	$R\bar{3}c$	3
$a^0a^0c^-$	$I4/mcm$	3
$a^0a^0c^+$	$P4/mbm$	3
$a^0b^-b^-$	$Imma$	6
$a^-b^+a^-$	$Pnma$	10
Group B: *Multiple A-site tilt systems*		
$a^+a^+a^+$	$Im\bar{3}$	3
$a^0b^-c^+$	$Cmcm$	10
$a^0b^+b^+$	$I4/mmm$	5
$a^+a^+a^-$	$P4_2/nmc$	8
Group C: *Low symmetry tilt systems*		
$a^-a^-c^-$	$C2/c$	9
$a^0b^-c^-$	$C2/m$	10
$a^-b^-c^-$	$P\bar{1}$	18
$a^+b^-c^-$	$P2_1/m$	18
$a^+b^+c^+$	$Immm$	9

Table 3-1 shows the glazer tilt system and the symmetry groups with the corresponding superscript. Defect chemistry from A-site deficient perovskites can be classed into three major crystallographic areas: tilting of anion octahedra, a displacement cation in two planer directions and the distortion of the octahedral as a result of cation size. In order to explain this further, two things must be considered: the unit cell length and the unit cell angle. $SrTiO_3$ is typically described as the archetypal perovskite structure, displaying a cubic structure, as the lattice parameters for a single unit ABO_3 cubic cell is similar. V_{uc} is the volume of the distorted cell, and n_{uc} is the number of units within the cell itself. ap= a_{SrTiO3} =3.905Å

$$ap = \sqrt[3]{\frac{V_{uc}}{n_{uc}}}$$

Both tetragonal and orthorhombic cell defects and distortions can be related to the primitive unit cell or psedo cubic unit cell parameter by a_p; $a_p \ x \ a_p$ x a_p (cubic) $\sqrt{2_{ap}} x \sqrt{2_{ap}} \ x \ 2_{ap}$ (tetragonal) and $2_{ap} \ x \ 2_{ap}$ x 2_{ap} (orthorhombic).

In order to summarize space groups, Miller indices need to be assigned to the unit cell a_p, which can be estimated using the following equation:

$$d^2 = \frac{a^2}{h^2 k^2 l^2}$$

Step 1

The first peak chosen is usually (220) in perovskites, which is the strongest reflection occurring in the range o 30-32°θ, and can be calculated by:

$$d^2_{(220)} = \frac{(2_{ap})^2}{2^2 + 2^2 + 0^2} = \frac{a_p^2}{2} => a_p \approx \sqrt{2} \cdot d_{(220)}$$

Step 2

The main perovskite peak should have a Miller indices with all even numbers noted as eee (even even even), which is also known as the sub-cell peak and is present in all perovskite XRD patterns. Based on this first 220 peak the selection list can be generated and indexed using software (WinXPOW).

The next step is to examine the peaks and check for distortion. If the main peaks show some splitting or total splitting, it is a good indication of the crystal system being distorted and therefore not cubic. In order to determine the level of distortion, the following rules can be applied, as shown in Figure 3-3.

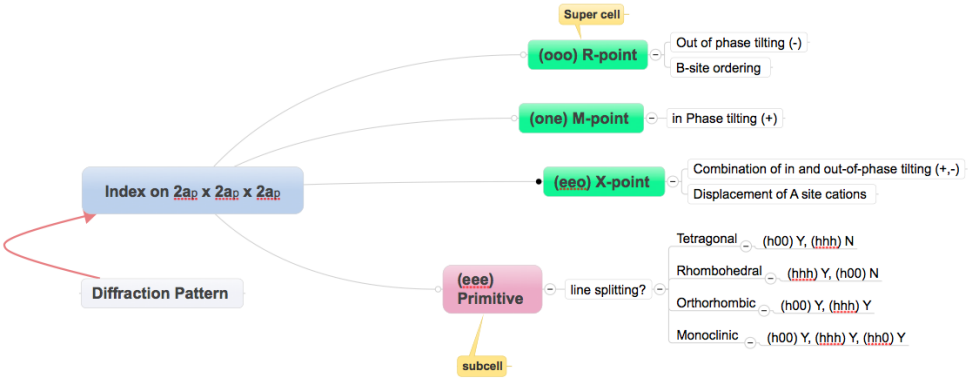

Figure 3-3 shows the methodological process used to calculate the space group and symmetry from Glazer superscript formulae.

(h00) peak split, (hhh) not split =tetragonal

(hhh) peak split, (h00) not split= rhombohedral

(hhh) peak split, (h00) peak split= orthorhombic

(h00) peak split, (hh0) peak split, ((hhh) peak split = monoclinic

From this methodology, one can determine the perovskite structure accurately and further determine tilting of the octahedra. Further confirmation can then be done through Rietveld refinement of the crystal system to validate claims.

Crystal structure of $La_{0.4}Sr_{0.4}M_yTi_{1-y}O_{3-\gamma}$ derived compounds

Initially, in order to study the effects of additional cation introduction and size on the base, $La_{0.4}St_{0.4}TiO_3$ $La_{0.4}Sr_{0.4}M_yTi_{1-y}O_{3-\gamma}$ was prepared by varying x and M (metal dopant).

The main objective of this work was to see if platinum group metals could be incorporated into wholly a crystalline lattice. With regards to the cation size, as previously mentioned in figure 3-2, Pt as a B site cation is larger than most B site cations for example Ni in comparison (0. 49a.u) to Pt (0.8a. u). With that in mind, we considered the first expansion of the unit cell using a large A site cation (Ba) to accommodate the larger B site cation. By expanding the unit cell size, we were able to understand the dopant levels we could possibly achieve.

The formulae for the derived compounds previously represented by D. Negau[82] allows for charge balance of the A site and B site cations in relation to O site stoichiometry.

$$La_xSr_{0.4-(4-m)\cdot x}M_x^{m+}Ti_{1-x}O_3 = La_{x+(4-m)\cdot y}Sr_{1-\frac{3x}{2-(4m)}\cdot y}M_y^{m+}Ti_{1-y}O_3$$

$La_{0.2}Ba_ySr_{0.7-y}TiO_3$ with barium doping from 1-10% was prepared by a modified conventional solid-state synthesis, as mentioned previously. The pressed pellets prior to sintering showed some discoloration due to the incorporation of increased barium. The pellet on the far left of Figure 3-4 shows $La_{0.2}Ba_{0.09}Sr_{0.61}TiO_3$ and the far right $La_{0.2}Ba_{0.02}Sr_{0.68}TiO_3$. This could be due to the particle size resulting in enhanced optical properties of the pressed pellets, the increased amount of $BaCO_3$ precursor material and the oxidation of the material during the ball milling step.

After sintering at 1450℃, both the colour change and mass lost are visible in Figure 3-5.

Figure 3-4

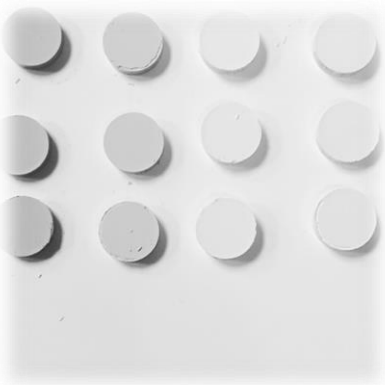

Figure 3-5

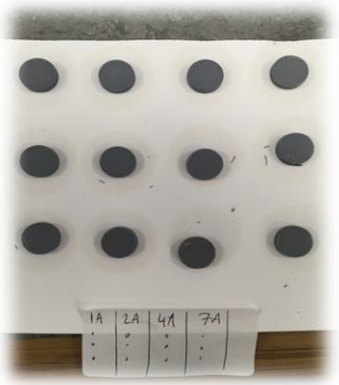

Figure 3-4 shows the change in colour of pressed pellets with the more Barium incorporated.
Figure 3-5 shows the pellets after the sintering process.
The mass loss is attributed to the removal of carbonate precursors and any molecular water-bound molecules still present within the powder phase. After crushing the dense pellet in a pestle and mortar, PXRD analysis was then carried out on each sample using the method described previously.

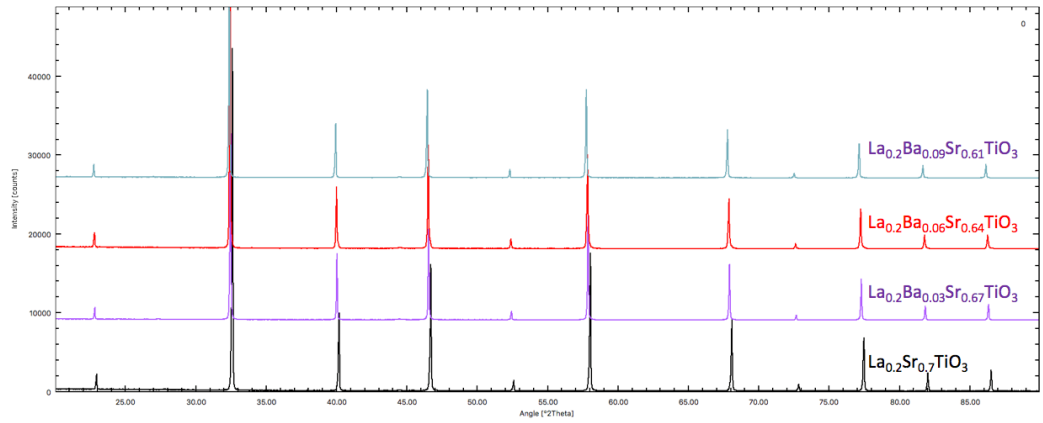

Figure 3-6a: XRD spectra of $\mathbf{La_{0.2}Ba_ySr_{0.7-y}TiO_3}$ with increasing Ba content.

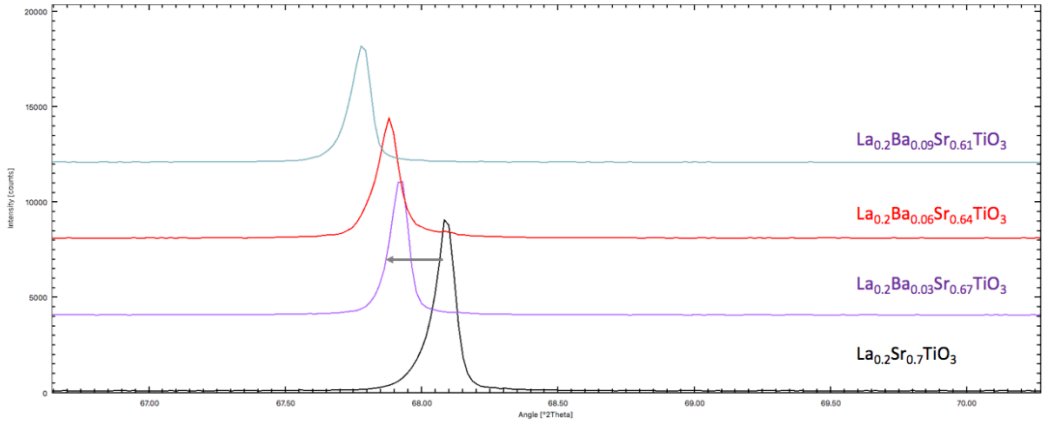

Figure 3-6b shows the $\mathbf{La_{0.2}Ba_ySr_{0.7-y}TiO_3}$ spectra shift to the right as the unit cell size increases.

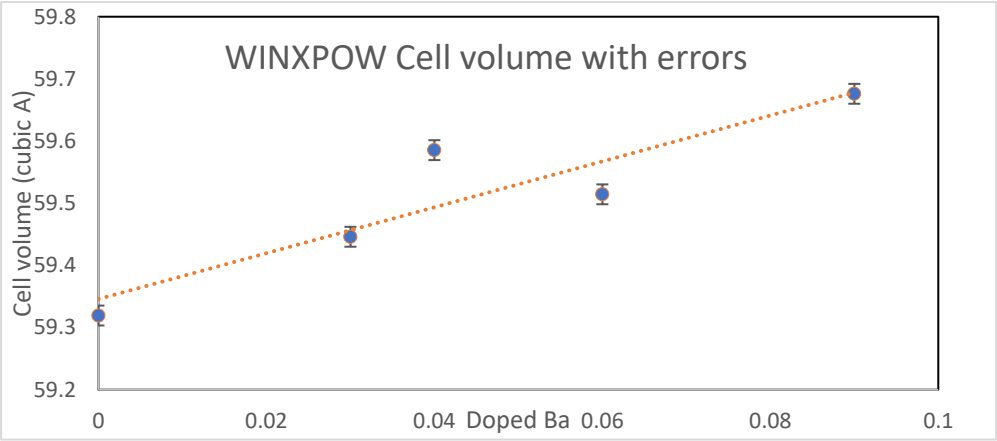

Figure 3-6c: The room temperature XRD patterns show that a single phase was obtained from all samples prepared. By further analysing the data using WinXPOW structural refinement software it was found that the crystal structure was Pm-3m pseudo-cubic structure. With increasing barium doping the unit cell size increased linearly. As can be seen in figure 14. The unit cell parameter increases from 3.90 to 3.9Å. Both WinXpow and GSAS were used to index the cell ,P m -3 m, cubic perovskite structure. Unit cell parameter a= 3.90 going to 3.91.The incorporation of Ba does not drastically affect the cubic structure. The unit cell size increases. Peak shoulder appears after 6% Barium doping

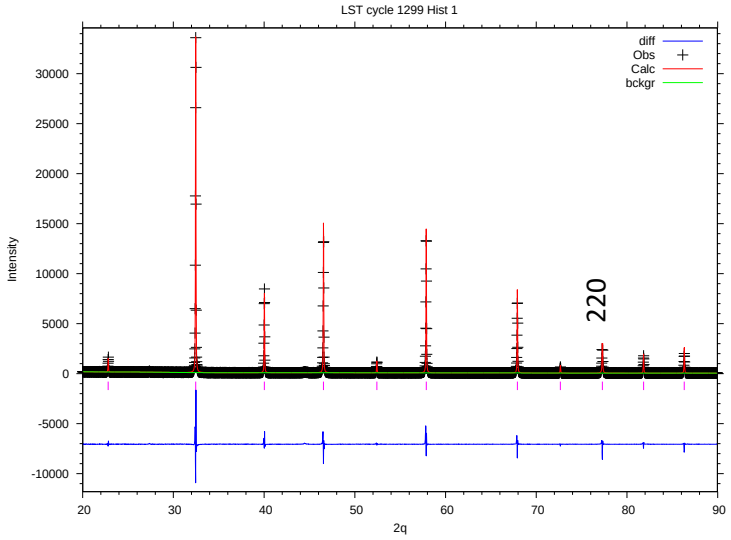

Figure 3-6d: The effect of barium had little overall significance on the pm-3m pseudo cubic structure, although some octahedra out-of-phase tilting was evident from the peak shape (220).

The incorporation of Platinum

As discussed in chapter 1, typically, attempts at the incorporation of PGMs into crystalline perovskite lattices have been made through sol-gel chemistry routes both for A site stoichiometric and A site deficient compounds. Although amorphous nanoparticles of Pt can form, upon reduction or exposure

to a temperature higher than 800°C, Pt metal starts to agglomerate and form metal clusters across the surface of the material. The crystalline structure of these compounds can be seen to have a strong peak at 38.9-40θ, indicating the presence of PtO_2 and or Pt metal, which in turn indicates the dissociation of Pt from the crystalline structure as seen in figure 3-7.

Initially, platinum nitrate was used as a simple precursor for sol-gel synthesis, and platinum oxide (PtO_2) was used as a precursor for the solid-state synthesis of $La_xBa_ySr_{(1-3x/2)-y}Pt_zTi_{1-z}O_{3-\delta}$ with z at 0.06-0.01. XRD spectra revealed peaks at 38.9-40θ, as shown in Figure 3-7.

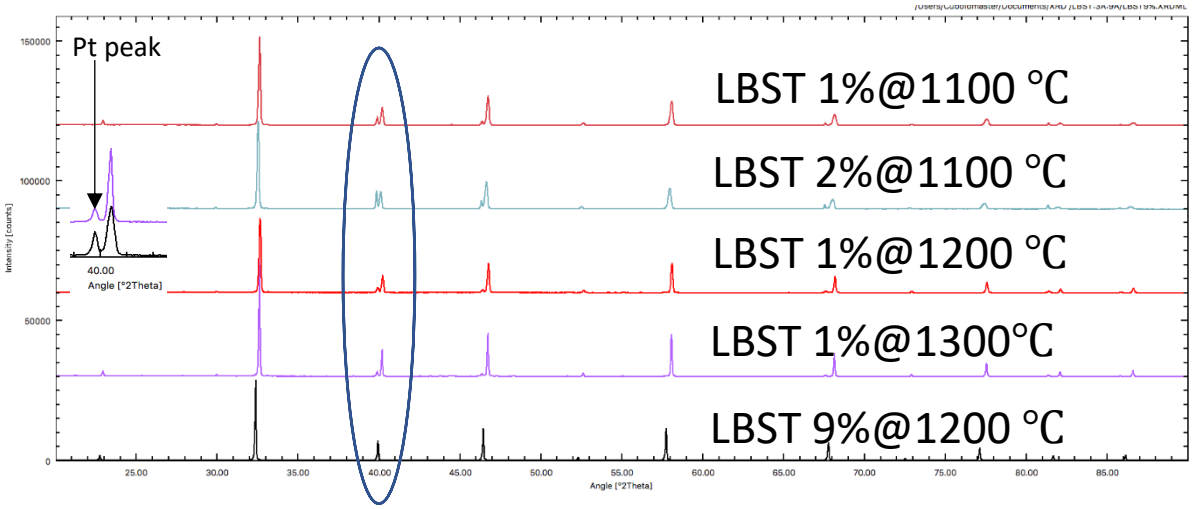

Figure 3-7: A selection of XRD patterns showing the crystalline phase of the perovskite. however, the noticeable peak of Pt metal at 38.9-40θ indicates the dissolution of Pt from the crystalline lattice before a reduction event, thus proving the dual-phase nature of the perovskite when synthesized in air at different temperatures. $La_xBa_ySr_{(1-3x/2)-y}Pt_zTi_{1-z}O_{3-\delta}$ (z=0.01) and LBST (LBST9%= $\mathbf{La_{0.2}Ba_ySr_{0.7-y}TiO_3}$ stoichiometric y=0.9).

The sintering environment in air and pure oxygen at temperatures from 1000-1500°C provided no further evidence of Pt incorporation into the perovskite, both through XRD and SEM analysis. Step-wise methodology was used to approach this problem, working first with sol-gel and then solid-state synthesis. One major challenge with the perovskite formation was the temperature of sintering (pellet and powder) to low >1200°C (the perovskite did not form from 12-100hr of sintering), and to high <1200°C (the perovskite formed a crystalline structure with the Pt disappearing in quantity from the bulk due to the evaporation of the Pt metal at high temperature and formation of un-anchored

nanoparticles at higher temperature <1300, which due to size and dispersion can be difficult to detect and see the intensity from XRD alone, due in part to the diffusion of Pt cations to the atmosphere, as will be discussed further in the following chapter).

Barium Platinate: A Trojan horse

Much like the subterfuge of the Greeks entering the city of Troy in a wooden horse, with the element of surprise and protection, the path to incorporating PGMs and, specifically, Pt into a crystalline structure at high temperature is deemed a technique of combining the new with the old. The concept of tricking the crystal structure into accepting Pt despite its cation size and mismatch required a combat on two major fronts:

1) The thermal stability of the Pt precursor
2) The cation size and makeup of the unit cell and incorporation of the precursor into a crystalline lattice.

First, it was deemed necessary to select a precursor that can be easily made, with a high thermal stability above the temperatures required for solid-state synthesis, in order to incorporate Pt atoms into the crystal lattice without its sublimation from the structure prior to the perovskite crystal structure being formed. Second, it is vital to choose a correct cation size for the precursor in order to tailor the A site deficiency of the perovskite and balance the charge.

Barium platinate ($Ba_3Pt_2O_7$), a compound first discovered in 1889 by Rosseau,[83] was later studied as a by-product of the Ba-TiO_2 system. Statton created the phase diagram (first mentioning hexagonal crystal-like structures after firing $BaCO_3$ in a platinum crucible[84]). It has also been studied as an analogue of the $Sr_3Ot_2O_7$ by Randal and Ward[85] and, finally, it underwent a structural study in 1977 by P. S. Haradem.[86] There are many forms of Platinate compounds containing a variety of cations. By far the easiest and simplest to synthesize is $Ba_3Pt_2O_7$, simply by mixing the correct stoichiometric amounts of $BaCO_3$ and PtO_2 (3:2 ratio) in a platinum crucible and firing it for 12 hours at 1000°C.

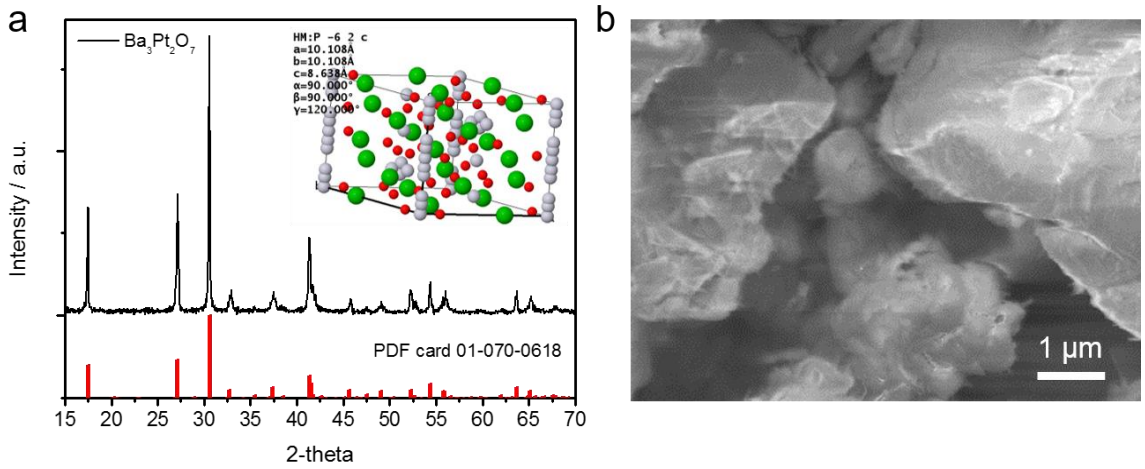

Figure 3-8: Trojan horse $Ba_3Pt_2O_7$ characterization. (a) X-ray diffraction pattern in the case of laboratory made $Ba_3Pt_2O_7$ which well matched with the PDF card of 01-070-0618 and Inorganic Structural Database (ICSD); and (b) SEM image of the $Ba_3Pt_2O_7$ co-precursor.

It is incredibly challenging to control Pt due to the reducing nature of Pt by the Pt metal dissociation from PtO_2 at ≥400 ^oC and its melting/sublimation in air at high temperature.

Used as a Trojan horse co-precursor, a thermally stable Pt compound of $Ba_3Pt_2O_7$ was synthesized by solid-state synthesis, which is capable of withstanding the high temperatures required to form a perovskite phase up to 1250°C (Fig. S1). In doing so, it is possible to sneak Pt into the perovskite crystal structure in an O_2-rich environment, further lowering the temperature of single-phase formation without the inherent separation of Pt (Figure 3-16). Therefore, it is co-doped by Pt on the B site and Ba on the A site, respectively. Two different A-site deficient perovskite materials of $La_{0.4}(Ca/Sr)_{0.3925}Ba_{0.0075}Pt_{0.005}Ti_{0.995}O_3$ were designed by fully incorporating g 1-0.5 wt.% of Pt into the crystal perovskite structure.

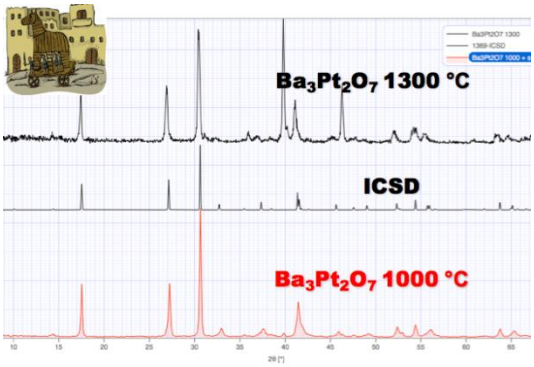

Figure 3-9a: $Ba_3Pt_2O_7$ XRD formed at 1000 and the crystal structure from ICSD and finally the decomposition of $Ba_3Pt_2O_7$.

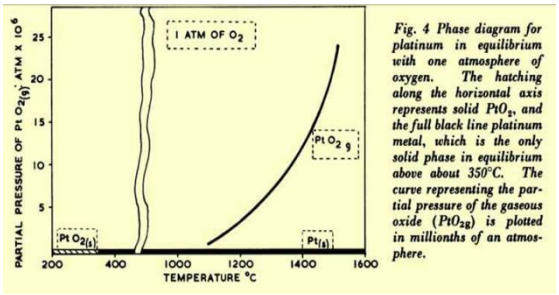

Figure 3-9b: The decomposition of PtO with an increasing temperature in 1atm of O_2. With permission from Johnson Matthey[87].

The thermal stability of $B_3Pt_2O_7$ results in the incorporation into a crystal structure being significantly easier than PtO_2, which starts to decompose at 450 ^oC. The thermal stability of $Ba_3Pt_2O_7$ was found to be 1250 ^oC, and full decomposition was found to occur at 1300 ^oC in air. Furthermore, $Ba_3Pt_2O_7$ remained stable in air without any crystallographic structural change to the compound.

Co-precursor

The idea of using a co-precursor for doping both the A and B sites simultaneously is complex, as the effect on the stoichiometry is dependent on the cation ratios of the A and B site within the composition and can further render the structure formulae difficult to make. During the synthesis process, Ba cations

move to the A site, and Pt to the B site at 1220 °C. The cation size itself of $Ba_3Pt_2O_7$ is a limiting factor in the amount (wt%) of platinum that can be incorporated into the crystal structure without dissolution depicted in Figure 3-11. This was confirmed with 3-1%wt Pt for both Pt@LCT and Pt@LST, which were found to have formed Pt metal within the bulk below 1000 °C after synthesis in oxygen and air, indicating that the Pt dissociated and did not migrate to the crystal structure, but rather, it formed Pt metal as seen in Figure 3-10.

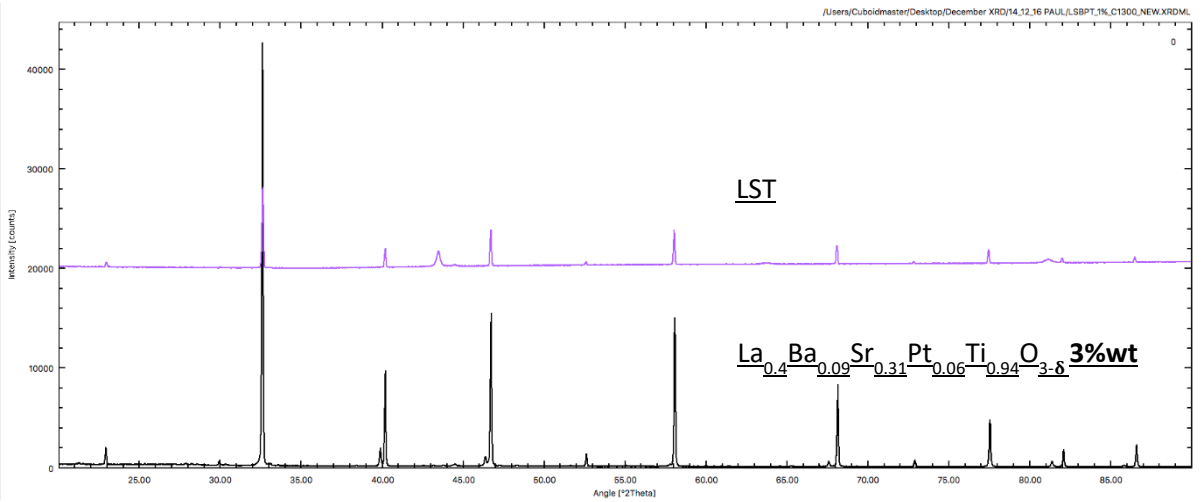

Figure 3-10: XRD of $La_{0.4}Ba_{0.09}Sr_{0.31}Pt_{0.06}Ti_{0.94}O_{3-\delta}$ 3%wt, whereby Pt metal has formed within the structure. Pt peak at 39.9θ.

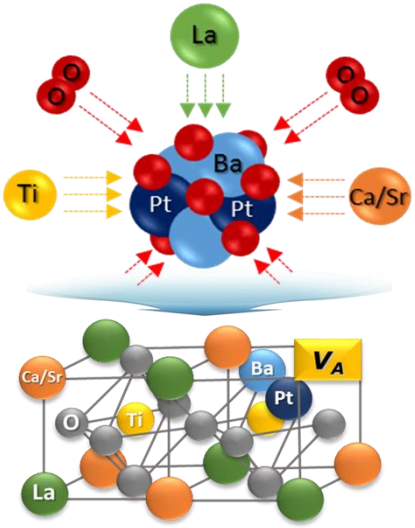

Figure 3-11 depicts the migration of barium palatinate to the perovskite to form a single phase crystal structure.

Using 0.5wt% Pt the crystal structure of: $La_xBa_ySr_{(1-3x/2)-y}Pt_zTi_{1-z}O_{3-\delta}$ formation in air

Using $Ba_3Pt_2O_7$ as a precursor, compositions of $La_xBa_ySr_{(1-3x/2)-y}Pt_zTi_{1-z}O_{3-\delta}$ were made with different firing temperatures to understand the dissolution of Pt into the lattice. It was found that the formation of the perovskite structure in air did not form fully crystalline compounds despite the decoration of nanoparticles (NPs) on the surface of the perovskite (as seen in chapter 4). These Pt NPs were detectable by XRD of the pellet and can be seen in Figure 3-12. The dissolution of Pt at lower temperatures >1200°C in air resulted in a strong peak at 38.9-40θ. The peak intensity decreased as the temperature increased, indicating two possibilities: either further dissociation of Pt from the crystal structure resulting in Pt nanoparticles forming over the perovskite surface, resulting in well dispersed small NPs (less than 1-5nm); or the evaporation of Pt metal from the structure at temperatures above 1400°C. The latter can be confirmed by the unit cell size calculations of the $La_{0.4}Ba_{0.016}Sr_{0.384}Pt_{0.01}Ti_{0.99}O_3$. In Figure 3-13, the decreasing unit cell size is an indication of the partial reduction and dissociation of Pt from the structure. Interestingly, Pt NPs only formed in air when $Ba_3Pt_2O_3$ was used as a precursor. The mobility of the Pt NPs was due to the dissociation of the metal from the crystal structure, which can be observed in SEM micrographs (as discussed in the following chapter). The formation of Pt NPs was a start and a good indication that it could be incorporated into the crystal structure; however, it was

deemed that the formation of the perovskite structure would have to occur at a temperature lower >1300 in order for Pt to migrate to the B site.

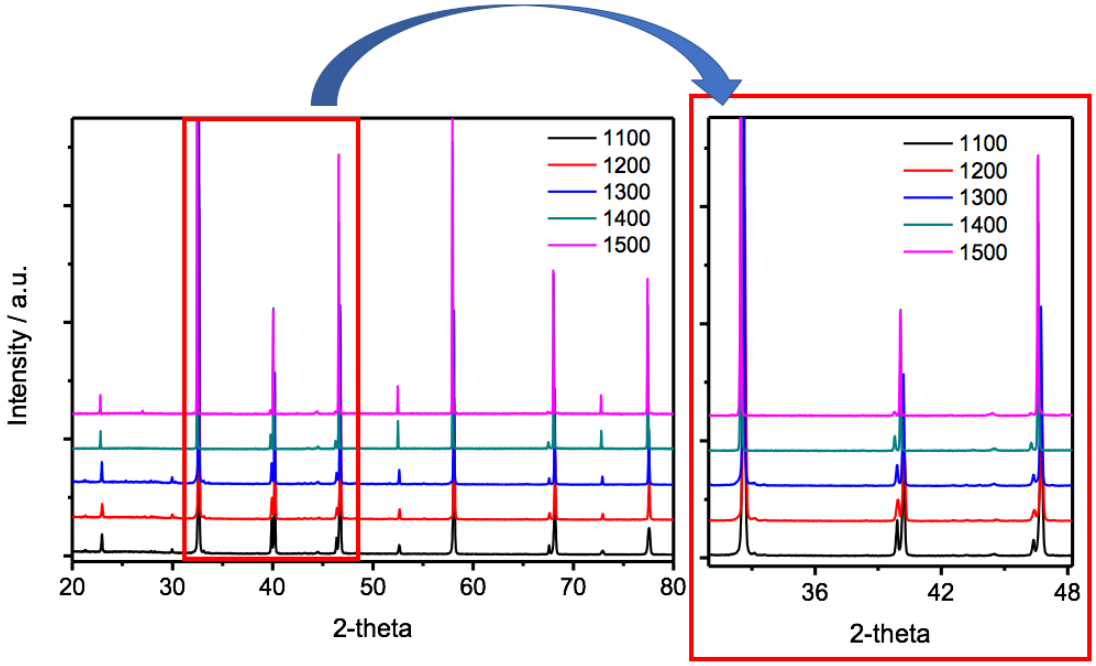

Figure 3-12: Perovskite formation with increasing temperature from 1100 to 1500°C: $La_xBa_ySr_{(1-3x/2)-y}Pt_zTi_{1-z}O_{3-\delta}$ formation in air.

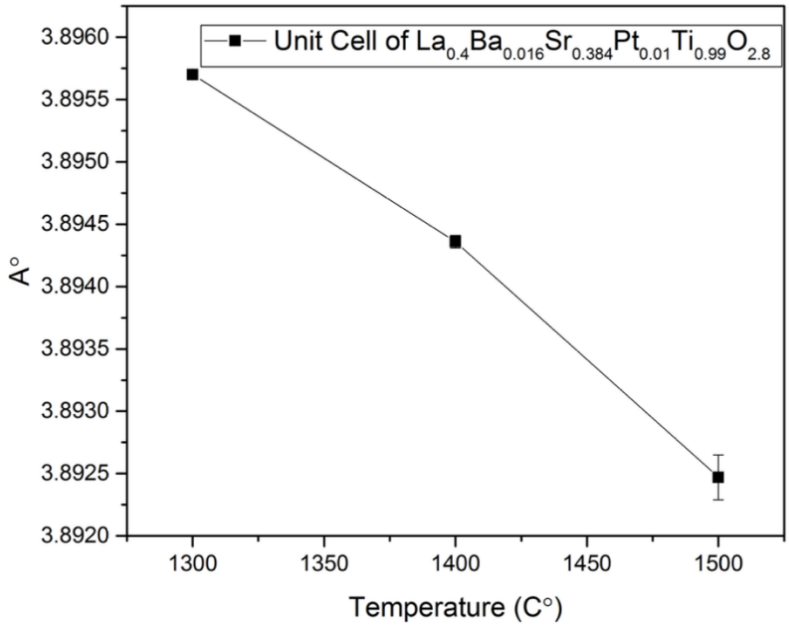

Figure 3-13 shows the unit cell size of $La_{0.4}Sr_{0.3925}Ba_{0.0075}Pt_{0.005}Ti_{0.995}O_3$ after formation in a pure oxygen environment.

To lower the formation of a crystalline perovskite the A-site deficient $La_{0.4}(Ca/Sr)_{0.3925}Ba_{0.0075}Pt_{0.005}Ti_{0.995}O_3$ compounds were synthesised in pure O_2 in a tube furnace. A step-wise temperature study was conducted to assess the temperature of perovskite formation in comparison to air. A pure perovskite phase was achieved at 1200°C.

The incorporation of Pt into the crystalline lattice of both Pt@LST and Pt@LCT of $La_{0.4}(Ca/Sr)_{0.3925}Ba_{0.0075}Pt_{0.005}Ti_{0.995}O_3$ in pure oxygen can be attributed to the saturated oxygen environment at high temperature (1200°C) and the permeation of O_2 gas through the crystal structure, forcing cation ordering due to the high partial pressure of O_2 (pO_2). Defect chemistry is controlled in a pure O_2 atmosphere where by grain boundary formation and diffusion of cations is slow and low ion mobility is created due to the excess O_2, resulting in the formation of the perovskite crystal at a lower temperature as well as keeping Pt oxidised rather than in a metallic form.[88,89] There is an oxygen scale that prevents the outward diffusion of cations from the perovskite, allowing for the formation of cation diffusion through the bulk of the perovskite.[90] The interaction of oxygen on $Ba_3Pt_2O_7$ needs to be studied further to understand the thermodynamic and kinetic damper on cation migration and the subsequent metallic formation of Pt_0 in air.

The XRD patterns of Pt@LST and Pt@LCT clearly show no observable peak at 38.9-40θ after formation in a pure oxygen environment above 1100°C. By studying the unit cell size from a reduced unit cell size parameter, calculated from WinXPOW refinement software, it was found that an increase in unit cell size and volume occurred upon the inclusion of Pt into the lattice, as shown in Table 3-1.

The space group was confirmed through Rietveld refinement and calculating the Glazer and Miller indices. A difference between both A site dopants Ca and Sr unit cell size and peak splitting/distortion of higher angle peaks resulted in three different space groups for Sr and Ca: LCT= *Ibmm,* LCBT=

I4/mcm, Pt@LCT= *I4/mcm* as depicted in figure 3-17, LST= *Pm-3m*, LSBT= *Pm-3m*, Pt@LSBT=*Pm-3m*.

From the perovskite peak shifts in Fig.4 and the refinement results, we can see that tetragonal Pt@LCT resides in an *I4/mcm* space group with a smaller unit cell size than that of cubic Pt@LST (*Pm-3m*) due to the difference in cation size between Ca and Sr (Fig.5). The crystal structure without Pt remains in a similar symmetry and space group, indicating that the incorporation of such a small amount of Pt has little effect on the crystal structure itself. However, it can be confirmed by the change in unit cell size with a small incremental increase. Due to the nature of the Ca cation being smaller than Sr by 0.2Å, the accommodation of a larger A site Ba cation further distorts the unit cell size, resulting in a change in structure and space group. Furthermore, the addition of an extra Pt cation on the B site results in a expanded unit cell size; however, enough within the system cell size limits to accommodate the cation within the unit cell parameters. As Sr has a larger cation size, both the incorporation of Ba and Pt can be accommodated within the *Pm-3m* unit cell. The increase in volume and unit cell size is a strong indication of the incorporation of Pt into the crystal lattice structure. Tetragonal out-of-phase tilting and distortion can be observed by studying the Miller indices from the A and B site cation ordering of the structure, in part due to the splitting and broadening of higher angle reflections, as well as the effect of the size of the smaller Ca cation. This can be observed from the Rietveld refinement of Pt@LCT, which is a good fit, as shown in Figure 3-16.

	$La_{0.4}Ca_{0.4}TiO_3$	$La_{0.4}Ca_{0.3925}Ba_{0.0075}TiO_3$	$La_{0.4}Ca_{0.3925}Ba_{0.0075}Pt_{0.005}Ti_{0.995}O_3$	$La_{0.4}Sr_{0.4}TiO_3$	$La_{0.4}Sr_{0.3925}Ba_{0.0075}TiO_3$	$La_{0.4}Sr_{0.3925}Ba_{0.0075}Pt_{0.005}Ti_{0.995}O_3$
	Ibmm[a]	*I4/mcm*	*I4/mcm*	*Pm-3m*	*Pm-3m*	*Pm-3m*
			Cell Parameter			
a/Å	7.7120	7.7287	7.7329	3.8802	3.8852	3.8911
b/Å	7.7278	7.7287	7.7329	3.8802	3.8852	3.8911
c/Å	7.7278	7.8120	7.8090	3.8802	3.8852	3.8911
β/°	90	90	90	90	90	90
Volume/Å^3	460.55	461.66	462.41	58.42	58.64	58.91

Table 3-2 shows the estimated crystallographic parameters from the powder X-ray diffraction data of literature and all the prepared perovskites taken at room temperature.

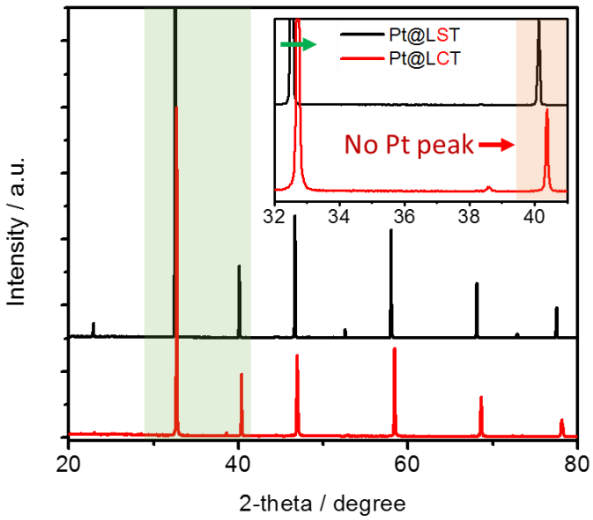

Figure 3-14 (above and below) shows the XRD (X-ray powder diffraction) spectra of both Pt@L(C/S)T with highly crystalline patterns. No visible metallic Pt peak can be observed at 38o-39.8o, indicating the incorporation of Pt into the crystal structure.

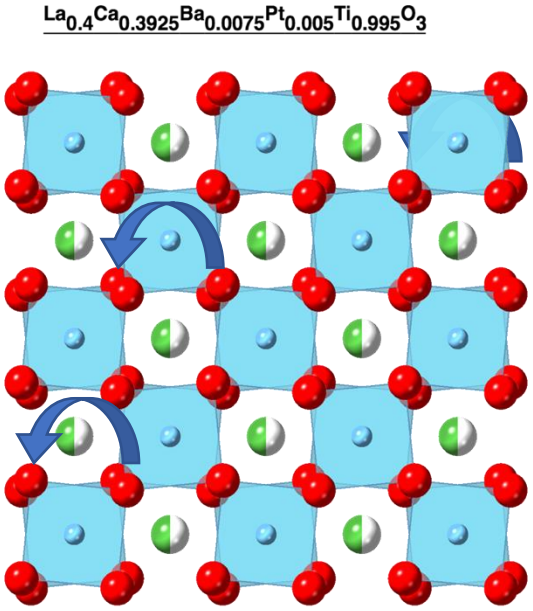

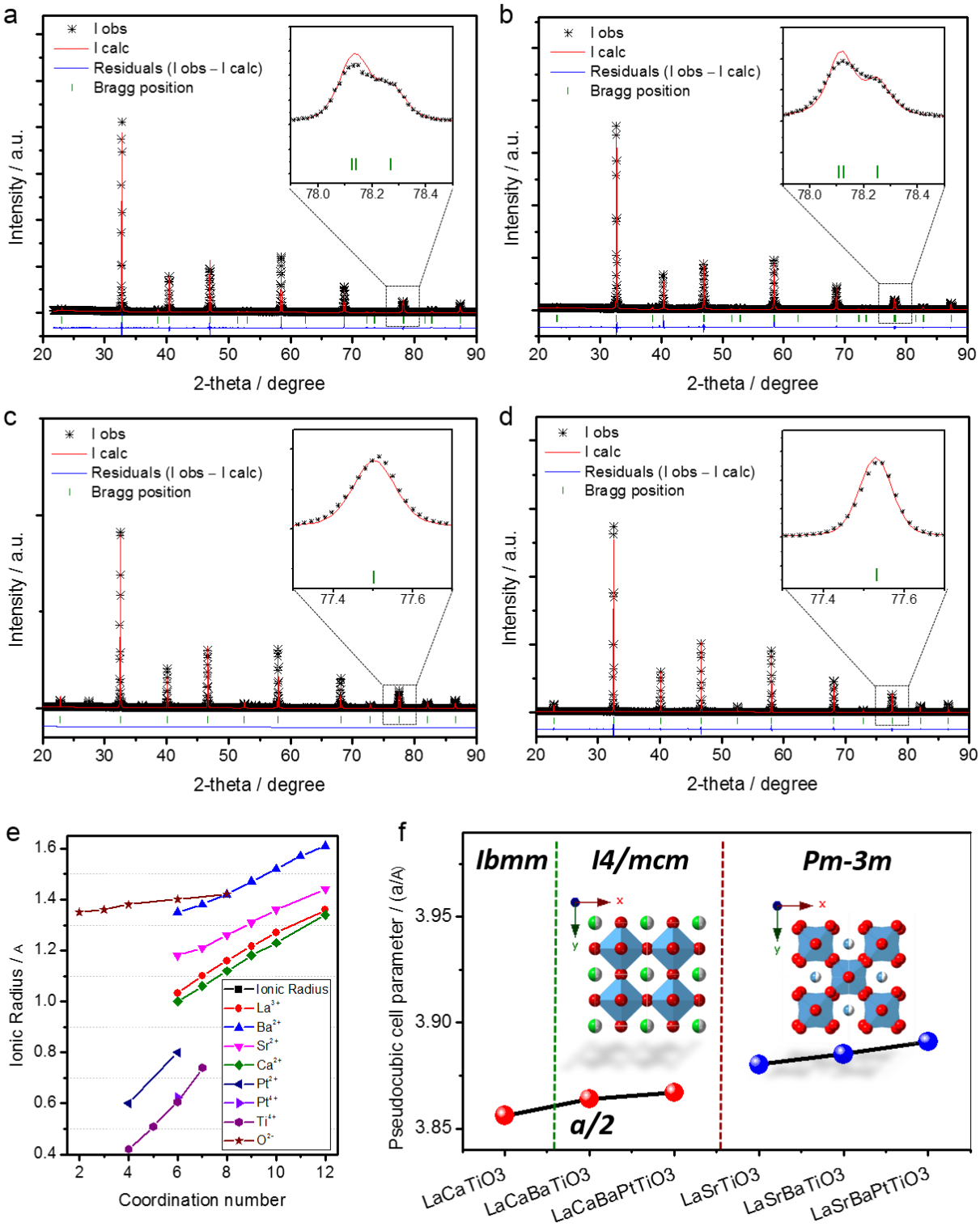
a
I obs
I calc
Residuals (I obs – I calc)
Bragg position
Intensity / a.u.
2-theta / degree
b
c
d
e
Ionic Radius / A
Coordination number
Ionic Radius
La3+
Ba2+
Sr2+
Ca2+
Pt2+
Pt4+
Ti4+
O2-
f
Pseudocubic cell parameter / (a/A)
Ibmm
I4/mcm
Pm-3m
a/2
LaCaTiO3
LaCaBaTiO3
LaCaBaPtTiO3
LaSrTiO3
LaSrBaTiO3
LaSrBaPtTiO3

Figure 3-15: Refined X-ray diffraction patterns using Rietveld analysis for (a) LCT, (b) Pt@LCT, (c) LST and (d) Pt@LST to investigate the structural difference. (e) Ionic radius versus coordination numbers for all used elements and (f) change of the cell parameters taken from literature and XRD analysis for all the prepared perovskites with crystal structure images for both tetragonal Pt@LCT and cubic Pt@LST from (b) and (d).

Crystallinity after reduction

Reduction in 5%H_2/Ar of all compositions was carried out at variable temperatures and times, as discussed in the following chapter. The exemplification of Pt emerging from the bulk lattice after a reduction event is evident from the XRD after reduction where by a Pt peak is observable for face centred cubic.

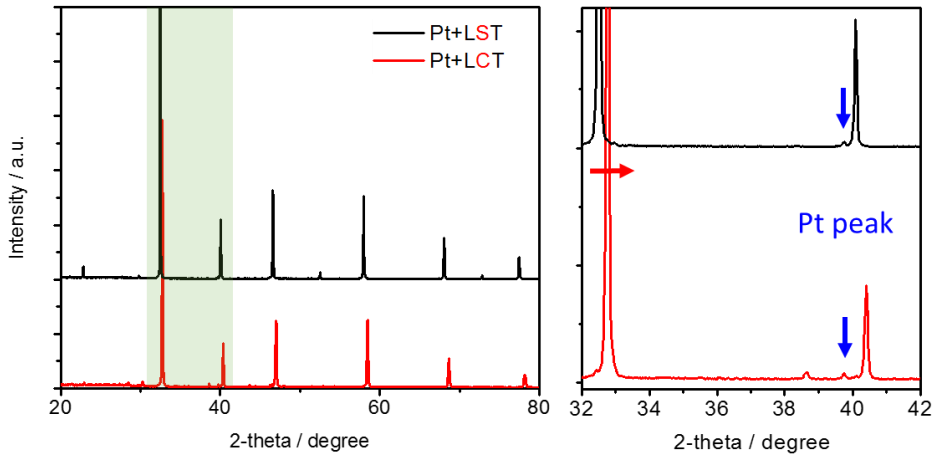

Figure 3-16 shows the XRD patterns (inset: magnification for 32o-42o) for the perovskites after Pt emergence, showing the well-defined, sharp reflections for face-centred cubic (fcc) Pt (38o-39.8o) (3). The perovskite peak shifts are due to the difference in cation size between Ca and Sr.

Summary and conclusion

By studying the crystal structure and cation size of a non-stoichiometric perovskite system it is possible to tailor the crystallinity and crystal structure of the perovskite system. In this work, incorporating just Platinum metal or PtO into the crystal structure does not yield a single crystal structure. Moreover, incorporating anything more than 1%wt Pt into a balanced

system does not allow for Platinum to be incorporated. Both Sol-gel and solid state techniques did not work for the incorporation of PtO. It was found that Barium Platinate significantly improves crystallinity and upon sintering in oxygen provides a fully crystalline structure in which Platinum is incorporated at high temperature. In conclusion this significant step of tailoring the cation size, correctly mapping the perovskite unit cell size, realising wt% maximums for larger cations and oxygen sintering have all contributed to making a fully crystalline non-stoichiometric Pt continuing perovskite system.

References

1. Galassi, G. & Spada, G. Sea-level rise in the Mediterranean Sea by 2050: Roles of terrestrial ice melt, steric effects and glacial isostatic adjustment. *Glob. Planet. Change* **123**, 55–66 (2014).
2. Rowley, R. J., Kostelnick, J. C., Braaten, D., Li, X. & Meisel, J. Risk of Rising Sea Level to Population and Land Area. *Eos, Trans. Am. Geophys. Union* **88**, 105 (2007).
3. Alley, R. B., Clark, P. U., Huybrechts, P. & Joughin, I. Ice-sheet and sea-level changes. *Science* **310**, 456–60 (2005).
4. Cox, P. M., Betts, R. A., Jones, C. D., Spall, S. A. & Totterdell, I. J. Acceleration of global warming due to carbon-cycle feedbacks in a coupled climate model. *Nature* **408**, 184–187 (2000).
5. Corma, A. & López Nieto, J. M. *The Role of Rare Earths in Catalysis*. *Handbook on the Physics and Chemistry of Rare Earths* **29**, (Elsevier, 2000).
6. BY se G. le. 3–5 (1973).
7. Cohn, J. G. Catalytic converters for exhaust emission control of commercial equipment powered by internal combustion engines. *Environ. Health Perspect.* **10**, 159–164 (1975).
8. Farrauto, R. J., Deeba, M. & Alerasool, S. journey to cleaner air. *Nat. Catal.* **2**, 603–613 (2021).
9. Eastwood, P. *Critical topics in exhaust gas aftertreatment*. (Research Studies Press, 2000).
10. Summers, J. C., Sawyer, J. E. & Frost, A. C. The 1990 Clean Air Act and Catalytic Emission

Control Technology for Stationary Sources. in *Catalytic Control of Air Pollution* **495**, 8–98 (American Chemical Society, 1992).

11. Libby, W. F. Promising Catalyst for Auto Exhaust. *Science (80-.).* **171**, 499–500 (1971).

12. Twigg, M. V. Progress and future challenges in controlling automotive exhaust gas emissions. *Appl. Catal. B Environ.* **70**, 2–15 (2007).

13. Russell, A., Epling, W. S., Russell, A. & Epling, W. S. Diesel Oxidation Catalysts Diesel Oxidation Catalysts. **4940**, (2011).

14. Twigg, M. V. Catalytic control of emissions from cars. *Catal. Today* **163**, 33–41 (2011).

15. Matthey, J. Johnson Matthey Annual Report 2018 - customers. (2018).

16. Misono, M. Mixed Oxides as Catalyst Supports. **176**, 157–173 (2013).

17. Tanaka, H. & Misono, M. Advances in designing perovskite catalysts. *Curr. Opin. Solid State Mater.* (2001).

18. Tanaka, H. *et al.* Design of the intelligent catalyst for Japan ULEV standard. *Top. Catal.* **30/31**, 389–396 (2004).

19. Screen, T. Platinum Group Metal Perovskite Catalysts. *Platin. Met. Rev.* **51**, 87–92 (2007).

20. Russell, A. & Epling, W. S. Diesel Oxidation Catalysts. *Catal. Rev.* **53**, 337–423 (2011).

21. Kröcher, O. *et al.* Investigation of the selective catalytic reduction of NO by NH3 on Fe-ZSM5 monolith catalysts. *Appl. Catal. B Environ.* **66**, 208–216 (2006).

22. Prasad, D. H. *et al.* Effect of nickel nano-particle sintering on methane reforming activity of Ni-CGO cermet anodes for internal steam reforming SOFCs. *Appl. Catal. B Environ.* **101**, 531–539 (2011).

23. Prasad, D. H. *et al.* Effect of steam content on nickel nano-particle sintering and methane reforming activity of Ni–CZO anode cermets for internal reforming SOFCs. *Appl. Catal. A Gen.* **411**–**412**, 160–169 (2012).

24. Deng, J., Cai, M., Sun, W., Liao, X. & Chu, W. Oxidative Methane Reforming with an Intelligent Catalyst: Sintering-Tolerant Supported Nickel Nanoparticles. (2013).

25. Nishihata, Y. *et al.* Self-regeneration of a Pd-perovskite catalyst for automotive emissions control. *Nature* **418**, 164–167 (2002).

26. Tanaka, H. *et al.* An intelligent catalyst. -*SOCIETY Automot. Eng. JAPAN* (2001).

27. Kajita, N., Uenishi, M., Tan, I., Tanaka, H. & Kimura, M. Regeneration of Precious Metals in Various Designed Intelligent Perovskite Catalysts. (2002).

28. Sato, N., Tanaka, H., Tan, I., Uenishi, M. & Kajita, N. Design of a practical Intelligent catalyst. *SAE Trans.* (2003).

29. Nishihata, Y., Mizuki, J., Tanaka, H., Uenishi, M. & Kimura, M. Self-regeneration of palladium-perovskite catalysts in modern automobiles. in *Journal of Physics and Chemistry of Solids* (2005). doi:10.1016/j.jpcs.2004.06.090

30. Tanaka, H. An intelligent catalyst: the self-regenerative palladium–perovskite catalyst for automotive emissions control. *Catal. Surv. from Asia* (2005).

31. Uenishi, M., Tanaka, H., Taniguchi, M., Tan, I. & Sakamoto, Y. The reducing capability of palladium segregated from perovskite-type LaFePdO x automotive catalysts. *Appl. Catal. A* (2005).

32. Nishihata, Y., Mizuki, J., Tanaka, H. & Uenishi, M. Self-regeneration of palladium-perovskite catalysts in modern automobiles. *J. Phys.* (2005).

33. Tanaka, H., Tan, I., Uenishi, M., Taniguchi, M. & Nishihata, Y. The Intelligent Catalyst: Pd-Perovskite Having the Self-Regenerative Function in a Wide Temperature Range. *Key Eng. Mater.* (2006).

34. Taniguchi, M. *et al.* The self-regenerative Pd-, Rh-, and Pt-perovskite catalysts. in *Topics in Catalysis* (2007). doi:10.1007/s11244-007-0207-x

35. Taniguchi, M., Uenishi, M., Tan, I., Tanaka, H. & Kimura, M. Thermal Properties of the Intelligent Catalyst. (2004).

36. Tanaka, H. *et al.* Self-Regenerating Rh- and Pt-Based Perovskite Catalysts for Automotive-Emissions Control. *Angew. Chemie Int. Ed.* **45**, 5998–6002 (2006).

37. Hamada, I., Uozumi, A., Morikawa, Y., Yanase, A. & Katayama-Yoshida, H. A density functional theory study of self-regenerating catalysts LaFe1-xMxO3-y(M = Pd, Rh, Pt). *J. Am. Chem. Soc.* **133**, 18506–18509 (2011).

38. Tanaka, H. & Kaneko, K. Method for producing perovskite-type composite oxide. *US Pat. 7,381,394* (2008).

39. Katz, M. B. *et al.* Reversible precipitation/dissolution of precious-metal clusters in perovskite-based catalyst materials: Bulk versus surface re-dispersion. *J. Catal.* **293**, 145–148 (2012).

40. Malamis, S. A. *et al.* Comparison of precious metal doped and impregnated perovskite oxides for TWC application. *Catal. Today* **258**, 535–542 (2015).

41. Katz, M. Advanced Transmission Electron Microscopy Studies of Induced Interactions of Metallic Species with Perovskite Oxide Hosts. (2013).

42. Jarrige, I. *et al.* Toward optimizing the performance of self-regenerating Pt-based perovskite catalysts. *ACS Catal.* **5**, 1112–1118 (2015).

43. Hazen, R. M. Perovskites. *Scientific American* **258**, 74–81 (1988).

44. Keav, S., Matam, S., Ferri, D. & Weidenkaff, A. Structured Perovskite-Based Catalysts and Their Application as Three-Way Catalytic Converters—A Review. *Catalysts* **4**, 226–255 (2014).

45. Tejuca, L. G., Fierro, J. L. G. & Tascón, J. M. D. Structure and Reactivity of Perovskite-Type Oxides. *Adv. Catal.* **36**, 237–328 (1989).

46. Neagu, D. Materials and Microstructures for High Temperature Electrochemical Devices through Control of Perovskite Defect Chemistry Dragos Neagu. 1–257 (2012).

47. Goldschmidt, V. M. Die gesetze der krystallochemie. (1926).

48. Peña, M. A. & and J. L. G. Fierro*. Chemical Structures and Performance of Perovskite Oxides. *Chem. Rev.* **101**, 1981–2018 (2001).

49. Chynoweth, A. G. {\it Ferroelectricity in crystals} by H. D. Megaw. *Acta Crystallogr.* **11**, 754–755 (1958).

50. Allan, N. L., Dayer, M. J., Kulp, D. T. & Mackrodt, W. C. Atomistic lattice simulations of the ternary fluorides AMF3(A = Li, Na, K, Rb, Cs; M = Mg, Ca, Sr, Ba). *J. Mater. Chem.* **1**, 1035–1039 (1991).

51. Neagu, D. & Irvine, J. T. S. *Perovskite Defect Chemistry as Exemplified by Strontium Titanate*. *Comprehensive Inorganic Chemistry II* (Elsevier Ltd., 2013). doi:10.1016/B978-0-08-097774-4.00421-6

52. Duprez, D. *et al.* Perovskites as Substitutes of Noble Metals for Heterogeneous Catalysis : Dream or Reality Se b. *Chem. Rev.* **114**, 10292 (2014).

53. Shannon, R. D. Revised effective ionic radii and systematic studies of interatomic distances in halides and chalcogenides. *Acta Crystallogr. Sect. A* **32**, 751–767 (1976).

54. Neagu, D., Tsekouras, G., Miller, D. & Ménard, H. In situ growth of nanoparticles through control of non-stoichiometry. *Nat. Chem.* (2013).

55. Neagu, D. & Irvine, J. T. S. Enhancing electronic conductivity in strontium titanates through correlated A and B-site doping. *Chem. Mater.* **23**, 1607–1617 (2011).

56. Oh, T., Rahani, E., Neagu, D. & Irvine, J. Evidence and Model for Strain-Driven Release of Metal Nanocatalysts from Perovskites during Exsolution. *J.* (2015).

57. Zhu, Y. *et al.* Promotion of oxygen reduction by exsolved silver nanoparticles on a perovskite scaffold for low-temperature solid oxide fuel cells. *Nano Lett.* (2015).

58. Liu, S., Chuang, K. & Luo, J. Double layered perovskite anode with in-situ exsolution of Co-Fe alloy to cogenerate ethylene and electricity in proton conducting ethane fuel cell. *ACS Catal.* (2015).

59. Tsvetkov, D., Ivanov, I. & Malyshkin, D. Oxygen content, cobalt oxide exsolution and defect structure of the double perovskite PrBaCo 2 O 6− δ. *J. Mater.* (2016).

60. Thalinger, R., Gocyla, M. & Heggen, M. Ni–perovskite interaction and its structural and catalytic consequences in methane steam reforming and methanation reactions. *J.* (2016).

61. Miller, E. Synthesis, Characterization, and Optimization of Novel Solid Oxide Fuel Cell Anodes. (2015).

62. Liu, S., Chuang, K. & Luo, J. Erratum to “Double Layered Perovskite Anode with in Situ Exsolution of Co–Fe Alloy To Cogenerate Ethylene and Electricity in Proton-Conducting Ethane Fuel Cell”. *ACS Catal.* (2016).

63. Armor, J. N. A history of industrial catalysis. *Catal. Today* **163**, 3–9 (2011).

64. Voorhoeve, R. J. H., Remeika, J. P. & Johnson, D. W. Rare-Earth Manganites: Catalysts with Low Ammonia Yield in the Reduction of Nitrogen Oxides. *Science (80-.).* **180**, 62–64 (1973).

65. Gallagher, P. K., Johnson, D. W. & Schrey, F. Studies of some supported perovskite oxidation catalysts. *Mater. Res. Bull.* **9**, 1345–1352 (1974).

66. Bravo-Suárez, J. J., Chaudhari, R. V & Subramaniam, B. Design of Heterogeneous Catalysts for Fuels and Chemicals Processing: An Overview. in *Novel Materials for Catalysis and Fuels Processing* 3–68 doi:10.1021/bk-2013-1132.ch001

67. Misono, M. Catalysis of Perovskite and Related Mixed Oxides. *Stud. Surf. Sci. Catal.* **176**, 67–95 (2013).

68. Neagu, D., Oh, T., Miller, D., Ménard, H. & Bukhari, S. Nano-socketed nickel particles with enhanced coking resistance grown in situ by redox exsolution. *Nat. Commun.* (2015).

69. Xu, S. *et al.* Perovskite chromates cathode with resolved and anchored nickel nano-particles for direct high-temperature steam electrolysis. *J. Power Sources* (2014).

70. Tsekouras, G., Neagu, D. & Irvine, J. Step-change in high temperature steam electrolysis performance of perovskite oxide cathodes with exsolution of B-site dopants. *Energy Environ. Sci.* (2013).

71. Li, Y., Wang, Y., Doherty, W., Xie, K. & Wu, Y. Perovskite chromates cathode with exsolved iron nanoparticles for direct high-temperature steam electrolysis. (2013).

72. Sun, Y., Li, J., Zeng, Y., Amirkhiz, B. & Wang, M. A-site deficient perovskite: the parent for in situ exsolution of highly active, regenerable nano-particles as SOFC anodes. *J. Mater.* (2015).

73. Prabha, I. Current Status of Platinum Based Nanoparticles : Physicochemical Properties and Selected Applications – A Review. 122–133 (2019).

74. Da, Y. *et al.* Catalytic oxidation of diesel soot particulates over Pt substituted LaMn 1-x Pt x O 3 perovskite oxides. *Catal. Today* **327**, 73–80 (2019).

75. Li, X. *et al.* In situ exsolution of PdO nanoparticles from non-stoichiometric LaFePd0.05O3+Δ electrode for impedancemetric NO2 sensor. *Sensors Actuators, B Chem.* **298**, (2019).

76. Gao, Y. *et al.* Energetics of Nanoparticle Exsolution from Perovskite Oxides. *J. Phys. Chem. Lett.* **9**, 3772–3778 (2018).

77. Fang, C. *et al.* Highly Dispersed Pt Species with Excellent Stability and Catalytic Performance by Reducing a Perovskite-Type Oxide Precursor for CO Oxidation. *Trans. Tianjin Univ.* **24**, 547–554 (2018).

78. Fierro, J. L. G. Chemical Structures and Performance of Perovskite Oxides. (2017).

79. Zhang, S. In-situ and Ex-situ Microscopy and Spectroscopy Study of Catalytic Materials by. 217 (2017).

80. Glazer, A. M. The classification of tilted octahedra in perovskites. *Acta Crystallogr. Sect. B* **28**, 3384–3392 (1972).

81. Howard, C. J. & Stokes, H. T. Group-Theoretical Analysis of Octahedral Tilting in Perovskites. *Acta Crystallogr. Sect. B* **54**, 782–789 (1998).

82. Neagu, D., Tsekouras, G., Miller, D. D. N., Ménard, H. & Irvine, J. T. S. In situ growth of nanoparticles through control of non-stoichiometry. *Nat. Chem.* **5**, 916–923 (2013).

83. G. ROUSSEAU. No Title. *Acad. Sci. Paris* **109**, 144 (1889).

84. Statton, W. O. The phase diagram of the BaO-TiO2system. *J. Chem. Phys.* **19**, 33–40 (1951).

85. Randall, J. J. & Ward, R. The Preparation of Some Ternary Oxides of the Platinum Metals. *J. Am. Chem. Soc.* **81**, 2629–2631 (1959).

86. Haradem, P. S., Chamberland, B. L., Katz, L. & Gleizes, A. A structural model for barium platinum oxide, Ba3Pt2O7. *J. Solid State Chem.* **21**, 217–223 (1977).

87. Chaston, J. C. Reactions of Oxygen with the Platinum Metals; II-OXIDATION OF

RUTHENIUM, RHODIUM, IRIDIUM AND OSMIUM. *Platin. Met. Rev.* **9**, 51–56 (1965).

88. Sharma, P. A., Brown-Shaklee, H. J. & Ihlefeld, J. F. Oxygen partial pressure dependence of thermoelectric power factor in polycrystalline n-type SrTiO3: Consequences for long term stability in thermoelectric oxides. *Appl. Phys. Lett.* **110**, (2017).

89. Kuklja, M. M., Mastrikov, Y. A., Jansang, B. & Kotomin, E. A. The intrinsic defects, disordering, and structural stability of Ba xSr 1-xCo yFe 1-yO 3-δ perovskite solid solutions. *J. Phys. Chem. C* **116**, 18605–18611 (2012).

90. Nur, A. S. M. *et al.* Phase-Dependent Formation of Coherent Interface Structure between PtO2 and TiO2 and Its Impact on Thermal Decomposition Behavior. *J. Phys. Chem. C* **122**, 662–669 (2018).

12. Nur, A. S. M., Funada, E., Kiritoshi, S., Matsumoto, A., Kakei, R., Hinokuma, S., Yoshida, H., Machida, M. Phase-Dependent Formation of Coherent Interface Structure between PtO2 and TiO2 and Its Impact on Thermal Decomposition Behavior. *J. Phys. Chem. C* **122**, 662–669 (2018).

13. Haradem, P. S., Chamberland, B. L., Katz, L., Gleizes, A. A structural model for barium platinum oxide, Ba3Pt2O7. *J. Solid State Chem.* **21**, 217–223 (1977).

CHAPTER 4 MICROSTRUCTURE

4.1 Microstructure: sintering, reduction, porosity and oxidation chemistry

The means of reduction sintering and oxidation are primary factors in forming a complex nano-decorated perovskite surface. Firstly. in this chapter we will explore the reduction conditions necessary in forming nano-decorated Pt particles, and secondly, we will examine the sintering mechanism and nanostructure of the bulk and cleaved surfaces. Lastly, we will examine the oxidation chemistry of the nano-decorated particles formed from reduction.

Reduction

Meta-stable phase transformation, Chemical precursors, purity, processing and surface impurities

In reduction conditions (reductive gas and temperature), oxygen is removed form the bulk and surface of the perovskite structure from thermal vibration. The change in mass can be used to calculate the amount of oxygen lost through reduction, and therefore, using the amount of oxygen lost, we can quantify the extent of reduction through TGA measurements (thermogravimetric analysis)[1]. Every oxygen atom lost results in two electrons and an oxygen vacancy:

$$O_O^x \rightarrow \frac{1}{2}O_2 + V_O^{\cdot\cdot} + 2e'$$

$$\frac{m_{ABO_3}}{u_{ABO_3}} = \frac{m_{ABO_{3-\partial}}}{u_{ABO_{3-\partial}}}$$

U_{ABO3} is the molar weight of the perovskite, m_{ABO3} is the mass of the perovskite, and A_0 is the atomic weight of oxygen.

$$\frac{m_{ABO_3}}{u_{ABO_3}} = \frac{m_{ABO_{3-\delta}}}{u_{ABO_{3-\delta}} - \delta \cdot A_0}$$

Therefore:

$$\frac{m_{ABO_3}}{m_{ABO_3}} = \frac{u_{ABO_{3-\delta}}}{u_{ABO_{3-\delta}} - \delta \cdot A_0}$$

Using fraction properties:

$$\frac{m_{ABO_3}}{m_{ABO_{3-\delta}} - m_{ABO_3}} = \frac{u_{ABO_3}}{u_{ABO_3} - \delta \cdot A_0}$$

Reduction can therefore be quantified by:

$$\delta = \frac{u_{ABO_3}}{A_O} \cdot \frac{m_{ABO_3} - m_{ABO_{3-\delta}}}{m_{ABO_3}}$$

Reduction overview

A-site deficient perovskite systems were all reduced in a tube furnace with a 20ml/min flow rate of 5%H_2/Ar. Reduced pellets were placed in a ceramic boat and laid sideways rather than flat so as to maximise the flow of gas over the surface of the pellet. A variety of reduction conditions were studied in order to determine metal exsolution and corresponding size of metallic nanoparticles (Pt and Pd) for specific catalytic reactions, including CO-oxidation and NH_3 slip conversion. It was also possible to calculate the oxygen loss and therefore assume the correct amount of Pt that emerged from the surface of the perovskite itself. A comparison of Pt from non-barium platinate and barium platinate containing samples also revealed differences in nanoparticle anchoring and mechanistic embedding of Pt to the perovskite surface. In combination with studying SEM and TEM images, it was possible to further calculate dispersion, particle size and composition. A strong difference in Sr and Ca cations on the A site also contributed to different morphological effects, as seen by SEM.

Porosity

Nitrogen physisorption of Pt@LST prepared by solid-state synthesis and combustion synthesis was undertaken in order to understand the porosity of each material in the powder form, as can be seen in Figure 18. Pt@LST prepared by solid-state synthesis showed no meso- or micro-porosity, and the material itself is very dense and has a low BET surface area of $3.83 m^2/g$. A type I reversible isotherm is observed, indicating that very low microporosity on the surface of the material is available for nitrogen adsorption. LBSPT prepared by combustion synthesis was porous and had a much higher BET surface area of $22.08 m^2/g$, and the surface area of reduced LBSPT prepared by sol gel was slightly lower $18.789 m^2/g$. This is due to the effect of reduction conditions contributing to further sintering of the material. Sol gel synthesis of LBSPT (not single phase) created a disordered nanoporous material with no adsorption limit at high p/p_o indicating slit- and plate-like nanopores, show by the H3 hysteresis loop. The porosity of sol-gel prepared samples can be further confirmed from SEM micrographs, as shown in Figure 4-0. Clear disordered micropores (1) and plate-like structures (2) are visible, as well as a fully formed hexagonal platinum nanoshield (4).

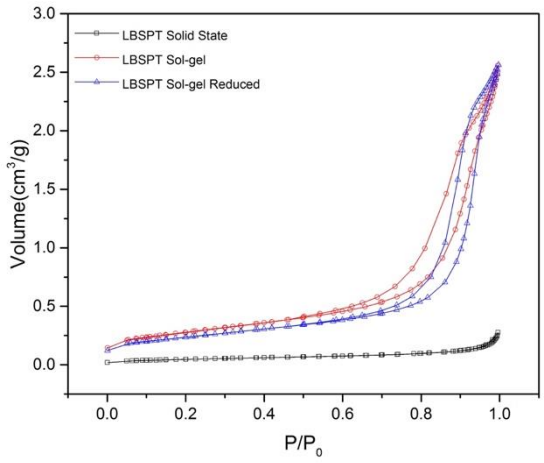

Perovskite $La_{0.4}Ba_{0.09}Sr_{0.31}Pt_{0.06}Ti_{0.94}O_3$ (LBST)	S_{BET} (m^2/g)	S_{ext} (m^2/g)	S_{mp} (m^2/g)	Pore $size_{BJH}$ (nm)
Pt@LST solid state	3.83	3.16	-	9.4
LBST sol-gel (not single phase)	22.08	13.30	8.79	20.4
LBST sol-gel reduced	18.79	11.01	7.78	17.1

Figure 4-0a: Nitrogen Physisorption of LBSPT prepared by both synthesis routes.

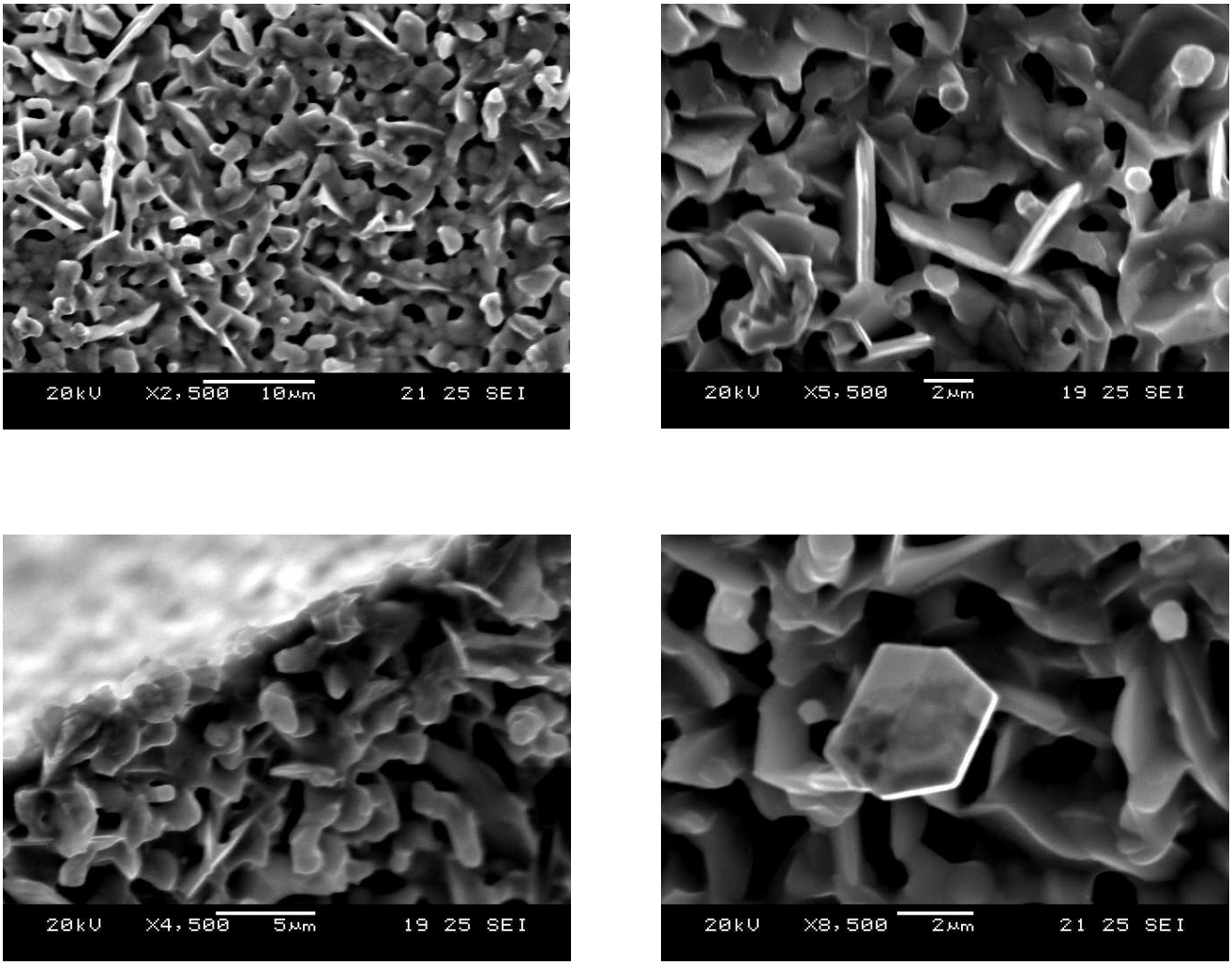

Figure 4-0b: SEM micrographs of LBSPT prepared by Sol-gel synthesis (not single phase), calcined at 1200°C and reduced in 5%H_2/Ar at 900°C for 2 hours.

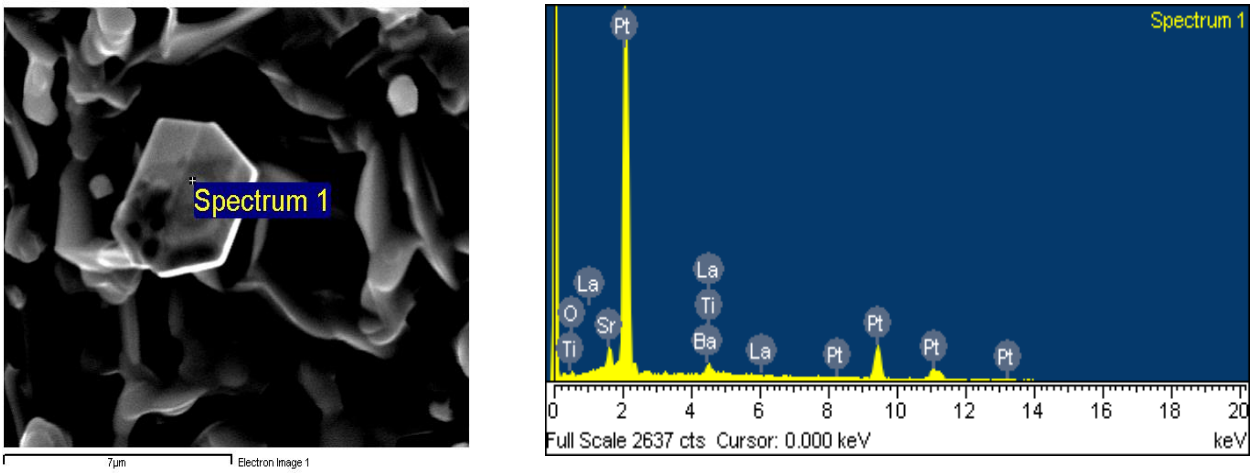

Figure 4-0c: EDS point data for reduced LBSPT prepared by Sol-gel synthesis. Spectrum 1 shows the composition of the point.

Scanning electron microscopy coupled with energy dispersive spectroscopy (EDS) was used as a characterization tool for analysing the microstructure of LBSPT and understanding the porosity. Due to both calcination and sintering conditions, interesting nanostructures were observed in reduced LBSPT prepared by combustion synthesis. Figure 19 shows the micrographs of a porous pellet that was calcined at 1000°C for 12 hours and reduced at 900°C for 2 hours. The EDS point data are shown in Figure 4-0.

Reduction of $La_{0.2}Ba_ySr_{0.7-y}TiO_3$

$La_{0.2}Ba_ySr_{0.7-y}TiO_3$ was initially studied after reduction from 800-1000°C in 100°C steps for 12 hours in order to study the effect of reduction on the microstructure. The chosen stoichiometry of x=0.4, as shown in Figure 4-1, was exemplified, as it showed the highest extent of reduction which further results in more metallic exsolution. The extent of reduction from the change in the dopant amount of Ba is shown in Figure 4-2, and the extent of reduction shows a stable reduction up to 1000°C, indicating the amount of Ba on the A site has little effect on the overall reduction of the perovskite. Furthermore, evidence can be seen by observing the microstructure of the material via SEM micrograph analysis, as seen in Figure 4-3. Above 900°C titanate grains often develop, as seen in Figure 4-3d. The extent of reduction is noted as O-δ.

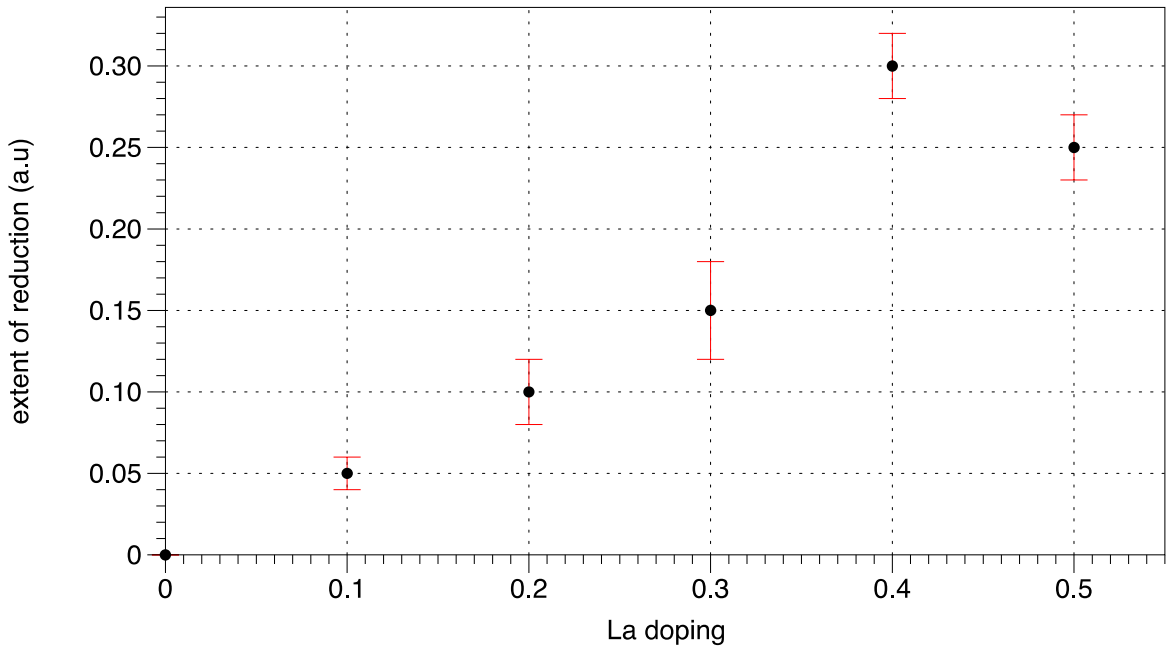

Figure 4-1 shows the extent of reduction vs A site stoichiometry for $La_xBa_ySr_{0.7-y}TiO_3$ in 5% H_2Ar at 1000°C for 12 hours. Y axis =La_x x=0-0.5)

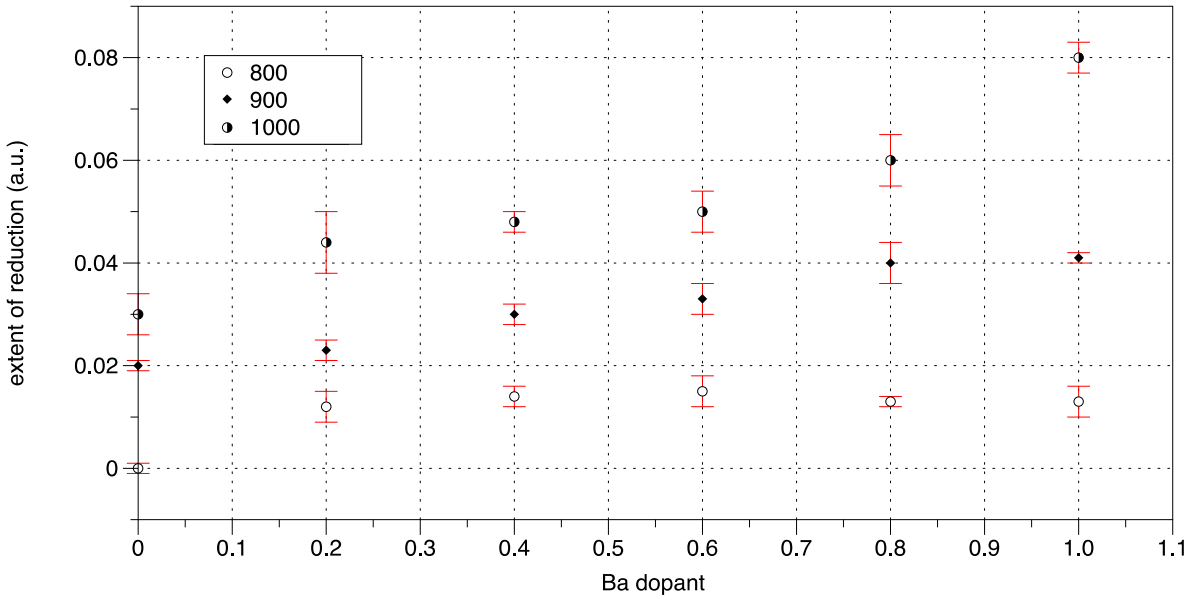

Figure 4-2 shows the extent of reduction for 800,900 and 1000°C for 12hr in 5%H_2Ar of $La_{0.2}Ba_ySr_{0.7-y}TiO_3$ (y axis = $Sr_{0.7-y}$, y= 0-1.1) calculated through TGA analysis.

Figure 4-3

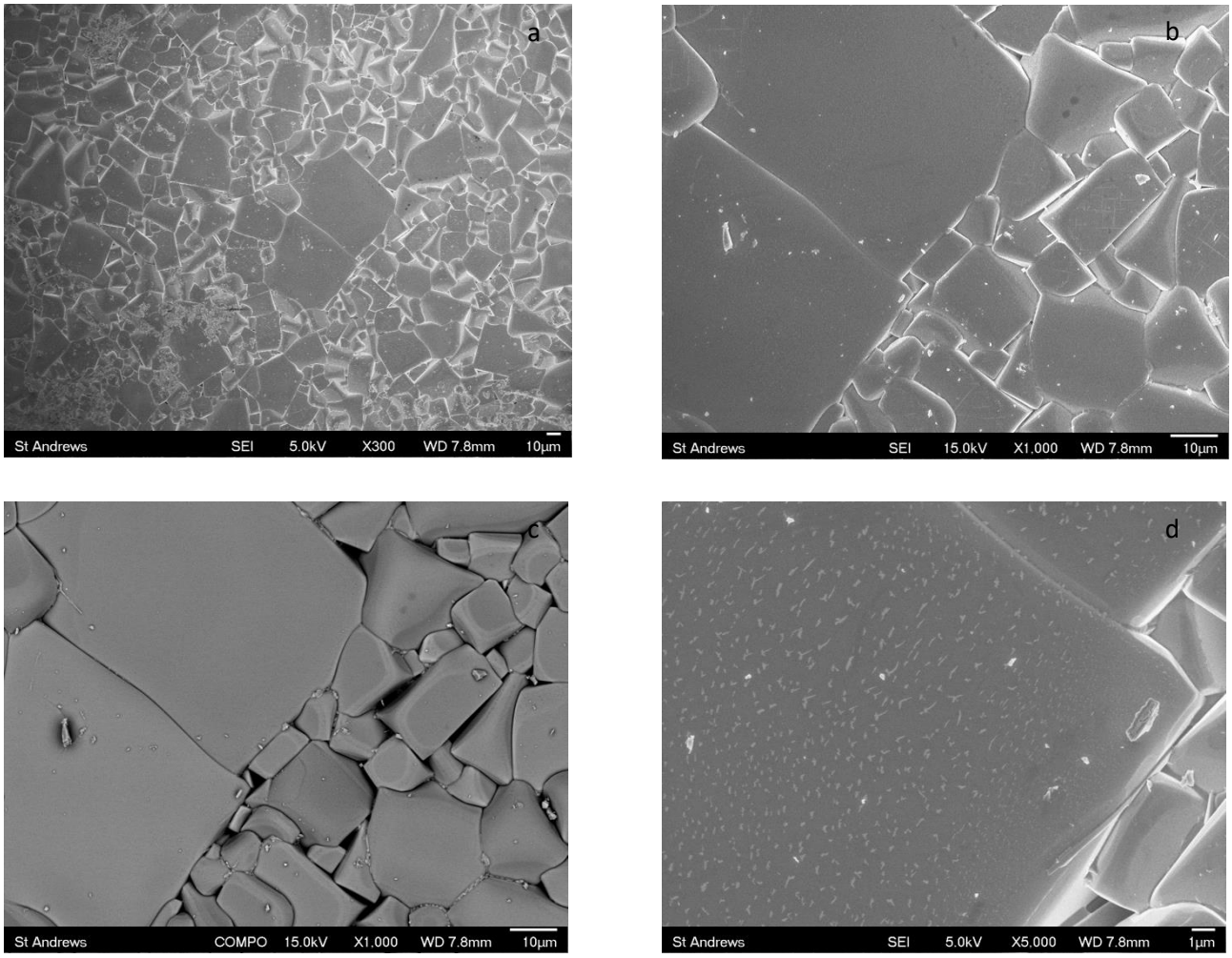

Figure 4-3: FEG-SEM micrograph of $La_{0.2}Ba_{0.6}Sr_{0.64}TiO_3$ pellet, sintered for 12 hours at 1450°C and further reduced in 5%H_2Ar for 12hr at 1000°C. Field Emission Gun Scanning Electron Microscopy (FEG-SEM)

Micrographs in Figure 4-3 reveal the microstructure of the formed LBST perovskite after the sintering step. Micrograph (a) shows a dense pellet has formed with both hexagonal and cubic grain growth, there is no observable porosity, as a result of the high firing temperature and 12-hour duration. Micrograph (b) further shows the grain boundary between two distinct sized grains, which is attributed to the kinetics and thermodynamic effects of the sintering process. Grain boundary migration of larger bi-modal phases resulting in coalescence could contribute to this effect; however, this does not conform with PXRD data, which suggests the material is single phase. Micrograph (c) has been taken in backscattering mode (COMPO); there is no evident secondary phase in the back scattering mode further confirming the single phase PXRD pattern. The two distinct morphological sized grain boundaries are evident, the ball milling of the precursor powders determines the particle size of the pelleted powder. Micrograph d shows an interesting linear scarring (possible Titanate exsoluition) on the surface of the pellet, this is attributed to the evolution of carbonates from the pellet during the sintering process as well as the quenching of the pellet. The overall goal of synthesizing LBST and understanding the unit cell size was achieved, paving the way to study $La_xBa_ySr_{(1-3x/2)-y}Pt_zTi_{1-z}O_{3-\delta}$.

Reduction of $La_xBa_ySr_{(1-3x/2)-y}Pt_zTi_{1-z}O_{3-\delta}$ without Trojan Horse $Ba_3Pt_2O_7$

The reduction of $La_xBa_ySr_{(1-3x/2)-y}Pt_zTi_{1-z}O_{3-\delta}$ proved interesting enough to study despite the Pt peak being observable in XRD patters (Figure 3-10) and the formation of Pt nanoparticles in air (Figure 4-4). It was found that platinum (z=0.01-0.3) (initially incorporated into the perovskite through solid-state synthesis as PtO_2) dissociated from the ceramic bulk at temperatures above 900°C in air even if the perovskite phase had yet to fully form (above 1100°C). The stability of the base perovskite structure formed a dense ceramic structure with terracing, porosity surrounded by grains as seen in Figure 4-4a. The pores were surrounded by a dihedral structure of a 120° angle, thus forming a flat interface rather than a concave interface at before reduction temperature <12 hours; however, for reduction conditions over 20 hours, concave smaller pores were observed. This indicates the shrinking of the pore size and the densification of the bulk perovskite[2]. Notably, both pre- and post-reduction showed nodular formation around large micron-sized Pt particles, indicating a strong affinity for the ceramic bulk toward the metal. The cleaved bulk of the material revealed Pt nanoparticles that have primarily formed at the neck or what once was the neck of a pore. Gas-phase reactants tend to condense at neck regions of pores due to to the surface nature curvature and higher contact points.

4-4a

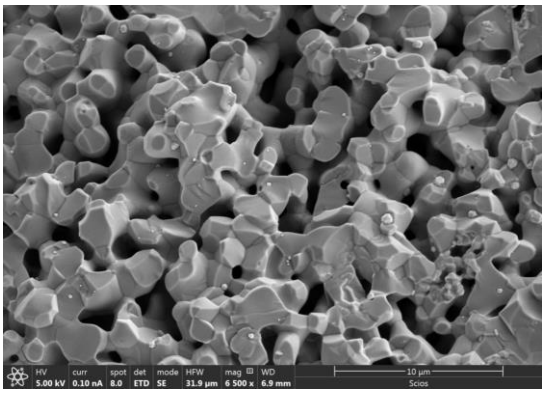

4-4b

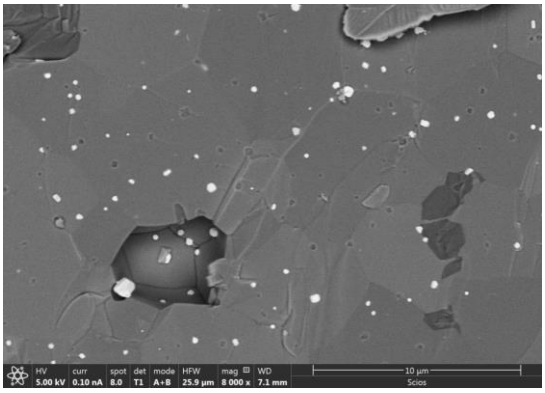

4-4c

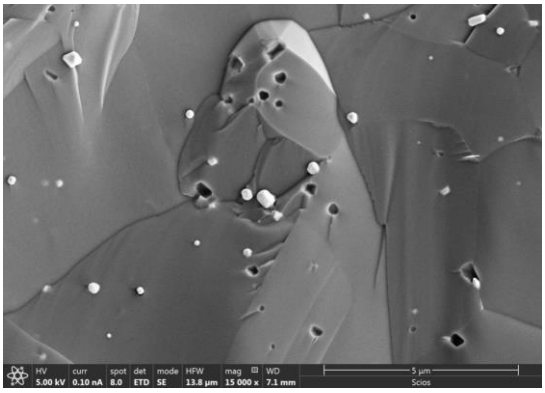

4-4d

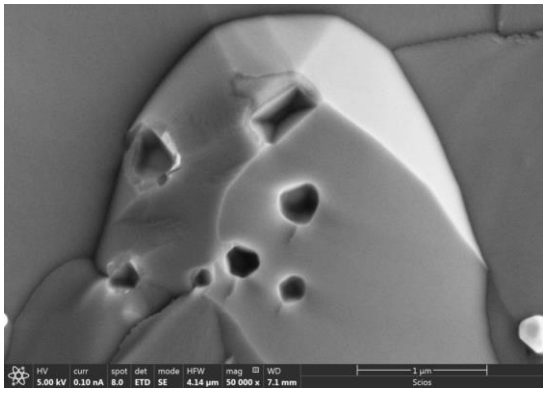

Figure 4-4a: A cleaved pellet shows the microstructure of $La_{0.4}Ba_{0.016}Sr_{0.384}Pt_{0.01}Ti_{0.99}O_3$ sintered in air at 1300°C. A dense perovskite phase has formed, and clear necking of the pores has started to occur. The dihedral angle is less than 120° and therefore has allowed a grain to form. Large agglomerations of Pt are visible, which have formed dihedral diamond formations as a result of the high temperature of synthesis. Pt here has not been incorporated into the crystal structure of the perovskite, as is evident. Figure 4-4b: $La_{0.4}Ba_{0.016}Sr_{0.384}Pt_{0.01}Ti_{0.99}O_3$ show a cleaved pellet after reduction in 5%H_2Ar for 12 hours at 700°C. Large agglomerations of Pt have formed in pits within the bulk of the crystalline structure. Figure 4-4c further exemplifies the pitting of Pt agglomerates formed due to the incomplete synthesis of $La_{0.4}Ba_{0.016}Sr_{0.384}Pt_{0.01}Ti_{0.99}O_3$ after reduction. Figure 4-4d shows pitting caused by Pt agglomeration within the cleaved bulk of the perovskite $La_{0.4}Ba_{0.016}Sr_{0.384}Pt_{0.01}Ti_{0.99}O_3$. Interestingly, there are nodules that have formed around the pit, indicating strong anchoring of the particle.

4-4e

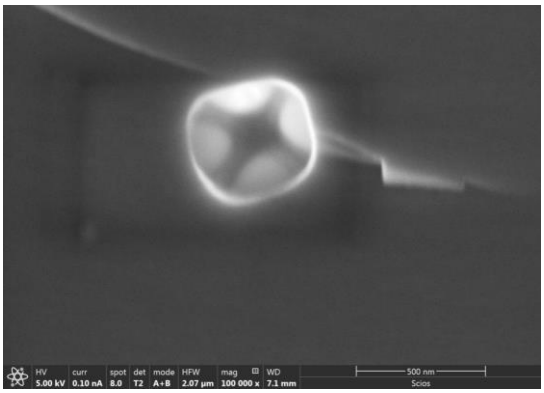

4-4f

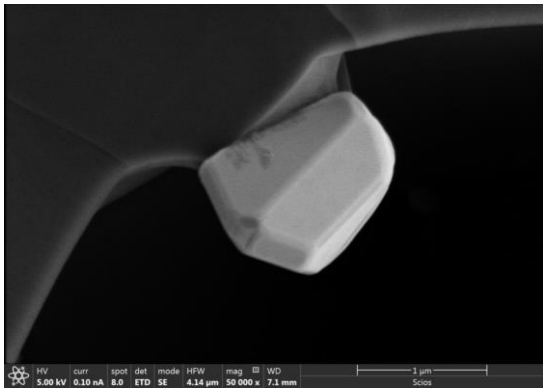

Figure 4-4e shows a pit 500nm in diameter with clear anchor nodule at 90° angles to one another.Figure 4-4f shows a large Pt particle 1um in size attached to the pore within the microstructure of $La_{0.4}Ba_{0.016}Sr_{0.384}Pt_{0.01}Ti_{0.99}O_3$

Element	Weight%	Atomic%	
O K	3.36	28.20	
Ti K	1.77	4.96	
Sr L	0.81	1.25	
Ba L	1.14	1.11	
La L	1.86	1.80	
Pt M	91.06	62.69	
Totals	100.00		

Figure 4-4g shows an EDS point analysis on the 1um sized particle in Figure 4-4e, confirming its elemental make up of Pt.

Formation of a crystalline single phase of of $La_xBa_y(Sr/Ca)_{(1-3x/2)-y}Pt_zTi_{1-z}O_{3-\delta}$ with Trojan Horse $Ba_3Pt_2O_7$ in air

As discussed previously in chapter 3, the use of PtO_2 was not deemed a suitable precursor for forming a phase-pure A-site deficient perovskite with Pt on the B site. $Ba_3Pt_2O_7$ was therefore used in order to incorporate Pt into the crystal structure. Sintering of the perovskite phase from 1100 to 1500°C in air for 12 hours revealed a Pt peak (Figure 3-12) and dissolution from the crystal structure despite the use of $Ba_3Pt_2O_7$. At 1100°C, the perovskite phase fully formed and at 1500°C, densification of the material and a slightly reductive atmosphere leads to Pt forming on the surface of the material rather than the bulk. The surface of a pellet is more energetically favourable than the bulk. The excess free energy of the surface can be estimated as the difference between the atomic contributions of bulk atoms and the missing atomic contribution at the surface (not considering anisotropy and restructuring)[3]. Therefore, the energetically favourable surface results in a stronger affinity of atomic Platinum migration rather than atomic migration within the bulk of the perovskite. As a result, even in air (slightly reducing above 1100°C) Pt nanoparticles formed on the surface of what is a crystalline perovksite. This cannot be considered embedment and/or exsolution, nor anchoring, and more of a deposition of metallic nanoparticles on the surface (not catalytically favourable). Interestingly, no large 1um sized Pt particles were found within the bulk or surface structure, unlike the synthesis with PtO_2. As only nanoparticles were found decorated on the surface, it can be assumed the $Ba_3Pt_2O_7$ has a strong affinity for the perovskite and the mechanistic effects of Pt dissociating from the precursor are different to that of PtO_2. It can be considered that a metastable crystalline phase had been achieved in sintering conditions in air rather than a stable crystalline phase, as seen in Figure 4-5. It is important to note that while higher temperature synthesis in air above 1200°C occurred, $Ba_3Pt_2O_3$ decomposition occurs at 1250-1300°C; thus, if the precursor had not fully incorporated then disoluted, platinum would be expected to remain within the bulk until 1300°C. The mechanism of this can be attributed to the energetically favourable pellet surface whereby Pt migrates toward the surface and propagates upon higher temperature to form an atomic scale[4] and further agglomeration to form sporadically shaped nanoparticles.

4-5a

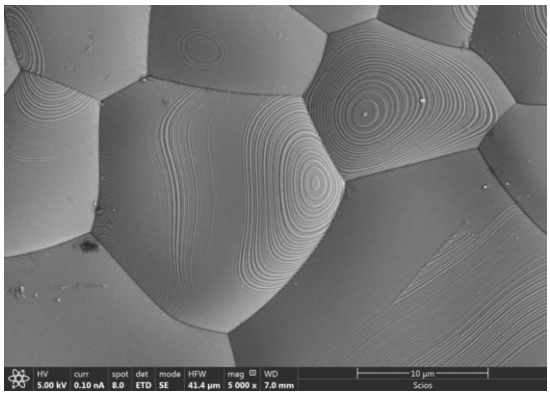

4-5b

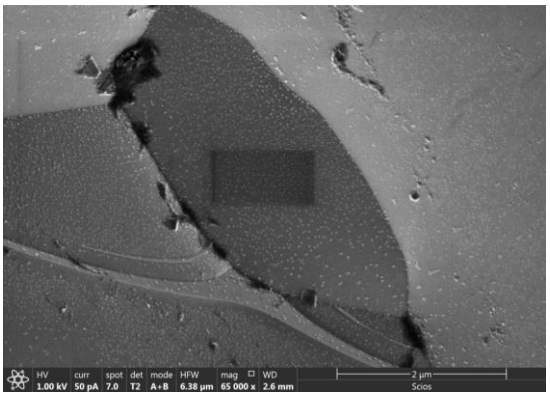

4-5c

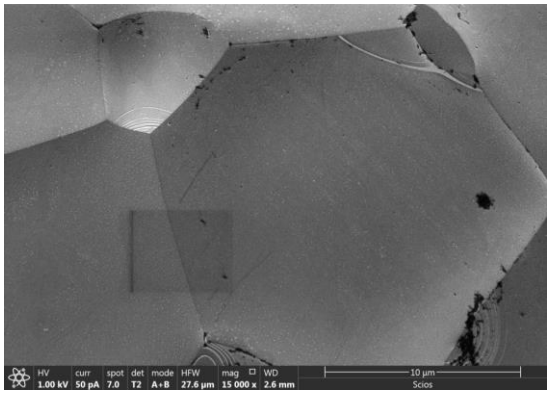

4-5d

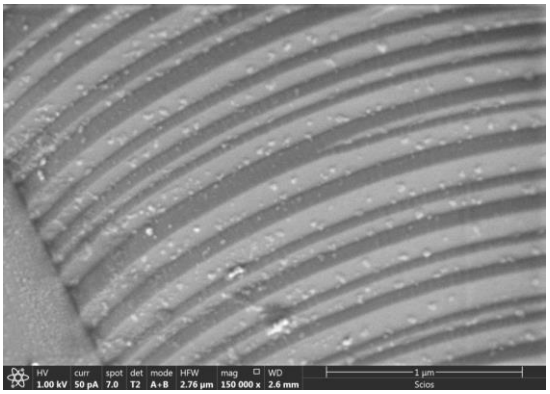

Figure 4-5a shows $\underline{La_xBa_y(Sr)_{(1-3x/2)-y}Pt_zTi_{1-z}O_{3-\delta}}$ crystalline perovskite surface structure of a pellet with 0.5wt% Pt doped with $Ba_3Pt_2O_7$, sintered in air at 1300°C. Figure 4-5b shows the crystalline surface of $\underline{La_xBa_y(Sr)_{(1-3x/2)-y}Pt_zTi_{1-z}O_{3-\delta}}$ crystalline perovskite surface structure of a pellet with 0.5wt% Pt doped with $Ba_3Pt_2O_7$ sintered in air at 1300°C with evident Pt nanoparticles decorating the surface. Upon close inspection, distinct lines of formation can be seen perpendicular to the neck of the grain. Some of the Pt nanoparticles are larger than others. Figure4-5c shows morphologically distinct Pt nanoparticles on the surface of crystalline perovskite $\underline{La_xBa_y(Sr)_{(1-3x/2)-y}Pt_zTi_{1-z}O_{3-\delta}}$ of a pellet with 0.5wt% Pt doped with $Ba_3Pt_2O_7$ sintered in air at 1200°C. Figure 4-5d shows morphologically distinct Pt nanoparticles on the surface of crystalline perovskite $\underline{La_xBa_y(Sr)_{(1-3x/2)-y}Pt_zTi_{1-z}O_{3-\delta}}$ of a pellet with 0.5wt% Pt doped with $Ba_3Pt_2O_7$ sintered in air at 1200°C. Clear distinct terracing can be seen typical of a A-site deficient perovskite that is cubic. The morphology of the Pt nanoparticles is not spherical, and they are widely different in shape, indicating no real mechanistic exsolution or anchoring on the surface of the perovskite itself.

Formation of $La_{0.4}(Ca/Sr)_{0.3925}Ba_{0.0075}Pt_{0.005}Ti_{0.995}O_3$ with Trojan Horse $Ba_3Pt_2O_7$ in oxygen Pt@L(C/S)T

The formation of a single-phase $La_{0.4}(Ca/Sr)_{0.3925}Ba_{0.0075}Pt_{0.005}Ti_{0.995}O_3$ in an oxygen-sintering environment at 1100-1200°C was confirmed through XRD (Figure 3-14). The microstructures – both surface and bulk –showed no nanoparticle decoration and were visibly clean (free of Pt) on all micrographs. This indicates that the surface energy of the pellet had remained low enough for Pt to remain within the crystalline structure of the perovskite itself, which was further confirmed by XAS, XANES and XPS surface measurements (discussed later in this chapter). The prevention of Pt from coalescing and forming nanoparticles prior to reduction was seen as the primary step to fully characterising this new material. The full incorporation of Pt into a perovskite crystal lattice with no Pt observable is a complete novelty.

The distinct morphologies of Pt@LCT (tetragonal I4/mcm) are different to that of Pt@LST (cubic Pm-3m) due to the cation size of Ca and Sr. Both Pt@LCT and Pt@LST were more porous than previously synthesised samples in air, primarily due to the lower sintering temperature of 1200°C and the effect of oxygen stoichiometry preservation at the surface of the perovskite. The bulk microstructure was consistent throughout with evident terracing formation on both cubic (Pt@LST) and tetragonal systems (Pt@LCT), which is common for A-site deficient stoichiometries. Furthermore, in comparison to $La_{0.4}Ca_{0.3925}Ba_{0.0075}TiO_3$ containing no Pt, the microstructure was the same in comparison (Figure 4-6a-c).

4-6a

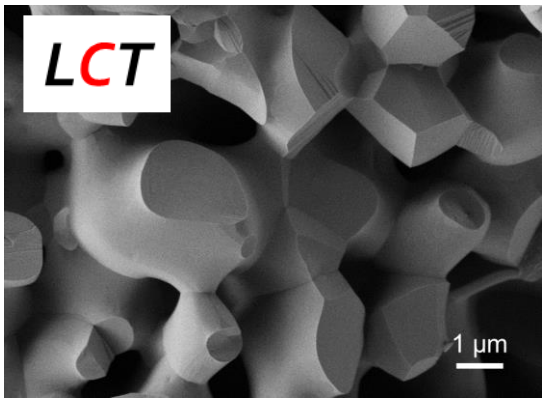

4-6b

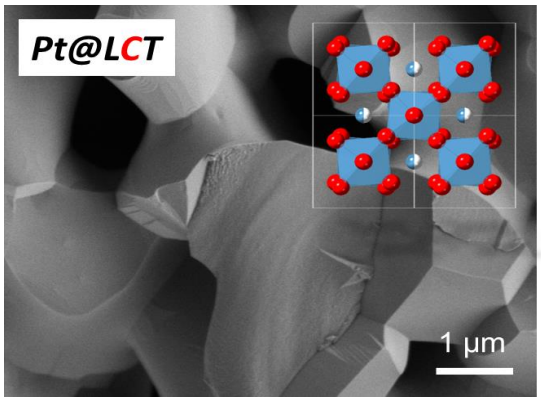

4-6c

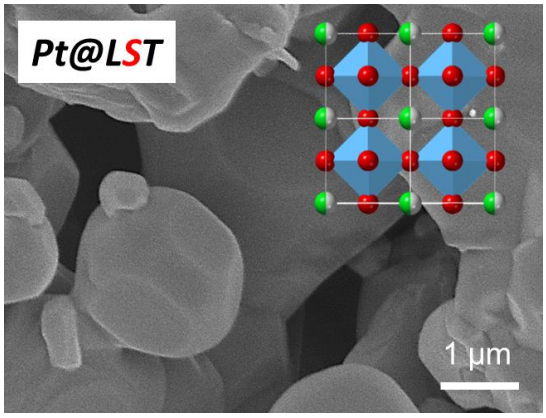

4-6d

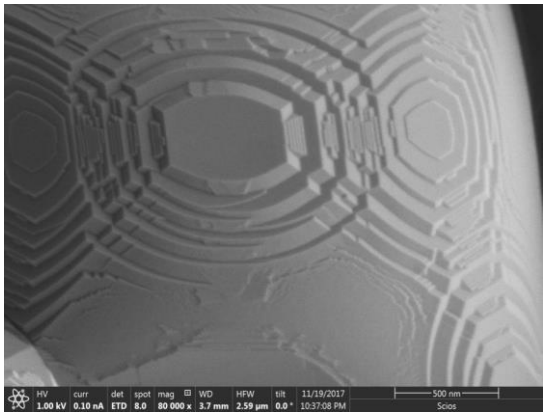

4-6e

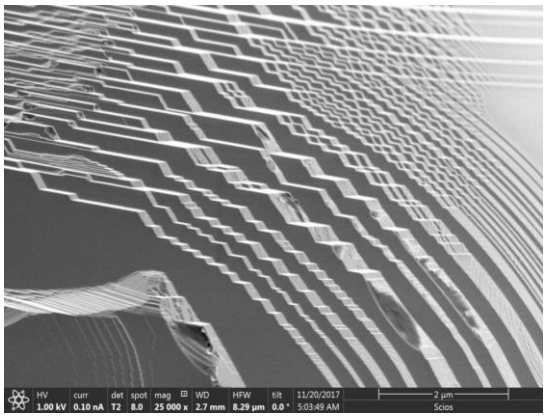

Figure 4-6a shows $La_{0.4}Ca_{0.3925}Ba_{0.0075}TiO_3$ cleaved and bulk surface. Figure 4-6b shows the native and cleaved surface Pt@LCT (tetragonal I4/mcm), showing visibly no embedded or exsolved nanoparticles. Moreover, the clean surface shown in the micrograph further confirms Pt as part of the crystalline structure in atomic form after high temperature sintering in pure O_2 for 12 hours at 1200°C in relation to the XRD in Figure 3-14.Figure 4-6c shows Pt@LST (cubic Pm-3m) after formation of the perovskite phase in the pure O_2 environment for 12 hours at 1200°C. A distinctly different microstructure is observable from Figure 4-6a. No Pt is visible in the micrograph, and this is further confirmed by the XRD in Figure 3-14. Figure 4-6e shows clear terracing structure of the Pt@LST perovskite sintered in O_2 or 12hr at 1200°C.

Reduction of $La_{0.4}(Ca/Sr)_{0.3925}Ba_{0.0075}Pt_{0.005}Ti_{0.995}O_3$ with Trojan Horse $Ba_3Pt_2O_7$ sintered in oxygen

Reduction of P@L(C/S)T revealed some fascinating morphologically distinct traits and has furthered our understanding of the emergence mechanism. In this study, nanoparticle (NP) dispersion, morphology, oxidation state, anchoring and temperature control were observed.

Pt nano emergence occurred under reduction conditions in 5%H_2Ar from 500-900°C after 12 hours for both P@L(C/S)T. The optimum conditions of Pt emergence were guided from TGA (Figure 4-7) (thermogravimetric analysis) in 5% H_2/Ar. An initial mass step occurred at 700°C with a total mass loss of 0.42 % on heating to 1000°C and holding for 12 hours (Fig. 4-7). Pt emergence occurred after 700°C, indicating that all Pt (0.5 wt%) has reduced, further weight loss can be attributed to titanite weight loss and the loss of O_2 from the perovskite. More O_2 is lost 0.067 atoms per formula unit than is needed to reduce Pt^{4+}, indicating full reduction and emergence of Pt. 700°C was therefore chosen as a primary reduction temperature, on the assumption that Pt emergence results mainly from the initial reduction step.

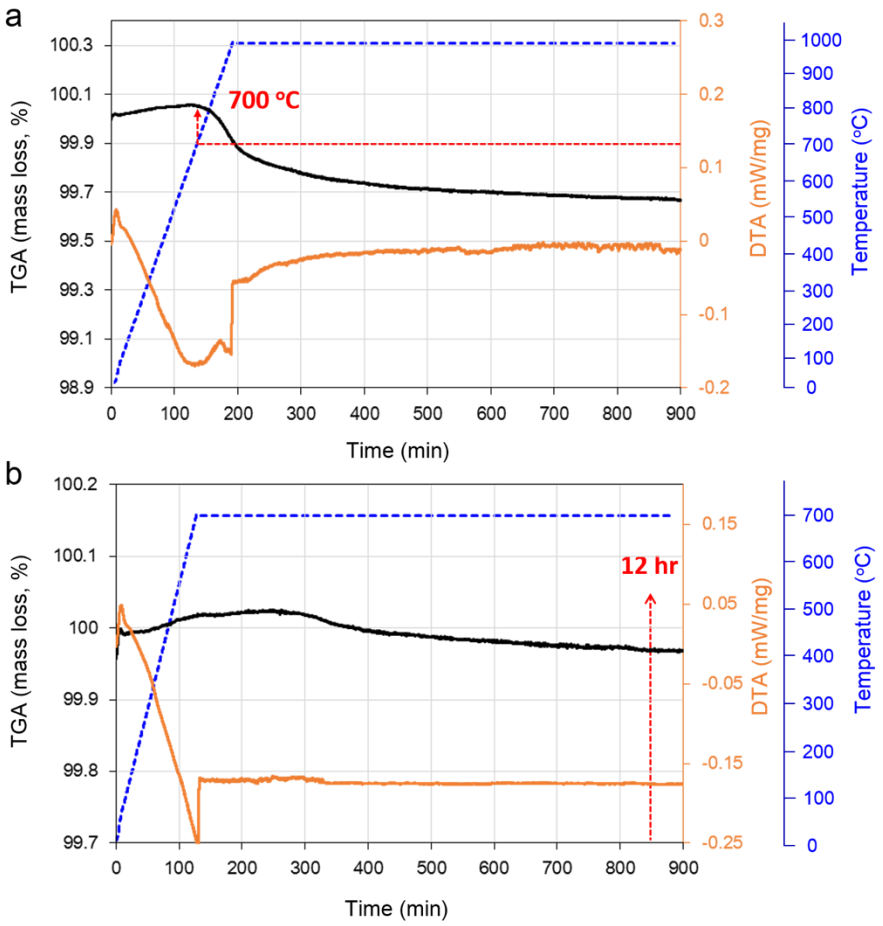

Figure 4-7: TGA and DTA analysis of Pt@LCT, by different measurement conditions: (a) heat up to 1000 °C with a ramp rate of 5 °C min^{-1}; and (b) heat up to 700 °C with a ramp rate of 5 °C min^{-1} and keep for 15 hrs, at the gas atmosphere of 5% H_2/95% Ar (20ml/min) to prove the assumed Pt emergence starting temperature and time from the weight loss behaviour. . The initial mass increase is due to free oxygen within the perovskite system initially oxidising and then reducing.

Applying these conditions, 12 hours at 700°C of reduction, the micrograph in Figure 4-8a shows well dispersed Pt NPs decorated on the surface by Pt emergence from A-site deficient Pt@L(C/S)T, denoted as Pt+L(C/S)T. Selected regions shown in Figure 4-8b display morphologically distinct Pt NPs with an average size of 15 nm (5-25 nm) and 20 nm (5-35 nm) for Pt+LCT and Pt+LST, respectively. Examination of Figure 4-8d for the HR-TEM (high-resolution transmission electron

microscopy) analysis of Pt+LCT reveals that the exposed NPs consist of Pt and have an embedded feature on the perovskite surface. From the XRD results in Figure 3-16, metal Pt peaks are observed for both perovskites without major change in their original perovskite structures, indicating the emergence of Pt from the crystal structure. Interestingly, a notable aspect is the difference in the Pt emergence tendency between Ca- and Sr-based perovskites. While the emergent Pt NPs from Pt+LST shows a bi-pyramidal localised dispersion, the Pt+LCT shows well dispersed spherical emergent Pt NPs across the surface.

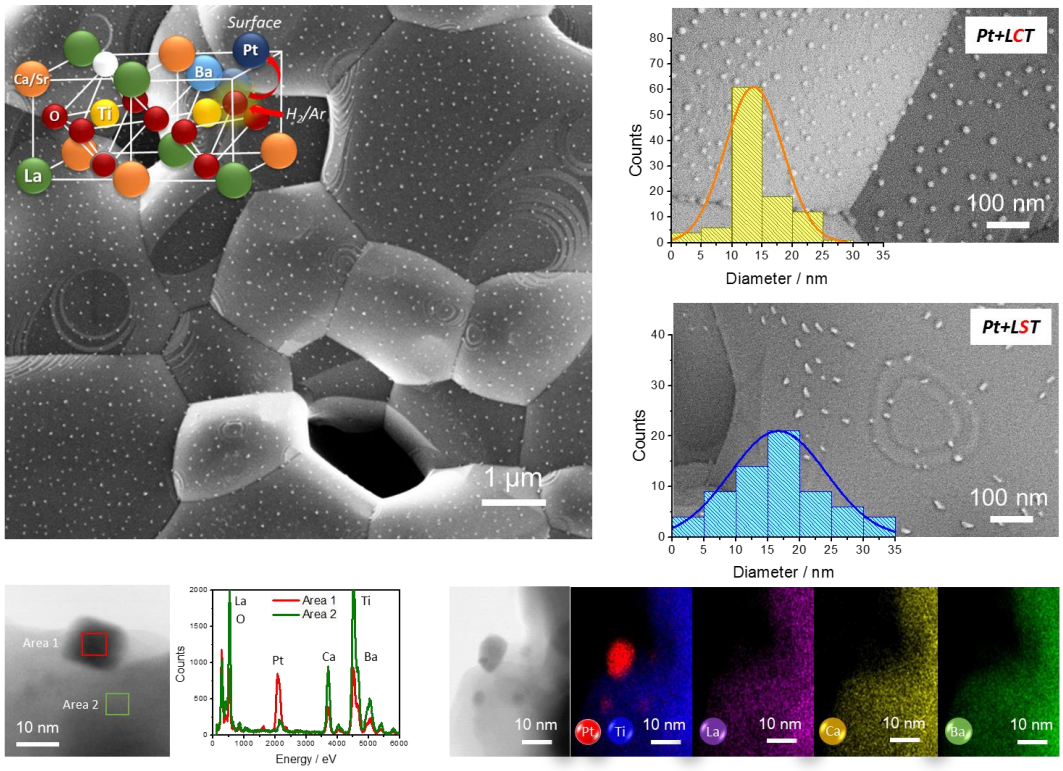

Figure 4-8 shows distinct Pt nanoparticle coverage on Pt+LCT and Pt+LST as well as confirmatory TEM-EDX for Pt nanoparticles.

The different morphological traits could be attributed to the Sr enrichment near the surface, as preciously observed for Ni-containing strontium titanates[5]. The greater dispersion at Pt+LCT is consistent with previous studies indicating more facile emergence for calcium titanate systems[6],

probably indicating less Ca segregation to the surface. For comparison, impregnated Pt materials (Pt/LCT and Pt/γ-Al_2O_3) were prepared with the same Pt loading of 0.5 wt% (Fig. 5-3) (as discussed in the next chapter). Notably, the impregnated Pt/LCT figure 5-3b shows morphological variation and increased size.

The proposed mechanism for Pt migration toward the surface is similar for Pt-L(Sr)T and Pt-L(C)T. Upon reduction, oxygen deficiency is much greater after 700°C in 5%H_2Ar, causing Pt atoms to migrate toward the oxygen-deficient surface of the perovskite, primarily forming an atomic disordered array below the surface, and in and around high energy areas such as pores, grains and pore necks. The difference in energy is enough to selectively promote Pt upon reduction to a specific surface area of higher free energy. An example of this is seen in Figures 4-9 and 4-10a-c (Pt+LCT), whereby a surface showing both bulk and exposed surfaces is clearly visible. The exposed surface (to a reductive atmosphere) is decorated in nanoparticles, and the surface that was in the bulk and not exposed does not have any coverage. Conversely, areas within the bulk that have been exposed to a reductive atmosphere at the same time as the surface display the same level of nanoparticle decoration (Figure 4-11).

4-9

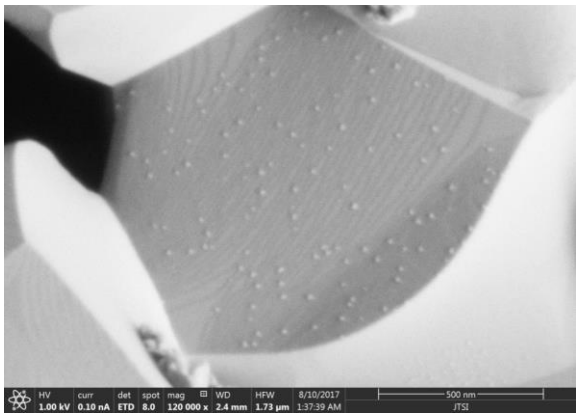

4-10a

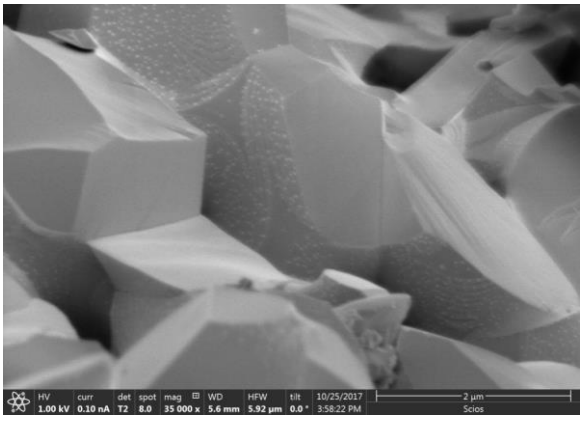

4-10b

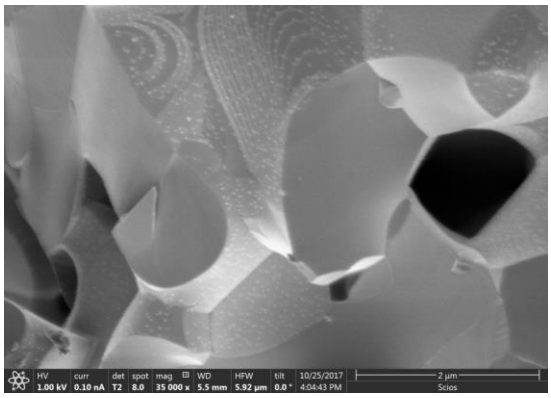

4-10c

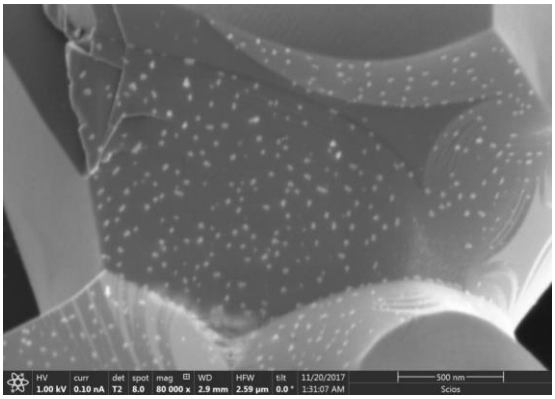

Figure 4-9a shows the cleaved area of a Pt+LCT pellet that has been reduced in 5%H_2Ar at 600°C for 12 hours. The pellet itself has been cleaved after reduction. Figure 4-10a shows the cleaved area of a Pt+LCT pellet that has been reduced in 5%H_2Ar at 700°C for 30 hours. Here the pellet has been cleaved after reduction showing preferential emergence toward exposed surfaces during reduction. Figure 4-10b shows the cleaved area of a Pt+LCT pellet that has been reduced in 5%H_2Ar at 700°C for 30 hours. Here the pellet has been cleaved after reduction showing preferential emergence toward exposed surfaces during reduction. Figure 4-10c shows the cleaved area of a Pt+LCT pellet that has been reduced in 5%H_2Ar at 700°C for 30 hours. Here the pellet has been cleaved after reduction showing preferential emergence toward exposed surfaces during reduction then further reduced again for 12 hours, showing little emergence on the freshly cleaved surface.

4-11a

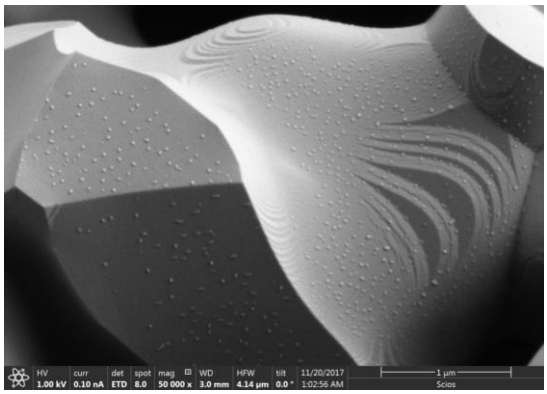

4-11b

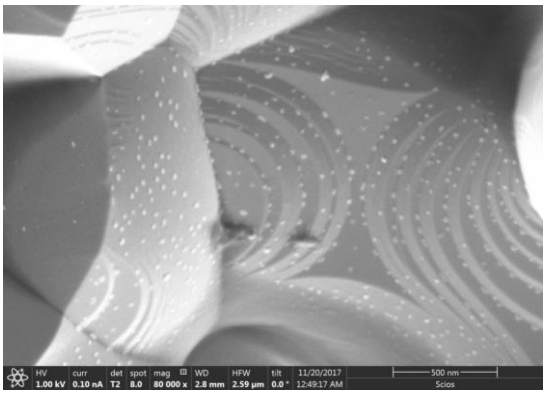

4-11d

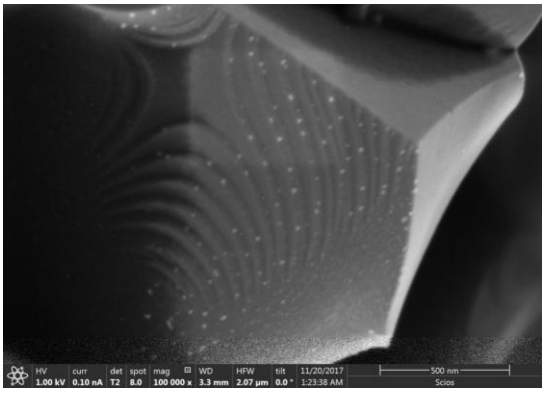

4-11e

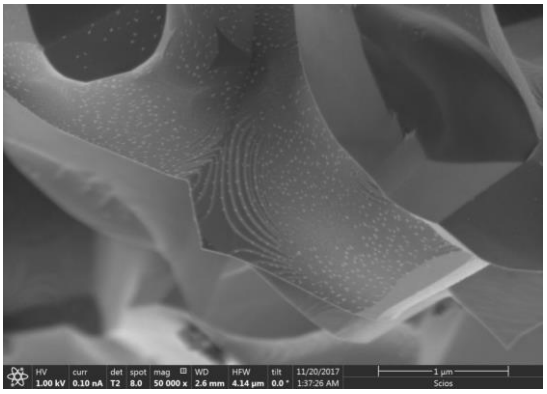

4-11f

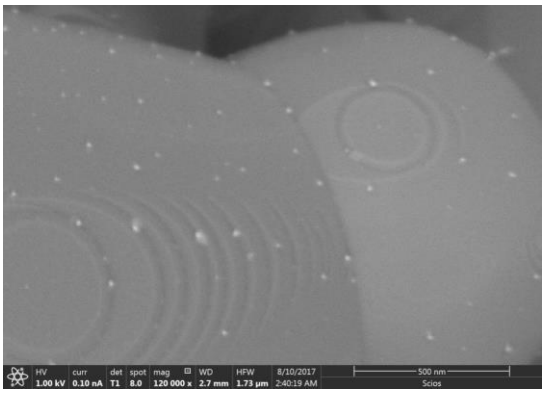

4-11g

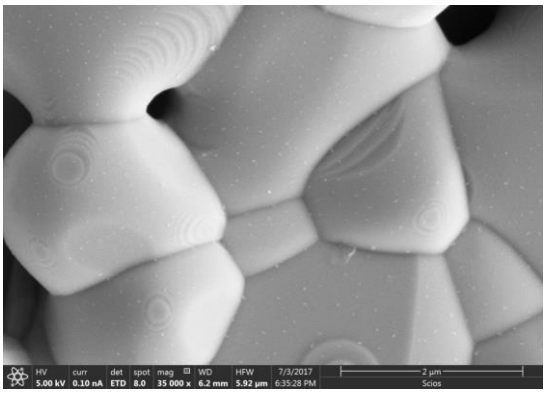

Figure 4-11a shows the cleaved area of a Pt+LCT pellet that has been reduced in 5%H_2Ar at 700°C for 12 hours. The pellet itself has been cleaved before reduction showing Pt nanoparticles on both the surface and bulk of the perovskite. Figure 4-11b shows the cleaved area of a Pt+LCT pellet that has been reduced in 5%H_2Ar at 1000°C for 12 hours. The pellet itself has been cleaved after reduction. Clear terracing is visible. Figure 4-11d shows the cleaved area of a Pt+LCT pellet that has been reduced in 5%H_2Ar at 500°C for 12 hours. Full decoration has not occurred as all the Pt has yet to migrate to the surface of the perovskite. Figure 4-11e shows the cleaved area of a Pt+LCT pellet that has been reduced in 5%H_2Ar at 500°C for 12 hours. Full decoration has not occurred as all the Pt has yet to migrate to the surface of the perovskite. The pellet has been cleaved after reduction in this instance.

Figure 4-11f shows the surface area of a Pt+LCT pellet that has been reduced in 5%H_2Ar at 700°C for 12 hours. Figure 4-11g shows the surface area of a Pt+LCT pellet that has been reduced in 5%H_2Ar at 600°C for 12 hours. Full decoration has not occurred as all the Pt has yet to migrate to the surface of the perovskite.

Pt/LST displays distinctive bipyramidal morphology and only in certain areas of the perovskite surface. This can be attributed to the Sr cation and its surface effects. The mechanism is only slightly different to Pt+LCT, as Sr is the only difference in composition. In reductive environments, oxygen non-stoichiometry and cation concentration are driven in part by high temperature and oxygen partial pressure. The surface of the perovskite can form an energy barrier to full reduction as a pellet, causing the surface area to become a separate phase, or bi-phasic in relation to the bulk. Sr cation segregation has previously been observed[7] on $SrTiO_3$, $LaSrMnO_3$[6]. The Sr cation congregates in Sr-rich areas at the surface, causing an A site misbalance in the surface phase, as the A site cation migrate towards Sr-rich areas, and deficient Sr areas are more energetically favourable for Pt cations. This results in patches of platinum nanoparticle emergence and Sr-rich areas void of B site cation nanoparticles. The A site cation segregation can cause further electronic changes to the structure's nanoparticle shape and catalytic properties. The microstructure of Pt+LST differs from Pt+LCT slightly with a more rounded nodule formation (Figure 4-12a-c), with clear embedded bipyramidal Pt nanoparticles in specific segregated areas (Figure 4-12a). Furthermore, Sr-rich surface areas were confirmed by HAADF TEM (Figure 4-13), whereby the heavier Sr cation segregation from the bulk is distinctly visible along with Ba. In these areas, little or no Pt nanoparticles were found.

4-12a

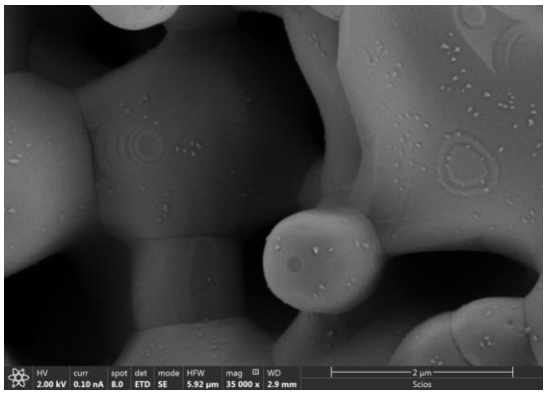

4-12b

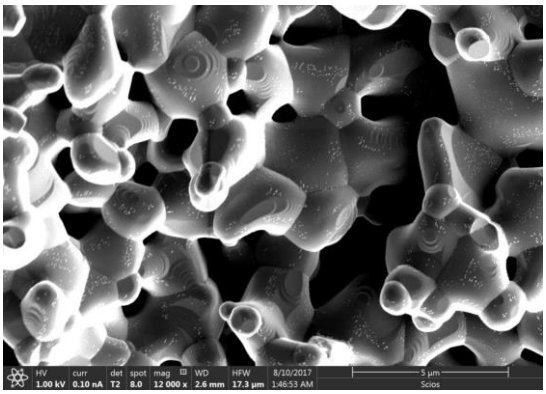

Figure 4-12a shows Pt+LST reduced in 5%H_2Ar for 12 hours at 800°C. Pt nanoparticles have grown in Sr deficient areas at the surface of the perovskite and are visible clearly on nodules. Figure 4-12b Pt+LST reduced in 5%H2Ar for 12 Hours at 800°C, distinct morphological bipyramidal Pt nanoparticles are visible in Sr-deficient areas of the perovskite surface.

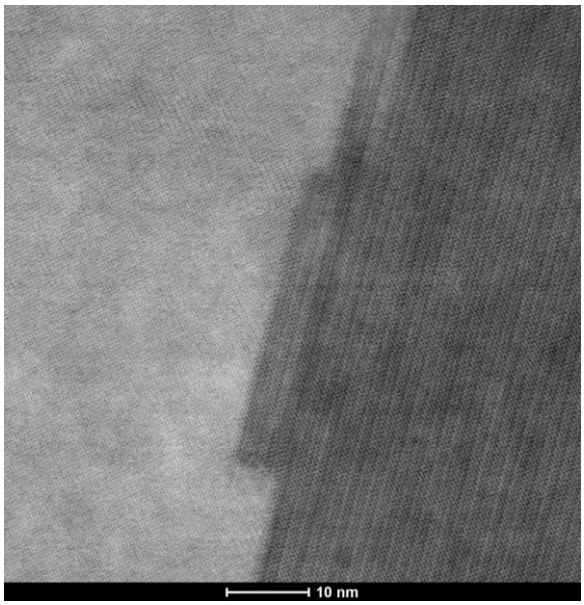

Figure 4-13 shows dark field HAADF TEM of Sr segregation atoms near to the surface of Pt@LST.

Morphologically distinct traits of Pt nanoparticles occur in both Pt/L(C/S)T, and for Pt+LCT, spherical nanoparticles formed throughout. Visible embedding is clear, especially in an FIB lamellar of the Pt+LCT (field ionisation beam SEM cut with a Ga beam) (Figure 4-3a,b). Figure 4-14 shows the TEM of the lamellar with an embedded nanoparticle firmly rooted within the structure, showing the spherical morphology and its shape within the structure. For Pt/LST, Figure 4-15 TEM shows the pyramid structure of Pt on the surface.

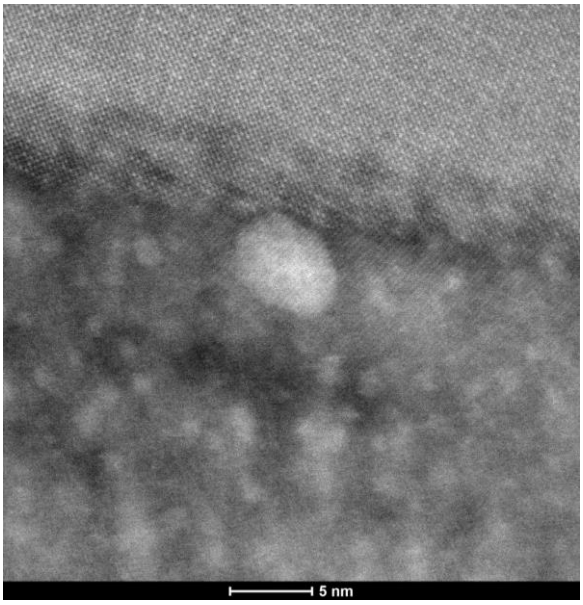

Figure 4-14 shows Pt+LCT TEM of the lamellar with an embedded nanoparticle firmly rooted within the structure, reduced at 700°C for 12 hours in 5%H_2Ar.

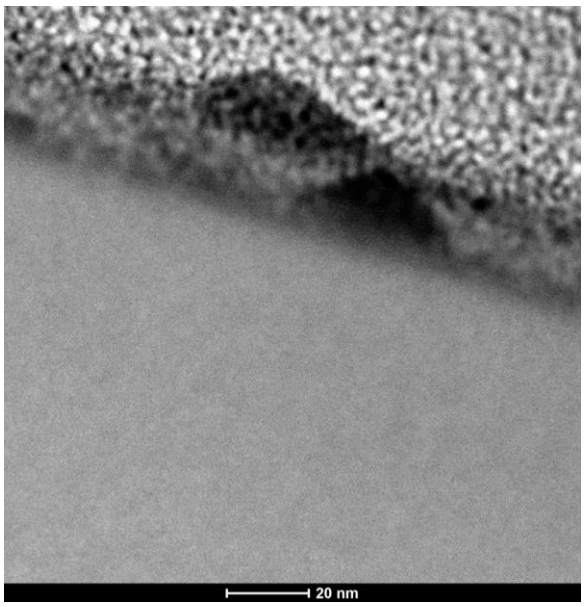

Figure 4-15 shows a bipyramidal Pt+LST that has been reduced in 5%H_2Ar for 12 hours at 700°C.

Free energy and surface nanoparticle formation are strongly correlated to one another – Pt cations first migrate toward neck regions of pores, and subsequently, to grains, where the surface energy is higher than the bulk. Evidence of this can be seen in SEM Figure 4-16 and TEM Figure 4-17, whereby Pt+LCT was reduced for 4 hours at 500°C in 5%H_2Ar. Individual nanoparticle formation around grains and pores can be seen at this early stage, after 12 hours at 600°C in 5%H_2Ar migration throughout the surface occurs, yielding a well distributed and decorated surface (Figure 4-18a-c).

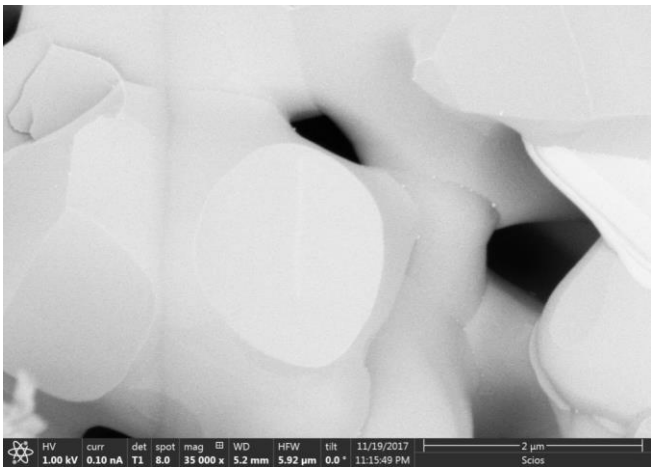

Figure 4-16 shows Pt+LCT reduced for 4 hours at 500°C in 5%H_2Ar, with minimal emergence of Pt nanoparticles showing through the surface

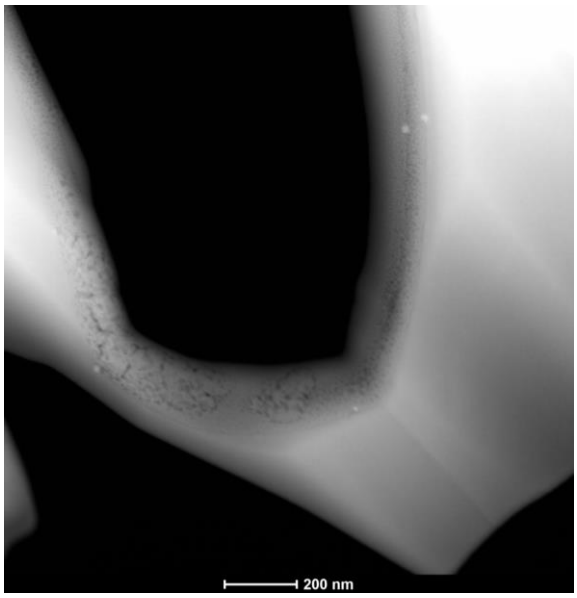

Figure 4-17 shows Pt+LCT reduced for 4 hours at 500°C in 5%H_2Ar with some Pt nanoparticles within a pore region near the neck and grain.

4-18a

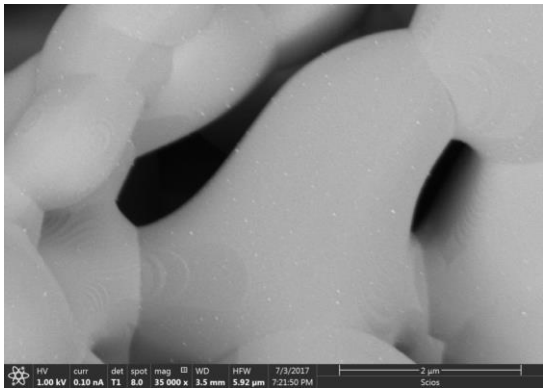

4-18b

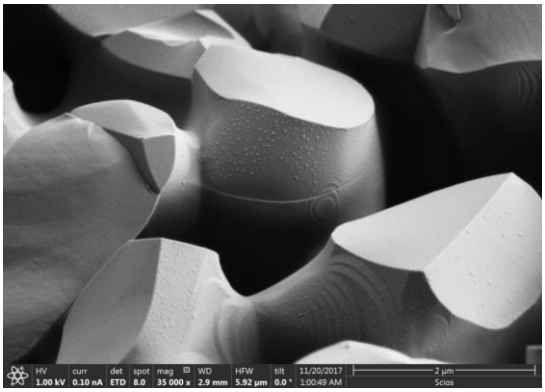

4-18c

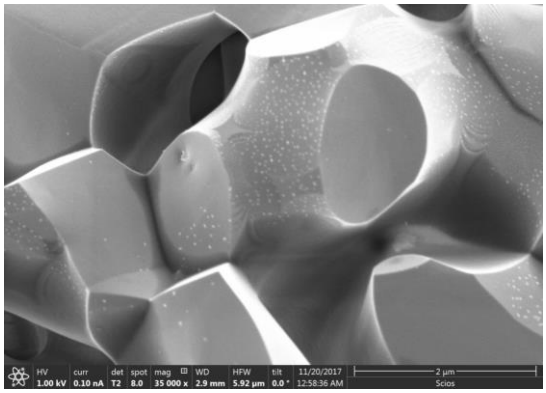

4-18d

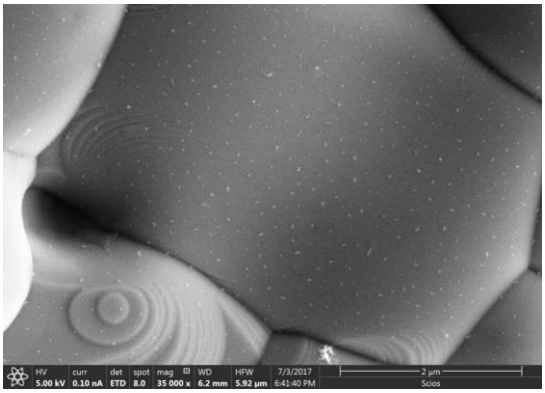

4-18e

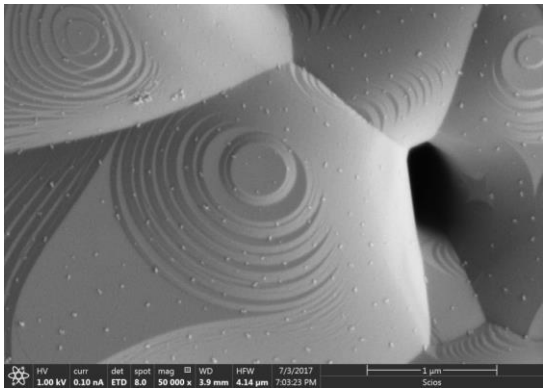

4-18f

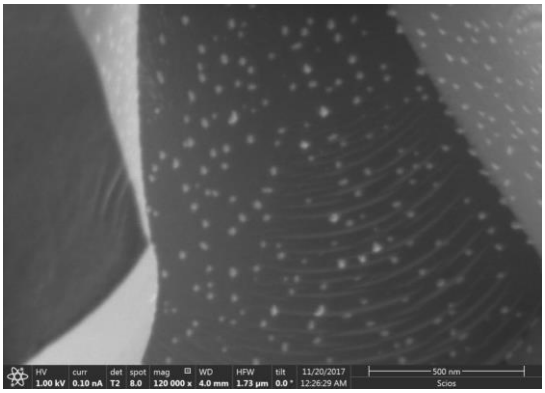

4-18a shows the cleaved area of a Pt+LCT pellet that has been reduced in 5%H_2Ar at 600°C for 12 hours.Figure 4-18b shows the cleaved area of a Pt+LCT pellet that has been reduced in 5%H_2Ar at 700°C for 12 hours. The pellet itself has been cleaved before reduction. Figure 4-18c shows the cleaved area of a Pt+LCT pellet that has been reduced in 5%H_2Ar at 700°C for 12 hours. The pellet itself has been cleaved after reduction. Figure 4-18d shows the surface area of a Pt+LCT pellet that has been reduced in 5%H_2Ar at 600°C for 12 hours. Figure 4-18e shows the surface area of a Pt+LCT pellet that has been reduced in 5%H_2Ar at 700°C for 12 hours. Figure 4-18f shows the cleaved area of a Pt+LCT pellet that has been reduced in 5%H_2Ar at 800°C for 12 hours.

Confirmation of the elemental makeup of the nanoparticles was confirmed by HR-TEM and X-ray dispersion spectroscopy (EDX), as seen in Figure 4-8d. Surface and bulk nanoparticle analysis confirms the mechanism of surface Pt migration. Figure 4-19a-b shows a cut lamellar of used to study surface nanoparticles; by cutting a cross-section, it was possible to determine the morphological anchoring to the perovskite surface.

4-19a

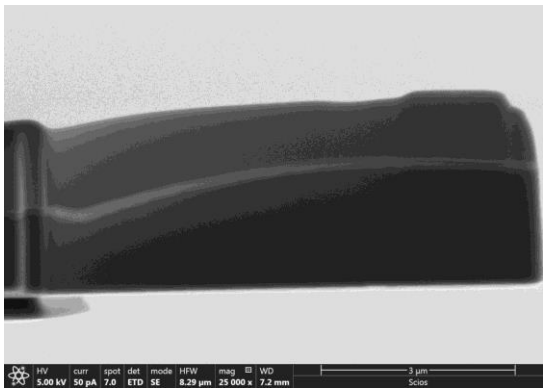

4-19b

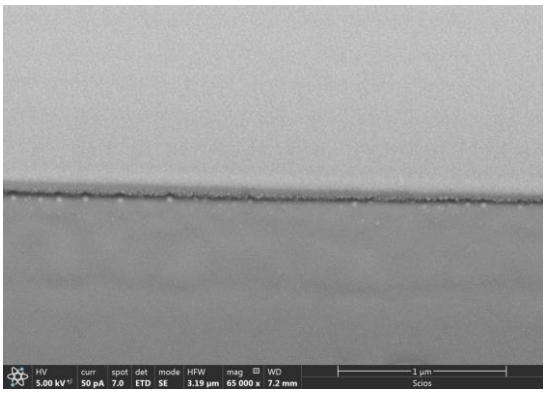

Figures 4-19a and 4-19b show FIB lamellar preparation of Pt+LCT with non-decorated Pt on the surface, despite the Pt deposition it is possible to see the nanoparticles clearly underneath.

Figure 4-19 confirms a semi-buried and anchored nanoparticle within the surface, and above the particle is a layer of Pt deposition. The contact angle of the nanoparticle is less than 90°, and there is a strong metal support interaction (SMSI) between the perovskite and the Pt nanoparticle, preventing movement in a high reducing temperature environment. It is likely that as Pt cations coalesce on the perovskite surface, strong interatomic bonds between A-site deficient vacancies form, anchoring the particles to the surface like a concerticious glue.

A contact angle of less than 90° is observed, and a diamond pyramidal tip is deeply embedded within the surface of the perovskite. Even after a very high temperature and highly reductive conditions, the Pt nanoparticle remains embedded within the surface of the perovskite. Furthermore, surface nanoparticle dispersion shows no agglomeration between 12 hours and 30 hours at 700°C reduced in 5%H_2Ar (Figure 4-21 for 12 hours and Figure 4-22 for 30 hours), further exemplifying the SMSI and

anchoring effect between Pt nanoparticles and the A-site deficient perovskite surface. As there is little to no agglomeration between highly reductive cycles, it is assumed that Pt is well and truly bound to perovskite structure, separating itself from the structure only from chemical attack rather than redox and high temperature events.

Figure 4-21

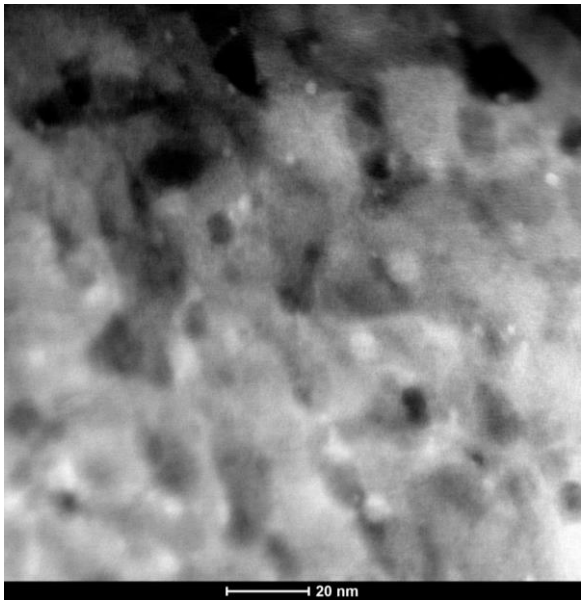

Figure 4-22

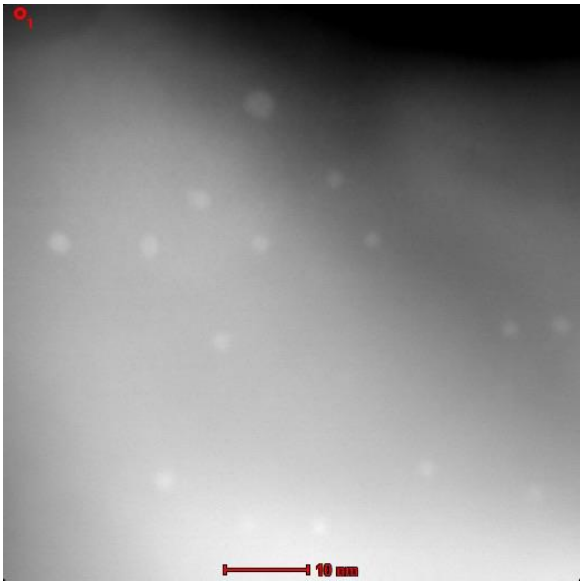

Figure 4-21 shows Pt+LCT first reduced at 700°C for 12 hours in 5%H_2Ar followed by oxidation in air at 1000°C for 750 hours. There is little movement of the embedded Pt nanoparticles Figure 4-22 shows Pt+LCT first reduced at 700°C for 30 hours in 5%H_2Ar followed by oxidation in air at 1000°C for 750 hours. There is little movement of the embedded Pt nanoparticles

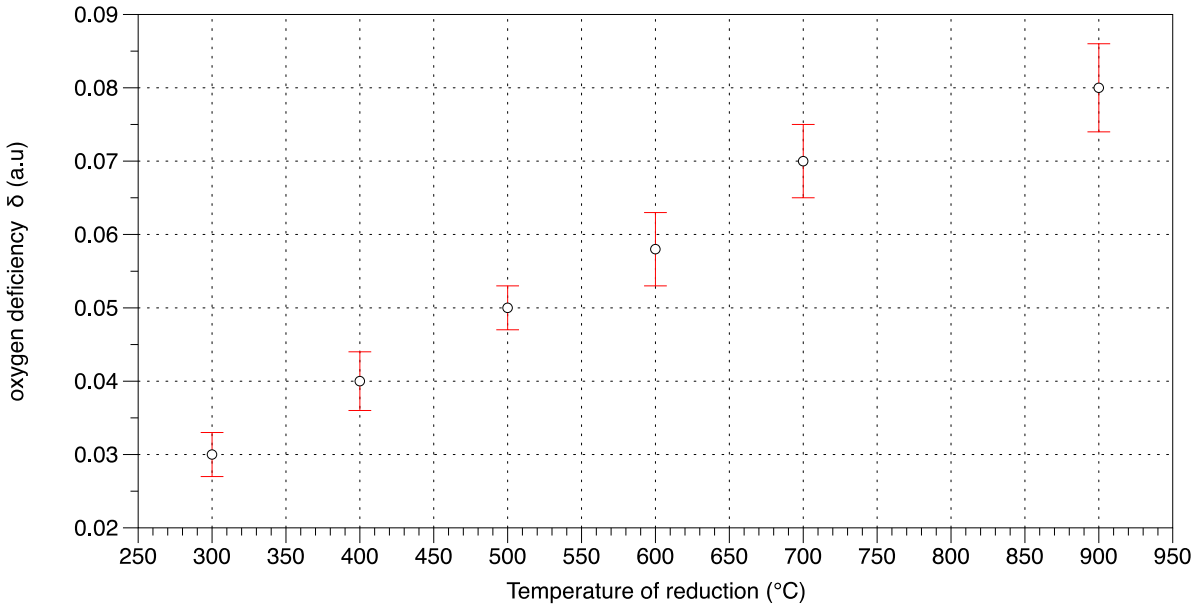

Figure 4-23: The as-calculated average oxygen deficiency of 3 samples (for each data point) in different temperature environments from thermogravimetric analysis.

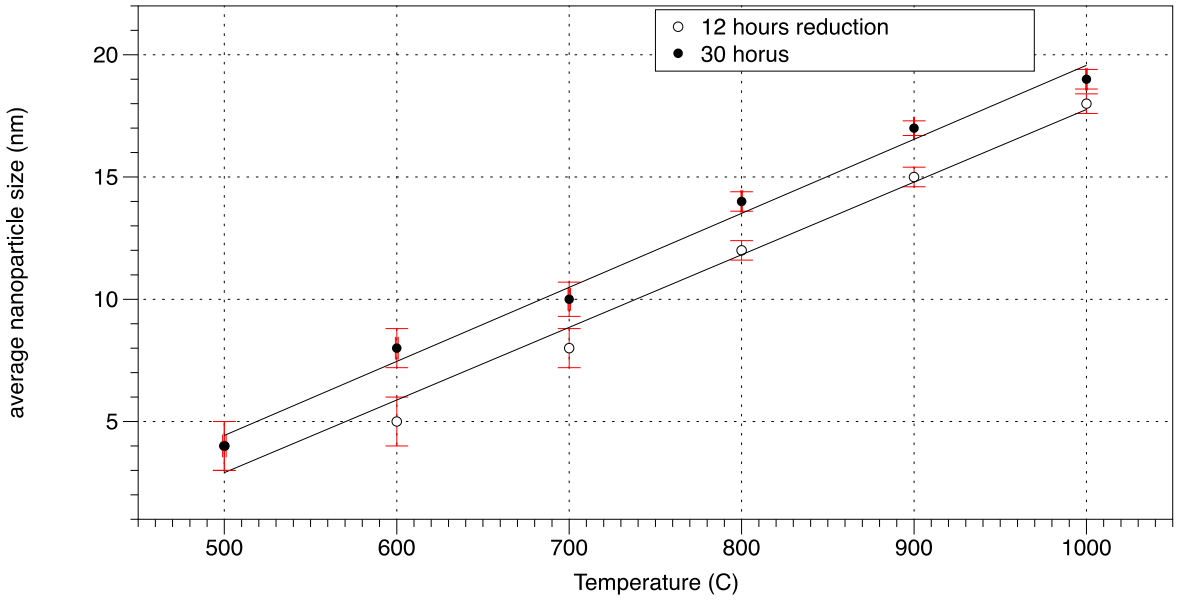

Figure 4-24: Average Pt nanoparticle in reducing conditions (5%H_2Ar) for Pt+LCT at 12 and 30 hours, respectively, at temperatures from 500-1000°C, as calculated from ImageJ of flat pellet surface with error.

Even though SMSI allows Pt nanoparticles to be bound and anchored to the reduction for longer periods of time, the temperature allows the nanoparticles to grow (Figure 4-24) to a maximum size of 20nm after 30 hours in a reductive environment. Durations of 12 and 30 hours were tested on

Pt+LCT ranging from 500-1000°C, and particle size and dispersion were calculated using ImageJ software (Figures 4-25 and 4-26a-b). It is noteworthy that even after 1200°C in 5%H_2Ar (Figure 4-27), the Pt particle size did not grow beyond 30nm. With the morphology and the anchoring, it is assumed that only 50-80% of the nanoparticle is exposed on the surface of the perovskite resulting in a smaller area for potential catalytic reactions to occur over. Another way of calculating the particle size to compare with particle counting from SEM micrographs is by studying the area under the metallic Pt peak of reduced samples by XRD analysis.

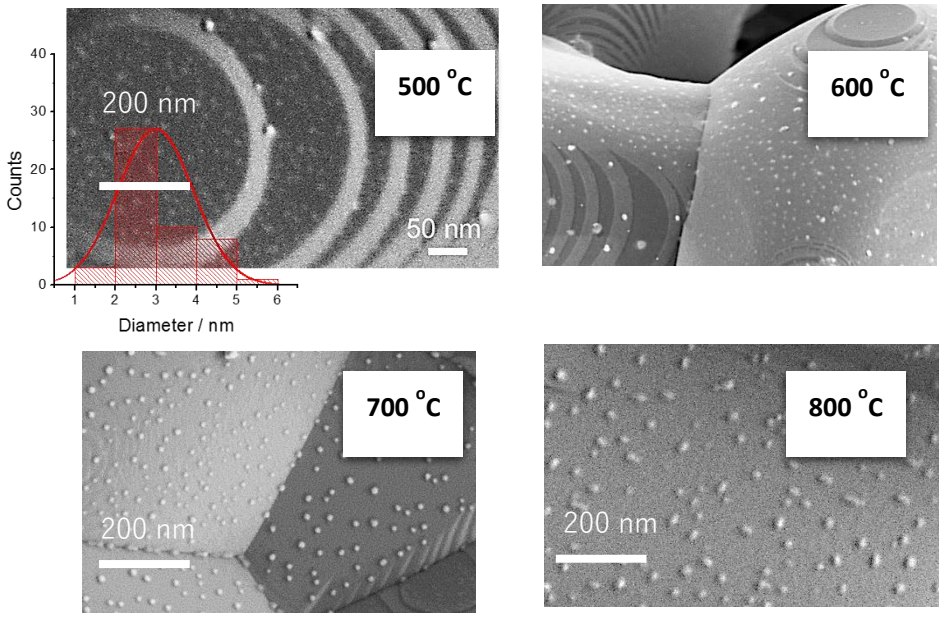

Figure 4-25 shows particle dispersion, morphology and size for four temperature ranges. From 500-800°C. With dispersion and size calculated by ImageJ.

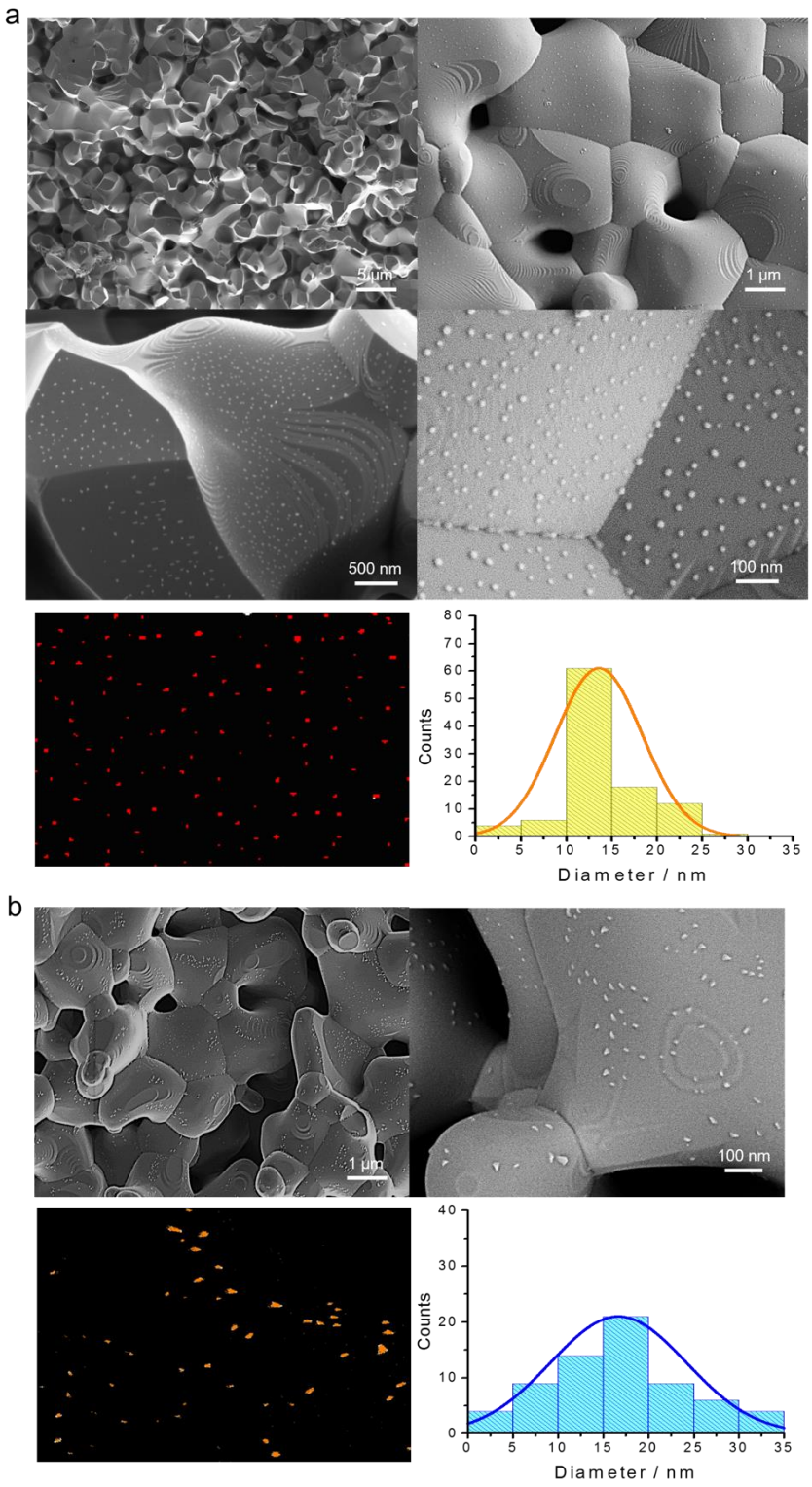

Figure 4-26 a and b show the surface of Pt+LCT and Pt+LST reduced for 12 hours in 5%H_2Ar at 700°C. With particle distribution and size calculated using image J software.

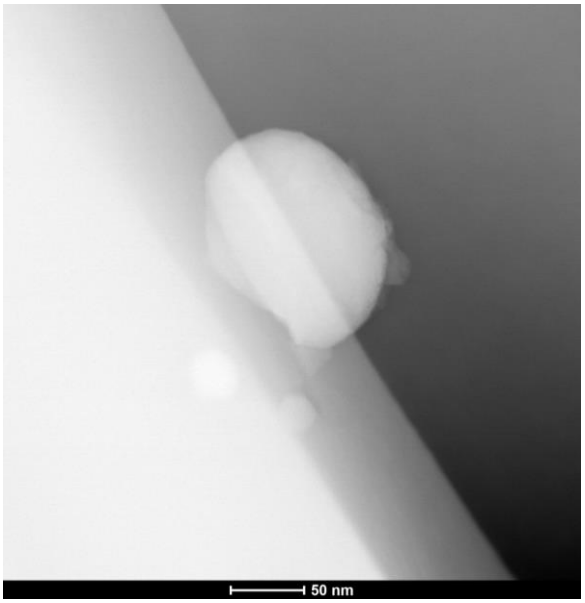

Figure 4-27 shows a large buried nanoparticle of Pt Pt+LCT reduced at 1200°C for 50 hours in 5%H_2Ar.

This is done by using the Scherrer equation[8]:

$$B = \frac{K\lambda}{L\cos\theta}$$

Whereby B is the crystalline size (in this case Pt nanoparticle), K is the Scherrer constant (shape), λ is the wave length of the incident X-ray, L is the FWHM (full width half maximum) and θ is the angle of diffraction.

The comparison of the two methods gives a good example of the proposed difference in what can be 'seen' in an SEM micrograph (Figure 4-25) with what is actually 'there' with an XRD (Figure 4-28).

It is assumed that the difference between particle size can be attributed to buried and embedded Pt that cannot be seen by SEM with XRD, so in the case of Pt+LCT reduced at 800°C for 12 hours in 5%H-$_2$Ar SEM analysis reveals an average particle size of 20-30nm and 37.45 for XRD on the same pellet sample. This indication can be further confirmed by studying TEM surface particles to see the level of embedment (Figure 4-27). Typical catalytic methods such as temperature programmed reduction (TPR) and incipient transient kinetics (ITK) revealed little as to the level of Pt embedded on the surface, which was due to the very low wt.% of Pt within the sample and the dense perovskite itself. Quantitatively, a combination of oxygen loss (calculated by TGA), particle analysis SEM and TEM analysis gave confirmation of full Pt coverage and migration of Pt out of the bulk toward the surface after 700°C in 5%H_2Ar for 12 hours.

In order to check the embedded nature of the Pt nanoparticles aqua regia was used to etch the Pt away from the perovskite bulk (Figure 4-29). Although this left the surface very dirty under observation in an SEM, it was evident that the pitting of Pt nanoparticles can be confirmed.

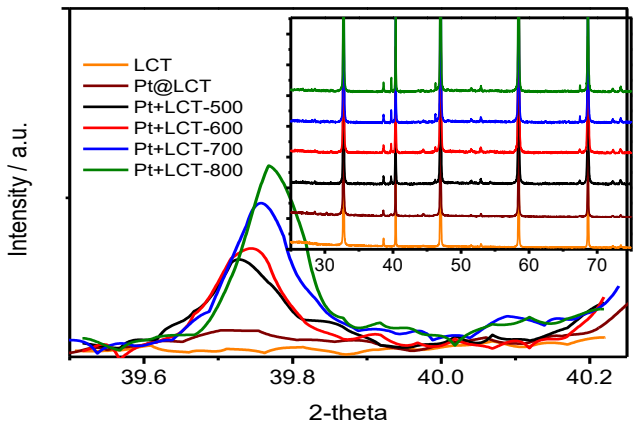

Figure 4-28 shows the XRD for reduced samples from 500-800°C in 5%H_2Ar for 12 hours. The Pt peak is observable at 39-39.8θ..From the area under the peak it is possible to gain a understanding of the Pt nanoparticle size.

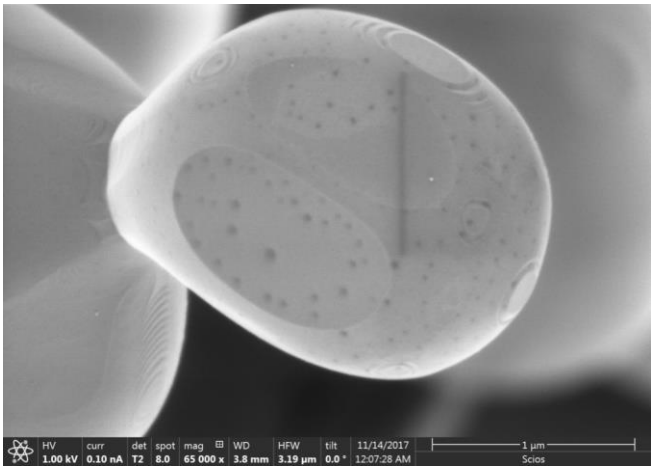

Figure 4-29 shows Pt+LCT reduced at 1000°C for 30 hours followed by etching with aqua regia to etch the Pt away from the perovskite bulk.

	500 °C	600 °C	700 °C	800 °C
SEM	**2-6 nm**	**6-12 nm**	**12-20 nm**	**20-30 nm**
XRD (Mean size)	**9.11 nm**	**17.26 nm**	**26.12 nm**	**37.45 nm**

Table 4-1 shows the Pt nanoparticle size difference between the two calculation methods of particle counting via image J software and calculations based on the Scherrer equation.

As discussed in chapter 1, work by H. Tanaka and Daihatsu Motor Corporation revealed the supposed intelligent redox ability of Pd nanoparticles in between the surface and bulk, which would require a much greater amount of free energy than is available in a typical TWC exhaust[9] (temperature and reactants). The proposed solid-state material and mechanism in this thesis show that after redox environments, the Pt nanoparticles do not move and are firmly rooted to the surface of the perovskite structure due in part to the embedded nanoparticle and the interaction between the perovskite support.

After redox in 5%H_2Ar at 700°C for 12 hours followed by 300 hours in an air furnace at 1000°, there is no movement of Pt nanoparticles from the surface. Furthermore, after 12 hours at 700°C in 5%H_2Ar followed by 750 hours at 1000°C re-oxidation in air, only the surface of the perovskite shows signs deterioration on the terracing, although the Pt nanoparticles remained in place and of the same size (Figure 4-30).

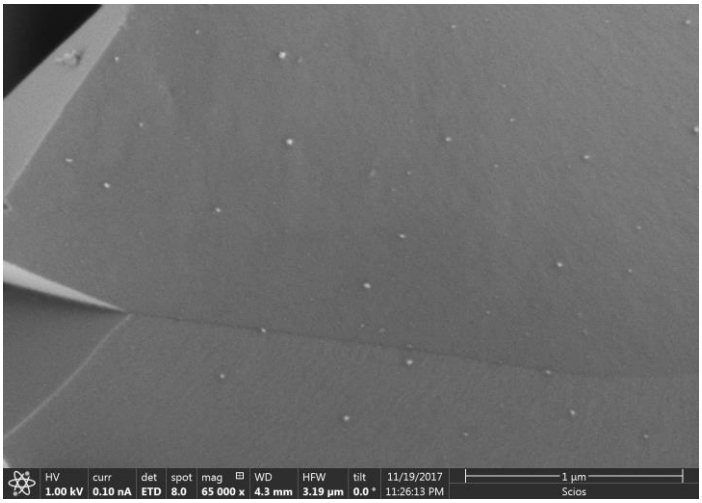

Figure 4-30 shows Pt+LCT reduced first in 5%H_2Ar for 30 hours at 700°C followed by 750 hours at 1000°C reoxidation in air.

This is a very important feature of A-site deficient materials and for these materials specifically, as it allows us to tailor the materials for long-term catalytic applications. HR-TEM of a sample that has been through the 750 hour redox process is shown in Figures 4-31a-b, where the preservation of the nanoparticle is visible on the surface, with visible segregation between the bulk and surface, due to the redox effect on the perovskite. One could assume if the material was powdered with a small particle size >1um and with a much higher surface area, all of the system phases would be similar in nature.

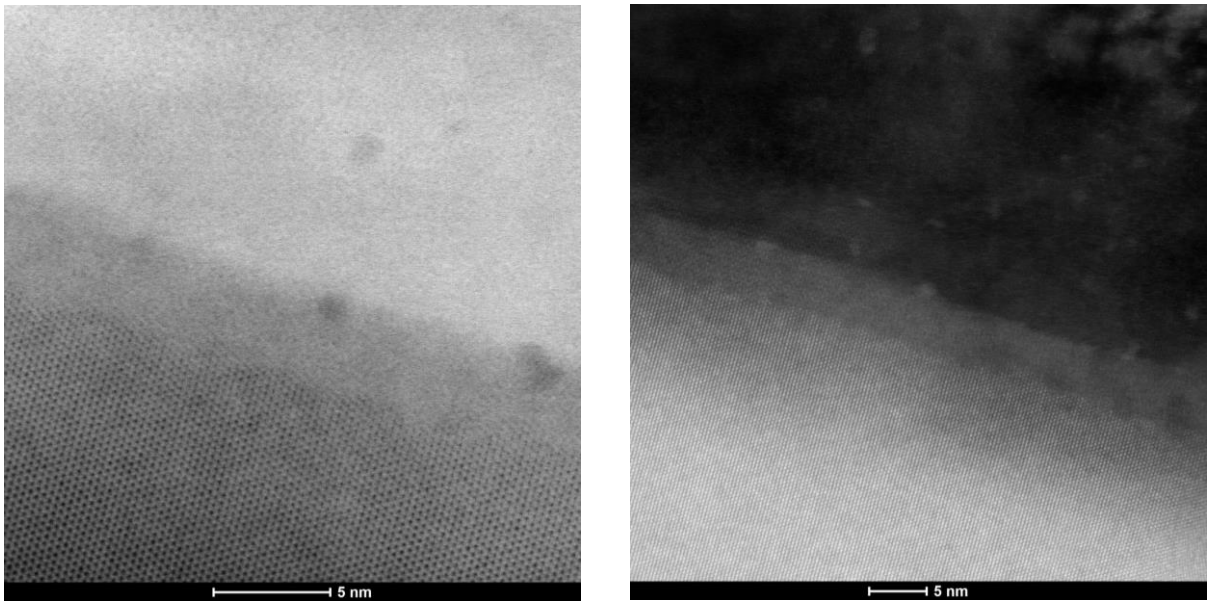

Figure 4-31a -b shows Pt+LCT first reduced at 700°C for 30 hours in 5%H_2Ar followed by oxidation in air at 1000°C for 750 hours. There is little movement of the embedded Pt nanoparticles.

Oxidation

In order to determine the oxidation chemistry of Pt nano-particles, XANES and EXAFS analysis was carried out in order to determine the localised oxidation state of Pt and to observe if there was any Pt metal prior to reduction.

The Pt LIII-edge XANES spectra of reduced Pt@LCT in figure 4-32 confirms the metallic valence state of the emerged Pt NPs from the white-line shape and intensity, with a small difference in amplitude comparing with Pt foil.

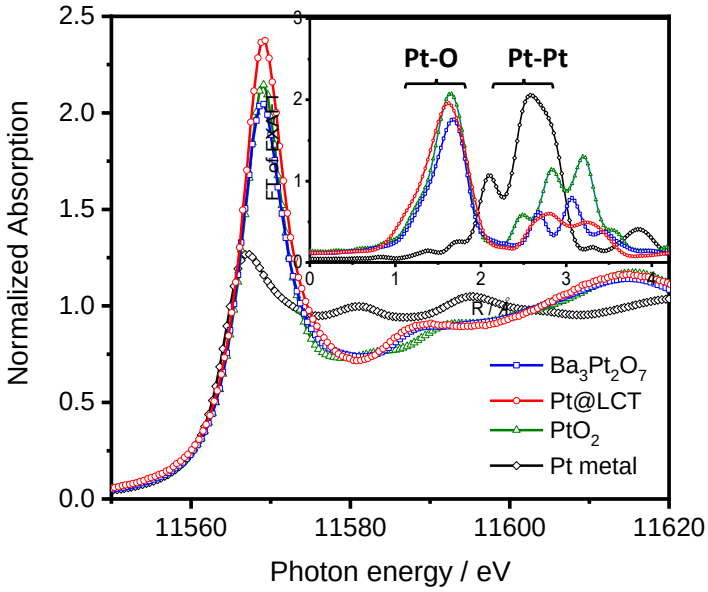

Figure 4-32 shows XANES spectra of the Pt L_{III}-edge (inset: EXAFS spectra of the Pt L_{III}-edge) for $Ba_3Pt_2O_7$, **Pt@LCT**, PtO_2 and Pt foil.

This might be caused by a morphology effect or by positively charged Pt species from a d-electron density decrease due to the charge transfer of Pt@LCT support, which may result in efficient catalytic properties. The EXAFS analysis in Figure 4-33 shows also metallic Pt species from the strong contribution from Pt-Pt bonding (~2.7 Å). Remarkably, close examination of Pt-Pt shell for the emerged Pt +LCT ($La_{0.4}Ca_{0.4}TiO_3$) reveals a high reduction in the intensity, compared to the other

impregnated Pt references. The reduced amplitude links to the reduction of the average coordination number of 12 for the Pt-Pt bonding in the Pt metal bulk.

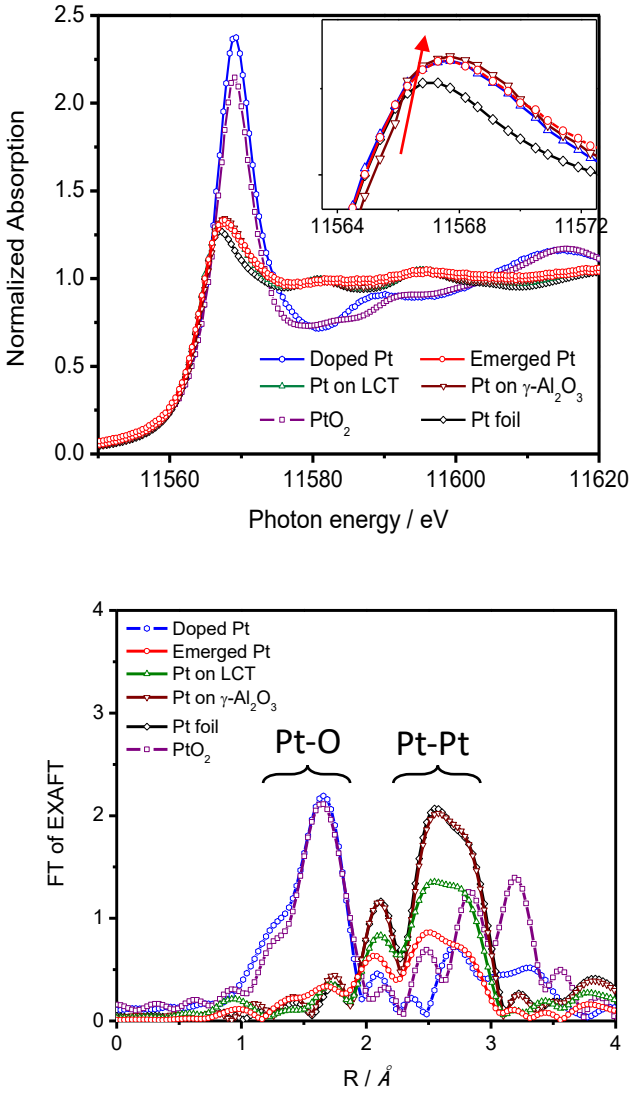

Figure 4-33 XANES and (g) EXAFS spectra of the Pt L_{III}-edge for the **Pt@LCT, Pt+LCT**, **Pt/LCT**, **Pt/γ-Al_2O_3**, PtO_2 and Pt foil.

From the refined analysis in Fig. 4-34 and Table 5-3d, the Debye-Waller factor (σ2) increases with a reduction of the interatomic distance (R), suggesting a strong structural disordering of the emerged Pt.

Both observations are consistent with a strong interaction between the Pt NPs and perovskite bulk, which could contribute to the stabilization of the Pt NPs in sintering conditions.

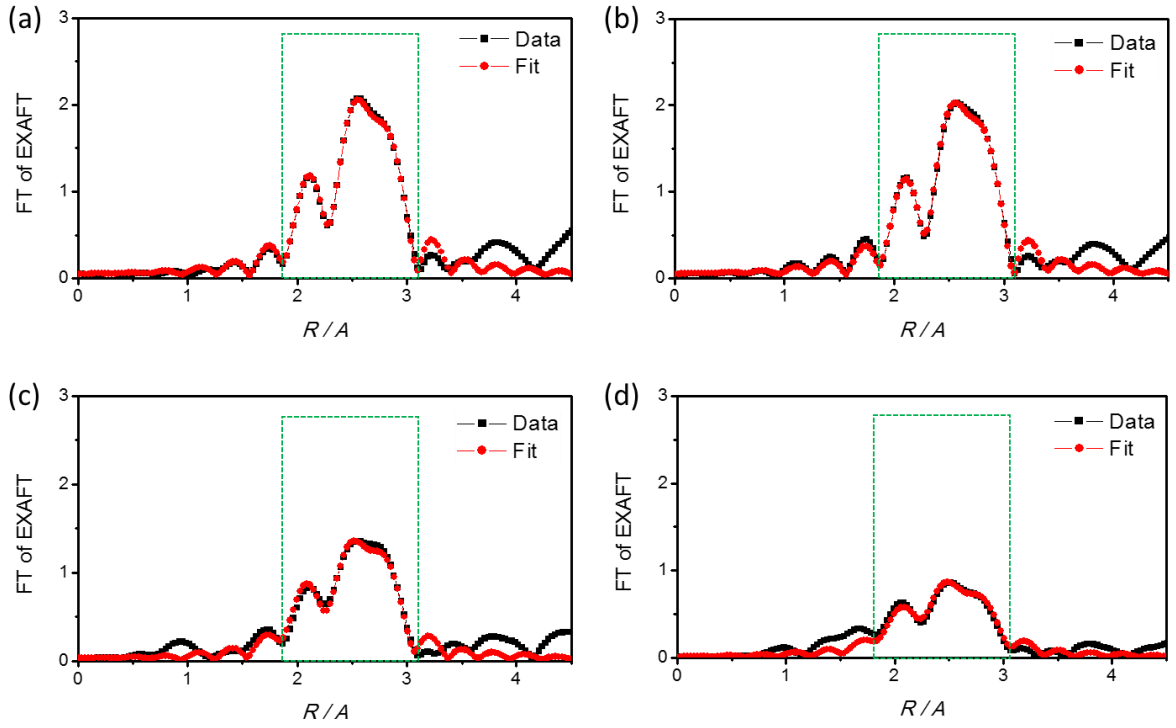

Figure 4-34: X-ray absorption fine structure. EXAFS data analysis of the Pt L_{III}-edge by comparing experimental data and the fitting curves (R-range=1.8-3.12 Å) for (a) Pt foil, (b) Pt/γ-Al_2O_3, (c) Pt/LCT and (d) Pt+LCT.

Summary and conclusion

The formation of Pt nanoparticles via emergence only occurred after the use of co-precursor Barium Platinate. SEM micrographs prior to this disproved any controlled emergence of Pt NP's. After the incorporation of Barium Platinate and sintering in oxygen as well as a tailored wt% clear controlled emergence can be observed. The temperature of reduction and time are critical to growing the Pt NP's out of the perovskite system toward the exposed surface. By reducing and observing exposed surfaces only it was possible to prove emergence of Pt NP's occurs at the interface of the perovskite mixed oxide

which is in contact with the reducing gas in this case 5%H_2/Ar. A full study on temperature and time whilst observing the size of the nano particles was carried out. Alongside this HR-TEM was undertaken to determine the atomic resolution on the perovskite oxide. Pt+LST resulted in Barium cation segregation, in areas where the Barium cation was limited, Strontium cations had segregated and thus preferential emergence of Pt NP's in areas of Ba atomic clusters occurred indicating that cation choice is crucial to forming a well defined system. Finally, the crystallinity and oxidation chemistry of the Pt perovskite system was proved by XANES/EXAFS and the corresponding fitting model proving that Pt^0 forms after a reduction event over 700℃. The oxidation chemistry of Pt@LCT prior to reduction show Pt^{4+} indicating that Pt is within the perovskite crystal structure and has formed at high temperature.

In conclusion the microstructure and oxidation chemistry are critical to determining if Pt incorporation within the perovskite system has occurred. The uniform and embedded nature of the Pt nano particles is critically important to catalytic reaction studies.

References

1. Galassi, G. & Spada, G. Sea-level rise in the Mediterranean Sea by 2050: Roles of terrestrial ice melt, steric effects and glacial isostatic adjustment. *Glob. Planet. Change* **123**, 55–66 (2014).
2. Rowley, R. J., Kostelnick, J. C., Braaten, D., Li, X. & Meisel, J. Risk of Rising Sea Level to Population and Land Area. *Eos, Trans. Am. Geophys. Union* **88**, 105 (2007).
3. Alley, R. B., Clark, P. U., Huybrechts, P. & Joughin, I. Ice-sheet and sea-level changes. *Science* **310**, 456–60 (2005).
4. Cox, P. M., Betts, R. A., Jones, C. D., Spall, S. A. & Totterdell, I. J. Acceleration of global warming due to carbon-cycle feedbacks in a coupled climate model. *Nature* **408**, 184–187 (2000).
5. Corma, A. & López Nieto, J. M. *The Role of Rare Earths in Catalysis*. *Handbook on the Physics and Chemistry of Rare Earths* **29**, (Elsevier, 2000).
6. BY se G. le. 3–5 (1973).
7. Cohn, J. G. Catalytic converters for exhaust emission control of commercial equipment powered by internal combustion engines. *Environ. Health Perspect.* **10**, 159–164 (1975).
8. Farrauto, R. J., Deeba, M. & Alerasool, S. journey to cleaner air. *Nat. Catal.* **2**, 603–613 (2021).
9. Eastwood, P. *Critical topics in exhaust gas aftertreatment*. (Research Studies Press, 2000).
10. Summers, J. C., Sawyer, J. E. & Frost, A. C. The 1990 Clean Air Act and Catalytic Emission Control Technology for Stationary Sources. in *Catalytic Control of Air Pollution* **495**, 8–98 (American Chemical Society, 1992).
11. Libby, W. F. Promising Catalyst for Auto Exhaust. *Science (80-.).* **171**, 499–500 (1971).
12. Twigg, M. V. Progress and future challenges in controlling automotive exhaust gas emissions. *Appl. Catal. B Environ.* **70**, 2–15 (2007).
13. Russell, A., Epling, W. S., Russell, A. & Epling, W. S. Diesel Oxidation Catalysts Diesel Oxidation Catalysts. **4940**, (2011).
14. Twigg, M. V. Catalytic control of emissions from cars. *Catal. Today* **163**, 33–41 (2011).
15. Matthey, J. Johnson Matthey Annual Report 2018 - customers. (2018).
16. Misono, M. Mixed Oxides as Catalyst Supports. **176**, 157–173 (2013).
17. Tanaka, H. & Misono, M. Advances in designing perovskite catalysts. *Curr. Opin. Solid State Mater.* (2001).
18. Tanaka, H. *et al.* Design of the intelligent catalyst for Japan ULEV standard. *Top. Catal.* **30/31**, 389–396 (2004).
19. Screen, T. Platinum Group Metal Perovskite Catalysts. *Platin. Met. Rev.* **51**, 87–92 (2007).
20. Russell, A. & Epling, W. S. Diesel Oxidation Catalysts. *Catal. Rev.* **53**, 337–423 (2011).
21. Kröcher, O. *et al.* Investigation of the selective catalytic reduction of NO by NH3 on Fe-ZSM5 monolith catalysts. *Appl. Catal. B Environ.* **66**, 208–216 (2006).
22. Prasad, D. H. *et al.* Effect of nickel nano-particle sintering on methane reforming activity of Ni-CGO cermet anodes for internal steam reforming SOFCs. *Appl. Catal. B Environ.* **101**, 531–539 (2011).

23. Prasad, D. H. *et al.* Effect of steam content on nickel nano-particle sintering and methane reforming activity of Ni–CZO anode cermets for internal reforming SOFCs. *Appl. Catal. A Gen.* **411**–**412**, 160–169 (2012).
24. Deng, J., Cai, M., Sun, W., Liao, X. & Chu, W. Oxidative Methane Reforming with an Intelligent Catalyst: Sintering-Tolerant Supported Nickel Nanoparticles. (2013).
25. Nishihata, Y. *et al.* Self-regeneration of a Pd-perovskite catalyst for automotive emissions control. *Nature* **418**, 164–167 (2002).
26. Tanaka, H. *et al.* An intelligent catalyst. -*SOCIETY Automot. Eng. JAPAN* (2001).
27. Kajita, N., Uenishi, M., Tan, I., Tanaka, H. & Kimura, M. Regeneration of Precious Metals in Various Designed Intelligent Perovskite Catalysts. (2002).
28. Sato, N., Tanaka, H., Tan, I., Uenishi, M. & Kajita, N. Design of a practical Intelligent catalyst. *SAE Trans.* (2003).
29. Nishihata, Y., Mizuki, J., Tanaka, H., Uenishi, M. & Kimura, M. Self-regeneration of palladium-perovskite catalysts in modern automobiles. in *Journal of Physics and Chemistry of Solids* (2005). doi:10.1016/j.jpcs.2004.06.090
30. Tanaka, H. An intelligent catalyst: the self-regenerative palladium–perovskite catalyst for automotive emissions control. *Catal. Surv. from Asia* (2005).
31. Uenishi, M., Tanaka, H., Taniguchi, M., Tan, I. & Sakamoto, Y. The reducing capability of palladium segregated from perovskite-type LaFePdO x automotive catalysts. *Appl. Catal. A* (2005).
32. Nishihata, Y., Mizuki, J., Tanaka, H. & Uenishi, M. Self-regeneration of palladium-perovskite catalysts in modern automobiles. *J. Phys.* (2005).
33. Tanaka, H., Tan, I., Uenishi, M., Taniguchi, M. & Nishihata, Y. The Intelligent Catalyst: Pd-Perovskite Having the Self-Regenerative Function in a Wide Temperature Range. *Key Eng. Mater.* (2006).
34. Taniguchi, M. *et al.* The self-regenerative Pd-, Rh-, and Pt-perovskite catalysts. in *Topics in Catalysis* (2007). doi:10.1007/s11244-007-0207-x
35. Taniguchi, M., Uenishi, M., Tan, I., Tanaka, H. & Kimura, M. Thermal Properties of the Intelligent Catalyst. (2004).
36. Tanaka, H. *et al.* Self-Regenerating Rh- and Pt-Based Perovskite Catalysts for Automotive-Emissions Control. *Angew. Chemie Int. Ed.* **45**, 5998–6002 (2006).
37. Hamada, I., Uozumi, A., Morikawa, Y., Yanase, A. & Katayama-Yoshida, H. A density functional theory study of self-regenerating catalysts LaFe1-xMxO3-y(M = Pd, Rh, Pt). *J. Am. Chem. Soc.* **133**, 18506–18509 (2011).
38. Tanaka, H. & Kaneko, K. Method for producing perovskite-type composite oxide. *US Pat. 7,381,394* (2008).
39. Katz, M. B. *et al.* Reversible precipitation/dissolution of precious-metal clusters in perovskite-based catalyst materials: Bulk versus surface re-dispersion. *J. Catal.* **293**, 145–148 (2012).
40. Malamis, S. A. *et al.* Comparison of precious metal doped and impregnated perovskite oxides for TWC application. *Catal. Today* **258**, 535–542 (2015).
41. Katz, M. Advanced Transmission Electron Microscopy Studies of Induced Interactions of Metallic Species with Perovskite Oxide Hosts. (2013).
42. Jarrige, I. *et al.* Toward optimizing the performance of self-regenerating Pt-based perovskite catalysts. *ACS Catal.* **5**, 1112–1118 (2015).
43. Hazen, R. M. Perovskites. *Scientific American* **258**, 74–81 (1988).
44. Keav, S., Matam, S., Ferri, D. & Weidenkaff, A. Structured Perovskite-Based Catalysts and Their Application as Three-Way Catalytic Converters—A Review.

Catalysts **4**, 226–255 (2014).
45. Tejuca, L. G., Fierro, J. L. G. & Tascón, J. M. D. Structure and Reactivity of Perovskite-Type Oxides. *Adv. Catal.* **36**, 237–328 (1989).
46. Neagu, D. Materials and Microstructures for High Temperature Electrochemical Devices through Control of Perovskite Defect Chemistry Dragos Neagu. 1–257 (2012).
47. Goldschmidt, V. M. Die gesetze der krystallochemie. (1926).
48. Peña, M. A. & and J. L. G. Fierro*. Chemical Structures and Performance of Perovskite Oxides. *Chem. Rev.* **101**, 1981–2018 (2001).
49. Chynoweth, A. G. {\it Ferroelectricity in crystals} by H. D. Megaw. *Acta Crystallogr.* **11**, 754–755 (1958).
50. Allan, N. L., Dayer, M. J., Kulp, D. T. & Mackrodt, W. C. Atomistic lattice simulations of the ternary fluorides AMF3(A = Li, Na, K, Rb, Cs; M = Mg, Ca, Sr, Ba). *J. Mater. Chem.* **1**, 1035–1039 (1991).
51. Neagu, D. & Irvine, J. T. S. *Perovskite Defect Chemistry as Exemplified by Strontium Titanate*. *Comprehensive Inorganic Chemistry II* (Elsevier Ltd., 2013). doi:10.1016/B978-0-08-097774-4.00421-6
52. Duprez, D. *et al.* Perovskites as Substitutes of Noble Metals for Heterogeneous Catalysis : Dream or Reality Se b. *Chem. Rev.* **114**, 10292 (2014).
53. Shannon, R. D. Revised effective ionic radii and systematic studies of interatomic distances in halides and chalcogenides. *Acta Crystallogr. Sect. A* **32**, 751–767 (1976).
54. Neagu, D., Tsekouras, G., Miller, D. & Ménard, H. In situ growth of nanoparticles through control of non-stoichiometry. *Nat. Chem.* (2013).
55. Neagu, D. & Irvine, J. T. S. Enhancing electronic conductivity in strontium titanates through correlated A and B-site doping. *Chem. Mater.* **23**, 1607–1617 (2011).
56. Oh, T., Rahani, E., Neagu, D. & Irvine, J. Evidence and Model for Strain-Driven Release of Metal Nanocatalysts from Perovskites during Exsolution. *J.* (2015).
57. Zhu, Y. *et al.* Promotion of oxygen reduction by exsolved silver nanoparticles on a perovskite scaffold for low-temperature solid oxide fuel cells. *Nano Lett.* (2015).
58. Liu, S., Chuang, K. & Luo, J. Double layered perovskite anode with in-situ exsolution of Co-Fe alloy to cogenerate ethylene and electricity in proton conducting ethane fuel cell. *ACS Catal.* (2015).
59. Tsvetkov, D., Ivanov, I. & Malyshkin, D. Oxygen content, cobalt oxide exsolution and defect structure of the double perovskite PrBaCo 2 O 6− δ. *J. Mater.* (2016).
60. Thalinger, R., Gocyla, M. & Heggen, M. Ni–perovskite interaction and its structural and catalytic consequences in methane steam reforming and methanation reactions. *J.* (2016).
61. Miller, E. Synthesis, Characterization, and Optimization of Novel Solid Oxide Fuel Cell Anodes. (2015).
62. Liu, S., Chuang, K. & Luo, J. Erratum to “Double Layered Perovskite Anode with in Situ Exsolution of Co–Fe Alloy To Cogenerate Ethylene and Electricity in Proton-Conducting Ethane Fuel Cell”. *ACS Catal.* (2016).
63. Armor, J. N. A history of industrial catalysis. *Catal. Today* **163**, 3–9 (2011).
64. Voorhoeve, R. J. H., Remeika, J. P. & Johnson, D. W. Rare-Earth Manganites: Catalysts with Low Ammonia Yield in the Reduction of Nitrogen Oxides. *Science (80-.).* **180**, 62–64 (1973).
65. Gallagher, P. K., Johnson, D. W. & Schrey, F. Studies of some supported perovskite oxidation catalysts. *Mater. Res. Bull.* **9**, 1345–1352 (1974).
66. Bravo-Suárez, J. J., Chaudhari, R. V & Subramaniam, B. Design of Heterogeneous

Catalysts for Fuels and Chemicals Processing: An Overview. in *Novel Materials for Catalysis and Fuels Processing* 3–68 doi:10.1021/bk-2013-1132.ch001
67. Misono, M. Catalysis of Perovskite and Related Mixed Oxides. *Stud. Surf. Sci. Catal.* **176**, 67–95 (2013).
68. Neagu, D., Oh, T., Miller, D., Ménard, H. & Bukhari, S. Nano-socketed nickel particles with enhanced coking resistance grown in situ by redox exsolution. *Nat. Commun.* (2015).
69. Xu, S. *et al.* Perovskite chromates cathode with resolved and anchored nickel nano-particles for direct high-temperature steam electrolysis. *J. Power Sources* (2014).
70. Tsekouras, G., Neagu, D. & Irvine, J. Step-change in high temperature steam electrolysis performance of perovskite oxide cathodes with exsolution of B-site dopants. *Energy Environ. Sci.* (2013).
71. Li, Y., Wang, Y., Doherty, W., Xie, K. & Wu, Y. Perovskite chromates cathode with exsolved iron nanoparticles for direct high-temperature steam electrolysis. (2013).
72. Sun, Y., Li, J., Zeng, Y., Amirkhiz, B. & Wang, M. A-site deficient perovskite: the parent for in situ exsolution of highly active, regenerable nano-particles as SOFC anodes. *J. Mater.* (2015).
73. Prabha, I. Current Status of Platinum Based Nanoparticles : Physicochemical Properties and Selected Applications – A Review. 122–133 (2019).
74. Da, Y. *et al.* Catalytic oxidation of diesel soot particulates over Pt substituted LaMn 1-x Pt x O 3 perovskite oxides. *Catal. Today* **327**, 73–80 (2019).
75. Li, X. *et al.* In situ exsolution of PdO nanoparticles from non-stoichiometric LaFePd0.05O3+Δ electrode for impedancemetric NO2 sensor. *Sensors Actuators, B Chem.* **298**, (2019).
76. Gao, Y. *et al.* Energetics of Nanoparticle Exsolution from Perovskite Oxides. *J. Phys. Chem. Lett.* **9**, 3772–3778 (2018).
77. Fang, C. *et al.* Highly Dispersed Pt Species with Excellent Stability and Catalytic Performance by Reducing a Perovskite-Type Oxide Precursor for CO Oxidation. *Trans. Tianjin Univ.* **24**, 547–554 (2018).
78. Fierro, J. L. G. Chemical Structures and Performance of Perovskite Oxides. (2017).
79. Zhang, S. In-situ and Ex-situ Microscopy and Spectroscopy Study of Catalytic Materials by. 217 (2017).
80. Glazer, A. M. The classification of tilted octahedra in perovskites. *Acta Crystallogr. Sect. B* **28**, 3384–3392 (1972).
81. Howard, C. J. & Stokes, H. T. Group-Theoretical Analysis of Octahedral Tilting in Perovskites. *Acta Crystallogr. Sect. B* **54**, 782–789 (1998).
82. Neagu, D., Tsekouras, G., Miller, D. D. N., Ménard, H. & Irvine, J. T. S. In situ growth of nanoparticles through control of non-stoichiometry. *Nat. Chem.* **5**, 916–923 (2013).
83. G. ROUSSEAU. No Title. *Acad. Sci. Paris* **109**, 144 (1889).
84. Statton, W. O. The phase diagram of the BaO-TiO2system. *J. Chem. Phys.* **19**, 33–40 (1951).
85. Randall, J. J. & Ward, R. The Preparation of Some Ternary Oxides of the Platinum Metals. *J. Am. Chem. Soc.* **81**, 2629–2631 (1959).
86. Haradem, P. S., Chamberland, B. L., Katz, L. & Gleizes, A. A structural model for barium platinum oxide, Ba3Pt2O7. *J. Solid State Chem.* **21**, 217–223 (1977).
87. Chaston, J. C. Reactions of Oxygen with the Platinum Metals; II-OXIDATION OF RUTHENIUM, RHODIUM, IRIDIUM AND OSMIUM. *Platin. Met. Rev.* **9**, 51–56

(1965).
88. Sharma, P. A., Brown-Shaklee, H. J. & Ihlefeld, J. F. Oxygen partial pressure dependence of thermoelectric power factor in polycrystalline n-type SrTiO3: Consequences for long term stability in thermoelectric oxides. *Appl. Phys. Lett.* **110**, (2017).
89. Kuklja, M. M., Mastrikov, Y. A., Jansang, B. & Kotomin, E. A. The intrinsic defects, disordering, and structural stability of Ba xSr 1-xCo yFe 1-yO 3-δ perovskite solid solutions. *J. Phys. Chem. C* **116**, 18605–18611 (2012).
90. Nur, A. S. M. *et al.* Phase-Dependent Formation of Coherent Interface Structure between PtO2 and TiO2 and Its Impact on Thermal Decomposition Behavior. *J. Phys. Chem. C* **122**, 662–669 (2018).

CHAPTER 5 OXIDATION AND CATALYSIS

5.1 Oxidation chemistry and catalysis

Automotive catalysis

In this chapter, we will explore the role of Pt/LCT and Pt/LST as an alternative catalyst for prospective commercial applications in the automotive sphere. The lab scale tests were carried out between St Andrews University and Johnson Matthey (Sonning Common). Between the two, it was possible to gain insight into the characteristics of the nature of the materials as prospective catalysts.

The methodology taken for each material prepared was one of screening first, followed by an in-depth study of the microstructure and nanoparticle characteristics, followed by catalysis reactions.

Here we will discuss the four major studies (1-4) carried out and, briefly, two further studies (5 & 6):

1: CO oxidation (St Andrews)

2:CO:NO 1:1 ratio (JM Sonning)

3: NH_3 oxidation (JM Sonning)

4: Diesel oxidation (JM Sonning)

5: Simulated Diesel oxidation real conditions particle study (JM Sonning)

6: DRIFT In-situ CO oxidation particle study (St Andrews)

CO oxidation

CO oxidation is a simple pre-screening catalytic mechanism in order to check the suitability of catalytically active materials. A CO oxidation rig was built in St Andrews to schematic Figure 5-1 in order to assess the activity of the materials prepared.

$$CO + 0.5(O_2) \rightarrow CO_2$$

Or

$$2CO + O_2 \rightarrow 2CO_2$$

Conversion of CO was calculated as follows:

$$X_{CO} = [CO]_{in}\text{vol.}\% - [CO]_{out}\text{vol.}\% / CO]_{in}\text{vol.}\%$$

$$R_{CO} = N_{CO} \times X_{CO} / W_{CAT}$$

Whereby [CO] in and out are the volume % of inlet and outlet gas through the catalyst bed. X_{CO} is used to calculate the reaction rate R_{CO}, where N_{CO} is the number of mol s^{-1} and W_{CAT} is the catalyst weight in grams. R_{CO} is the reaction rate in $mol_{CO}\ g_{cat}^{-1}\ s^{-1}$.

CO oxidation reaction conditions

- CO: 2%, O_2: 20% (CO: O_2 = 1: 10)
    - Carrier: N_2
- Total Flow: 200 ml/min
- Catalyst: 0.2 ml (around 0.25 g), 20-40 mesh (850-425 μm)
- GHSV: 60,000 /hr
- Temp: 50-250 °C
- Reduction before the test: 300 °C at 5% H_2/Ar

GC conditions

- Column: Molsieve 5A + Haysep
- Oven: 60 °C, constant
- Carrier: Ar, 10 ml/min
- Injector: 110 °C
- TCD detector, 180 °C
- Analysis time: 10 min

Catalytic performance of all samples was initially tested for CO oxidation in Figure 5-2a at lab-scale conditions. Non-doped perovskite demonstrated almost no catalytic activity, while an increased activity was observed after Pt incorporation prior to reduction. As expected, a very significant increase in catalytic performance was obtained after the emergence of the Pt NPs in both samples. While perovskites with Ca or Sr showed a difference in catalytic activity due to the difference in Pt NP morphology and distribution, **Pt+LCT** exhibited a superior performance with a light-off curve at 190 ^{o}C for 100 % CO conversion at low Pt loading of 0.5 wt.%, compared to impregnated **Pt/LCT** (240 ^{o}C). Remarkably, the activity was even higher than the commercial type **Pt/γ-Al_2O_3** (220 ^{o}C) increasing more than 20% in CO oxidation activity, despite a low surface area (1-2 m^2/g) compared to **Pt/γ-Al_2O_3** (112.7 m^2/g) as in Figure 5-4f. Another interesting result was that Pt+LCT also showed great oxidation activity in a partial O_2 environment (Fig. 5-3), maintaining activity with 50% of partial O_2 and outperforming **Pt/Al_2O_3** at 1:1 (CO:O_2).

XPS O 1s (Fig. 5-3a,b) showed that the perovskite surface possesses a large portion of active oxygen (O_D+O_C) species,[4, 22] resulting in oxygen sites that are involved more in oxidation reactions rather than O_L. These were further increased, especially O_D through the Pt emergence. These observations confirm an efficient oxidation mechanism at the uniquely active Pt species and the possession of active oxygens that are important factors for outstanding catalytic performance.

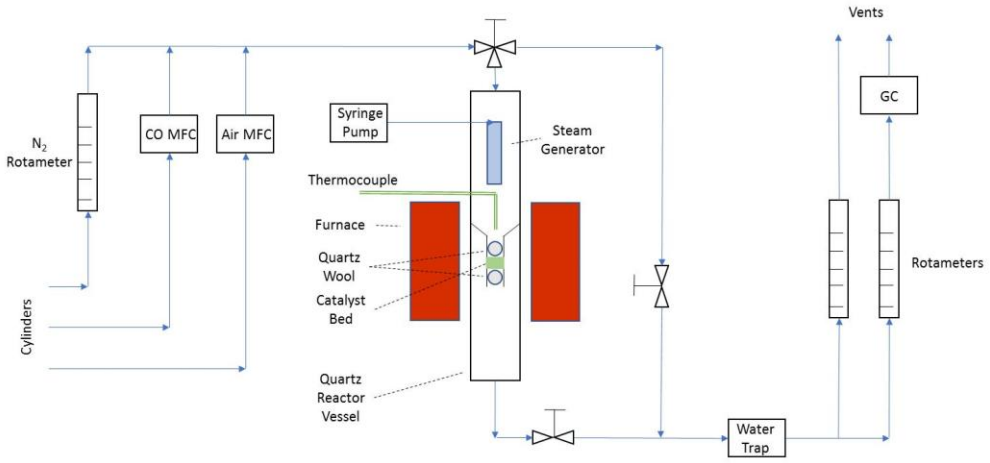

Figure 5-1 shows the schematic of the CO oxidation rig built in St Andrews.

a

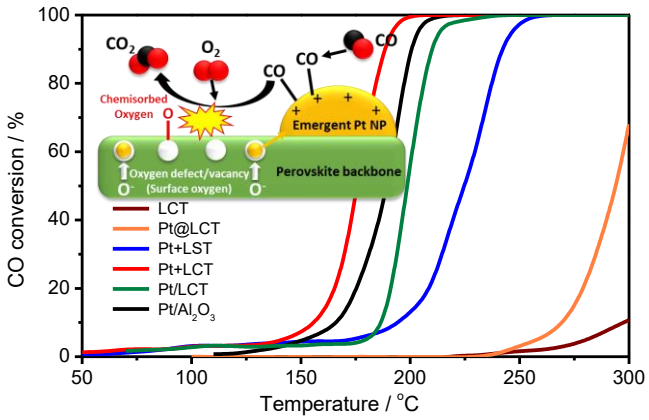

b

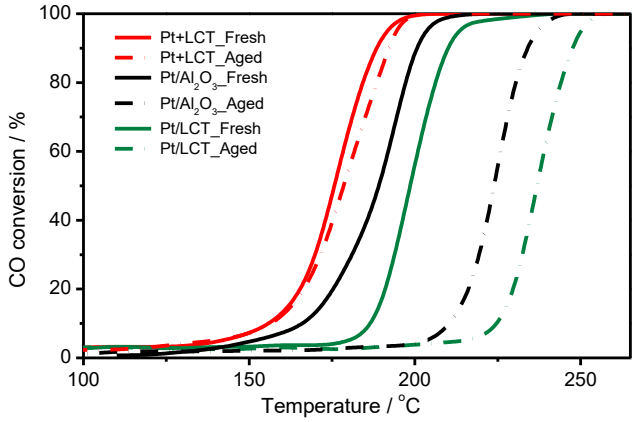

c

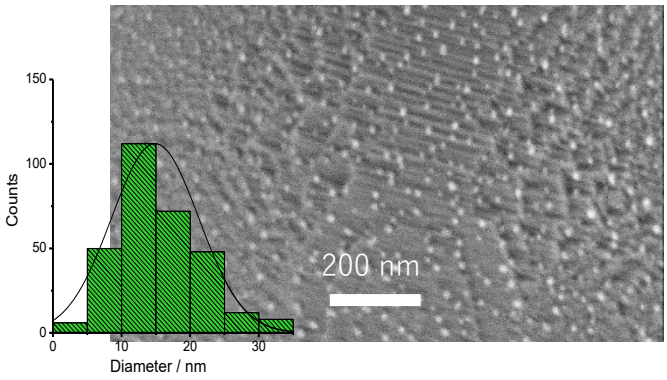

Figure 5-2: Catalytic functionality on CO oxidation of the perovskite catalysts with emergent Pt NPs. (a) Light-off curves for initial CO oxidation by a feed mixture gas of 20,000 ppm CO, 10.0 vol.% O_2 from air (21% O_2 and 79% N_2) at N_2 balance with a total gas flow rate of 200 ml/min (GHSV=60,000/hr) on the prepared samples (inset: reaction mechanism of **Pt+LCT**); (b) Light-off curves for CO oxidation before and after and in-situ aging at 800 °C under an air gas flow of 50 ml/min for over 2 weeks (350

hrs) for emergent **Pt+LCT**, infiltrated **Pt/LCT** and **Pt/γ-Al_2O_3**; (c) SEM image with the Pt NPs distribution after the 350-hour aging test of **Pt+LCT**.

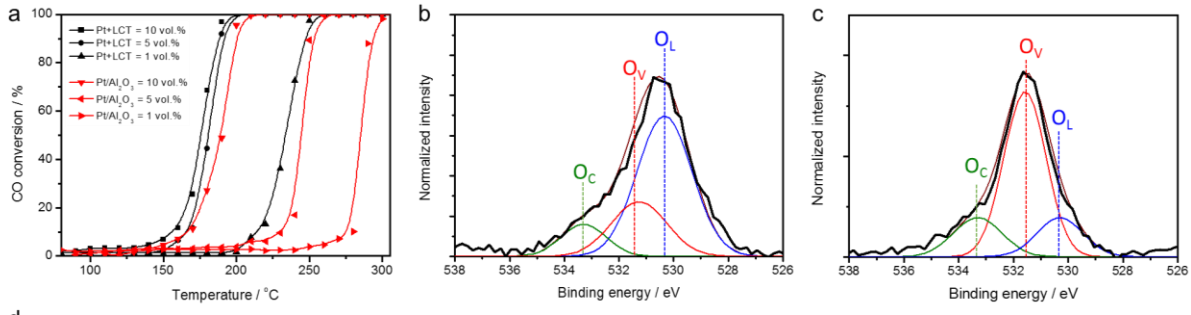

d

		Binding Energy (eV) and relative percentages in parentheses (%)			
		$O_L(O^{2-})$	$O_D(O^-)$	$O_C(O^-)$	$(O_D+O_C)/O_L$
Pt@LCT	eV	530.329	531.262	533.289	0.58
	%	63.36	28.89	11.75	
Pt+LCT	eV	530.306	531.58	533.305	4.86
	%	17.08	64.96	17.96	

Figure 5-3. Oxygen partial pressure effect. (a) Light-off curves for CO oxidation at various oxygen partial pressures by a feed mixture gas of 20,000 ppm CO, 10.0 vol.% O_2 from air (21% O_2 and 79% N_2) at N_2 balance with a total gas flow rate of 200 ml/min (GHSV=60,000/hr) on the samples of Pt@LCT and Pt/γ-Al_2O_3. The reactivity of Pt/γ-Al_2O_3 largely decreases at lower O_2 content, which is a normal phenomenon. XPS O 1s spectra of (b) Pt@LCT and (c) Pt+LCT after emergence process at 700 °C with the heating and cooling rates of 5 °C·min^{-1} under continuous flow of 5% H_2/Ar (20 ml·min^{-1}). (d) summarized table for binding energies (eV) and relative percentages for each oxygen species on the surface and the calculated $(O_D+O_C)/O_L$ ratio for Pt@LCT before and after the emergence process (O_L: lattice oxygen, O_D: defects or surface oxygen, and O_C: chemisorbed oxygen species on the surface).[4,21]

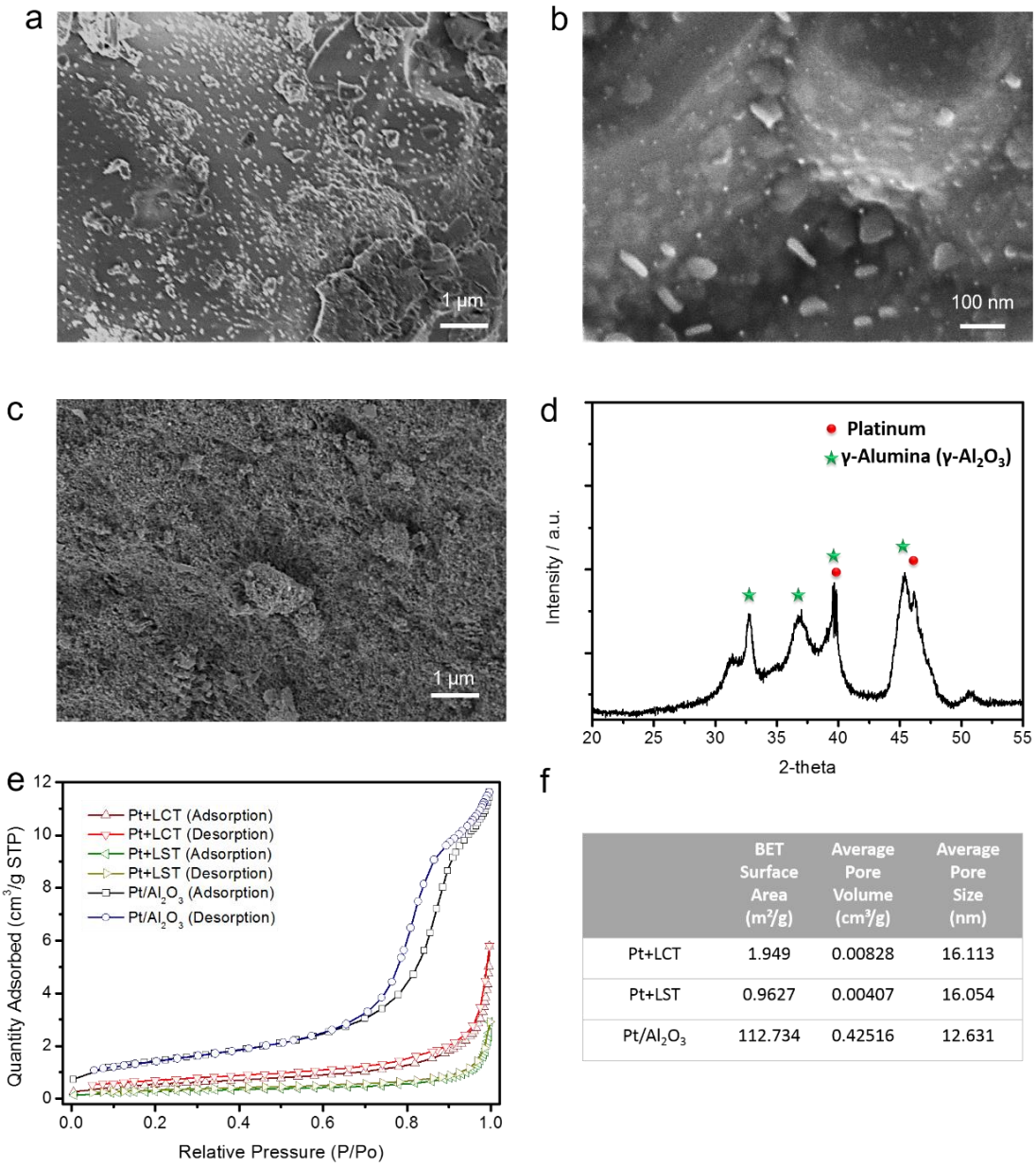

	BET Surface Area (m^2/g)	Average Pore Volume (cm^3/g)	Average Pore Size (nm)
Pt+LCT	1.949	0.00828	16.113
Pt+LST	0.9627	0.00407	16.054
Pt/Al_2O_3	112.734	0.42516	12.631

Figure 5-3: (a-b) SEM images for the Pt/LCT. (c) SEM image and (d) X-ray diffraction pattern for Pt/γ-Al_2O_3, as well as the (e) N_2-adsorption/desorption analysis with (f) the summarized Table of Pt+LCT and (b) Pt+LST perovskites comparing with the Pt/γ-Al_2O_3 catalyst.

CO:NO 1:1 oxidation

CO:NO 1:1 reaction was undertaken at Sonning Common (Johnson Matthey) in one of the test rigs (SCAT 3). The reduction of CO and NO over a perovskite has previously been studied (over perovskite)[1] materials and specifically in relation to the kinetic ability of the perovskite surface itself. NO is thermodynamically driven and is kinetically unstable for decomposition in the presence of catalysts. Although Pd is typically used for this catalytic process, Pt was screened in order to test its effectiveness. Although the reduction of CO and NO is typically undertaken with noble metals, perovskite-type oxides are known effective stable oxide catalysts.

$$2NO + CO \rightarrow N_2O \ (300\text{-}400°C)$$

$$2NO + 2CO \rightarrow 2CO_2 + N_2 \ (500\text{-}700°C)$$

CO:NO 1:1 oxidation conditions

- CO:NO is often
- CO 4000ppm, NO 4000ppm
- Carrier: N_2 balance
- Total Flow: 12L/min
- Catalyst: 0.2g with 0.2g of cordurite
- Temp: 90-500 °C

$$2NO + CO \rightarrow N_2O \ (300\text{-}400°C)$$

$$2NO + 2CO \rightarrow 2CO_2 + N_2 \ (500\text{-}700°C)$$

Results of the NO reduction reaction by CO were collected at feed streams of CO+NO with comparable stoichiometric conditions and gas hourly space velocity (GHSV) to that observed in simulated car exhausts. It was seen that the developed catalyst has great reducibility from the NO conversion by the presence of CO, as illustrated in Figure 5-4. Even under high GHSV conditions, the CO reduction activity of the materials followed the same trend on the light-off plots as those observed at the initial CO oxidation tests due to the oxygen storage property (Fig. 5-2a.). Interestingly, the NO conversion also reached a relatively high value of over 80% at 450 ºC for **Pt+LCT** comparing to **Pt/LCT** (35 %) and **Pt/γ-Al_2O_3** (63 %), which can provide a possible reaction model (Fig. 5-4) due to highly distributed active Pt NPs and oxygen atoms provided by the mixed oxide surface and monolayered Titanium oxide on the perovskite surfaces.

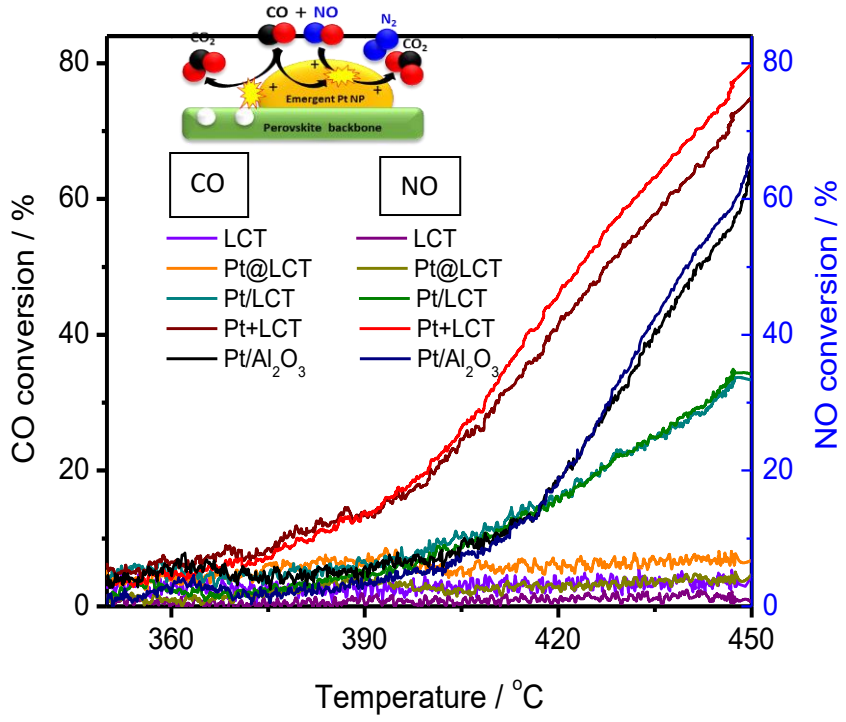

Figure 5-4: reaction mechanism of **Pt+LCT** and results at the coexistence of 4,000 ppm CO and 4,000 ppm NO at stoichiometric conditions in feed streams and an GHSV level of real car exhausts, calculated from the raw data in Figure 5-5.

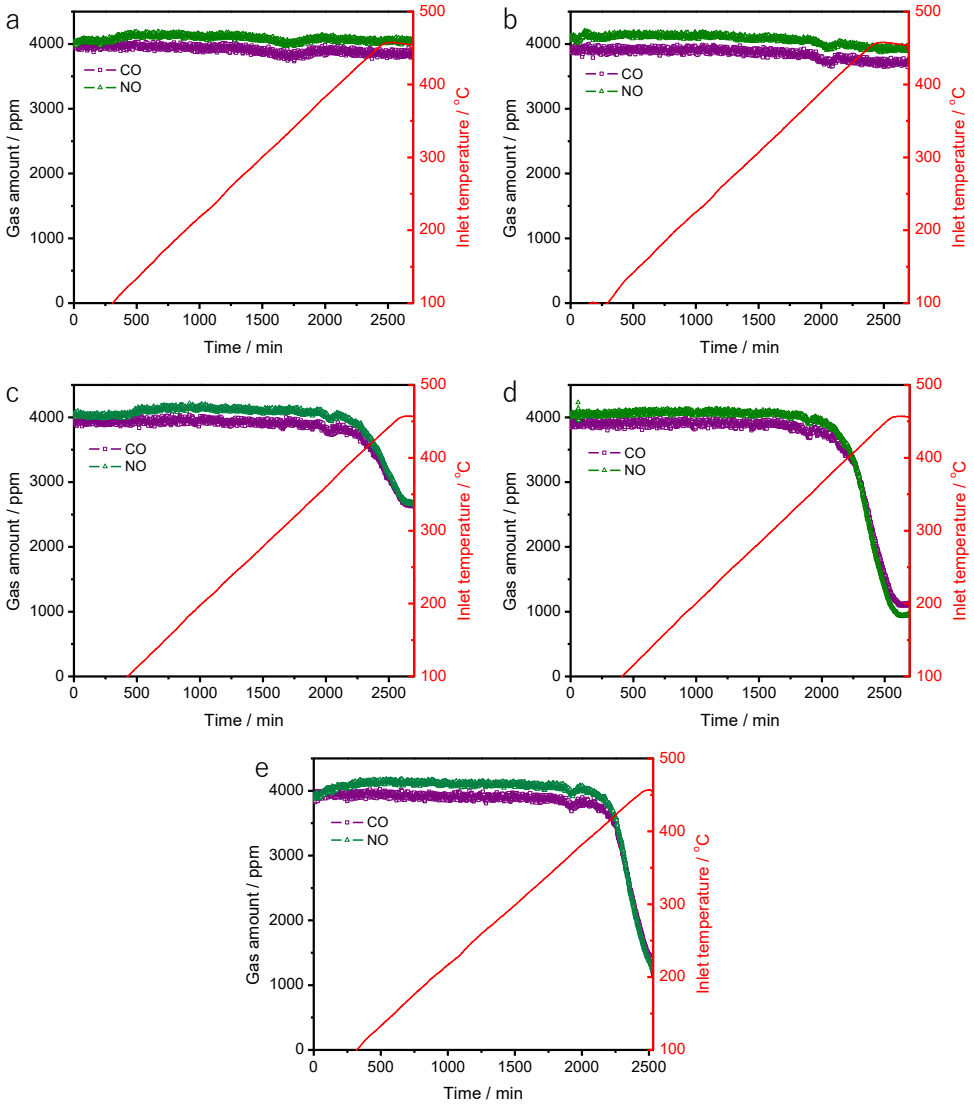

Figure 5-5: Catalyst tests of CO+NO reaction in simulated car exhaust environments. Each reactant amounts (ppm) for (a) **LCT**, (b) **Pt@LCT**, (c) **Pt/LCT**, (d) **Pt+LCT** and (e) **Pt/γ-Al_2O_3** over the time and reaction temperature.

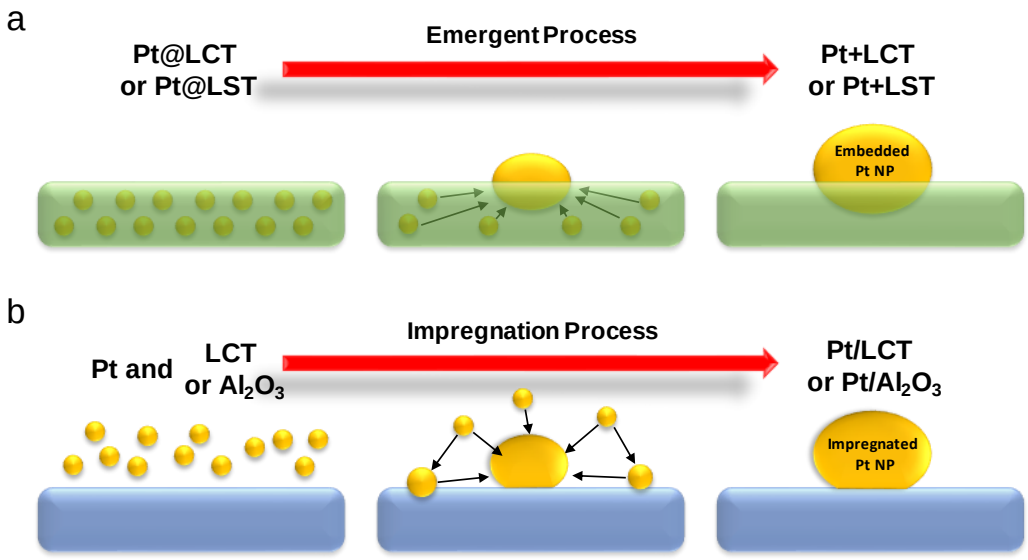

Figure 5-5a shows the revised scheme and illustrates the 2 major differences between Pt@LCT, and Pt+LCT. The emergent process is the reduction step.

Figure 5-5b shows the process of reduction for impregnated Pt/LCT and reference Pt/Al_2O_3 catalysts where by the Pt nano particles are not fully embedded within the support and rely upon a monolayer based interaction of Pt with the support. The impregnation process here refers to the reduction step necessary in forming nano particles.

NH_3 oxidation

Typically, modern diesel vehicles with a large engine size (medium-sized family vehicles and above) use NH_3 in order to catalyse NO_x. This poses a novel problem in the automotive industry whereby excess NH_3 that is not catalysed over a Cu-chabazite zeolite[2] is emitted into the environment, posing a far greater pollution risk than NO_x itself. In order to mitigate this, a NO_x slip catalyst is fitted to the back of the emissions process, which is usually $Pt\text{-}Al_2O_3$.

NH_3 oxidation reaction conditions

- NH_3 550ppm, CO 220ppm, 4.5% CO_2, 10% O_2 5%H_2O (steam)
- Carrier: N_2 balance
- Total Flow: 12L/min
- Catalyst: 0.2g with 0.2g of cordurite
- MKS MG2000 multi-gas analyser using a FT-IR detector
- Temp: 150-330 °C

In the case of ammonia slip, there is an automotive industrial problem whereby the non-catalyzed NH_3 is emitted into the atmosphere after NH_3 is sprayed onto a Cu-chabazite zeolite. In order to mitigate the excess NH_3, currently 0.5-1% **Pt/γ-Al_2O_3** catalysts are used for AMOX. As seen in Figure 4c, **Pt+LCT** shows a lower temperature (230 ^oC) for 100% NH_3 oxidation compared to **Pt/γ-Al_2O_3** (245 ^oC), where the multiple oxidation has also taken place with a 100% CO conversion. These both confirm the significant catalytic ability of the **Pt+LCT** catalyst on multiple oxidations for not only light gases like CO and NO, but also harmful hydrocarbons and even excess NH_3.

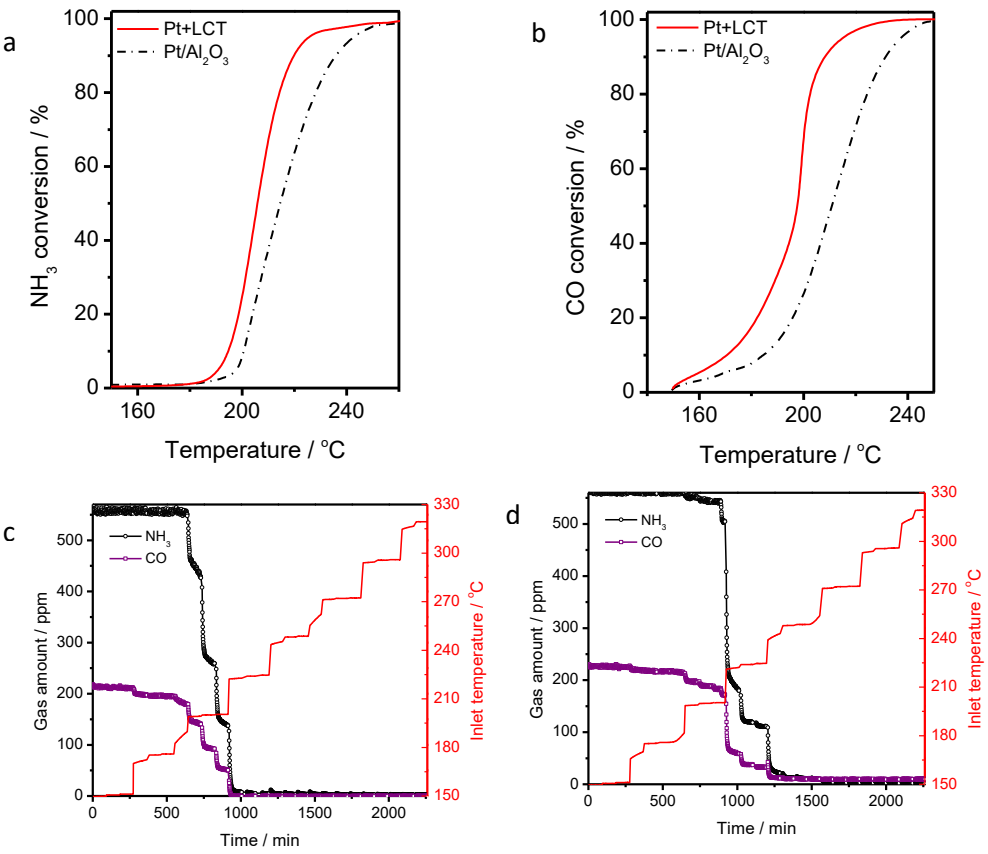

Figure 5-6: AMOX (coexistence of NH_3 and CO in feed streams) test results of each reactants in the presence of O_2 (10%), H_2O (5%) and CO_2 (4.5%) for emergent **Pt+LCT** and **Pt/γ-Al_2O_3**, converted from the raw data in Fig. 5-7

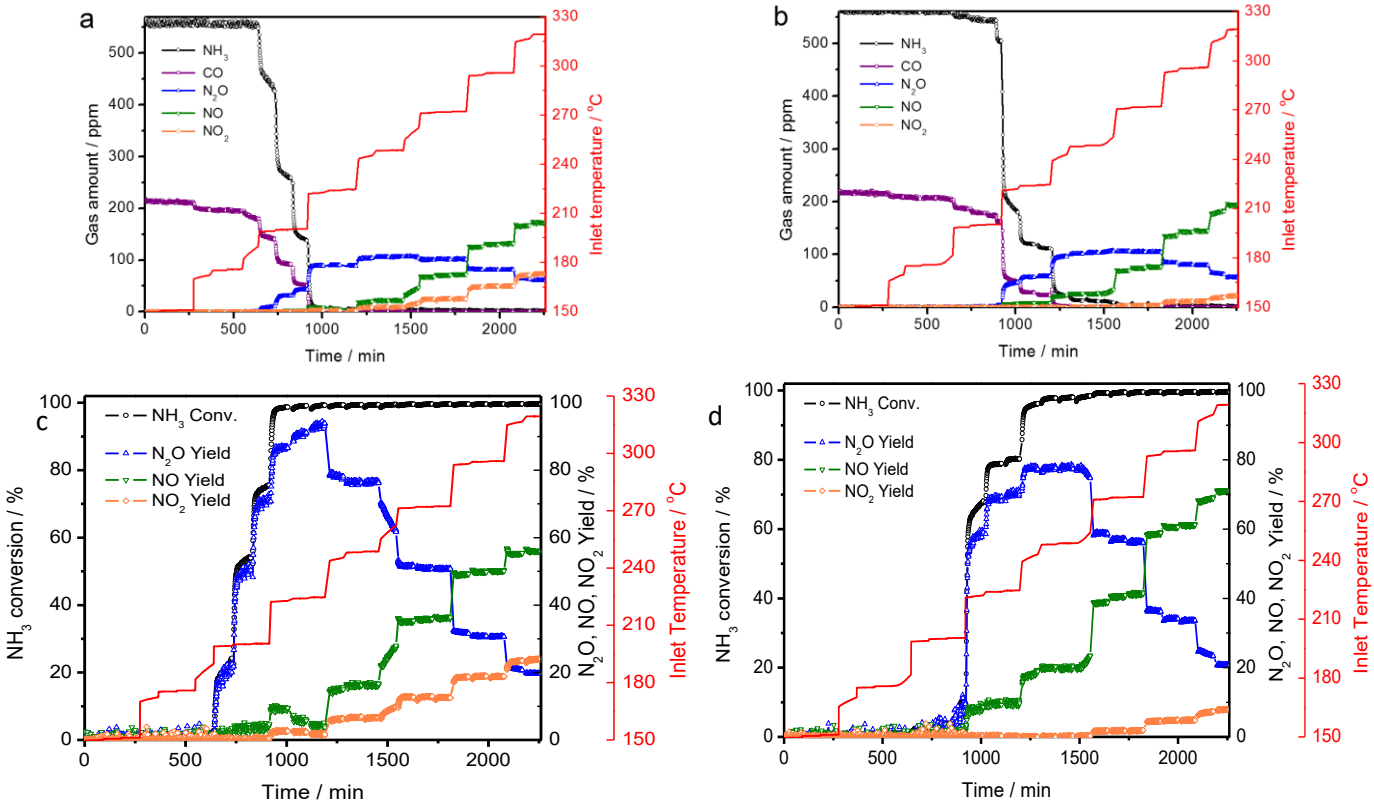

Figure 5-7: **Pt+LCT** (a and c) and **Pt/γ-Al_2O_3** (b and d) raw data for steady state transient reaction.

Each step is a temperature hold, indicating adsorption on the surface of the perovskite of CO and NH_3.

Diesel oxidation catalysis

Diesel oxidation catalysis are used in three major reactions: the catalysis of long chained hydrocarbons like propylene, CO and NO. The formation of NO_2 can sometimes be undesirable for exhaust to the environment, although N_2O is also favourable in further reactions such as the regeneration of DPFs and in helping with SCR reactions.

DOC:

$$CnH_2m + (n + ½\ m)\ O_2 \rightarrow nCO_2 + mH_2O$$

$$CO + ½O_2 \rightarrow CO_2$$

$$NO + ½\ 2O_2 \rightarrow NO_2$$

Diesel oxidation conditions

- C_3H_6 200ppm, NO 300ppm, CO 1500ppm, 4.5% CO_2, 10% O_2 5%H_2O (steam)
- Carrier: N_2 balance
- Total Flow: 12L/min
- Catalyst: 0.2g with 0.2g of cordurite
- MKS MG2000 multi-gas analyser using a FT-IR detector
- Temp: 150-330 °C

DOCs are functioned to oxidize the exhaust gases to harmless products, as well as NO to support the performance of diesel particulate filters and SCR catalysts. From Figure 5-8, we can see that **Pt+LCT** shows a strong ability in catalysing propylene (C_3H_6) at low temperature (260 ^oC) while simultaneously, multiple oxidations including CO and NO are observed. The coexistence of the feed gases marginally lowered the NO conversion, suggesting that CO and C_3H_6 oxidations take place preferentially. However, when we compare each reactant to **Pt/γ-Al_2O_3**, all the results were outperformed, with at least 20% in each conversion.

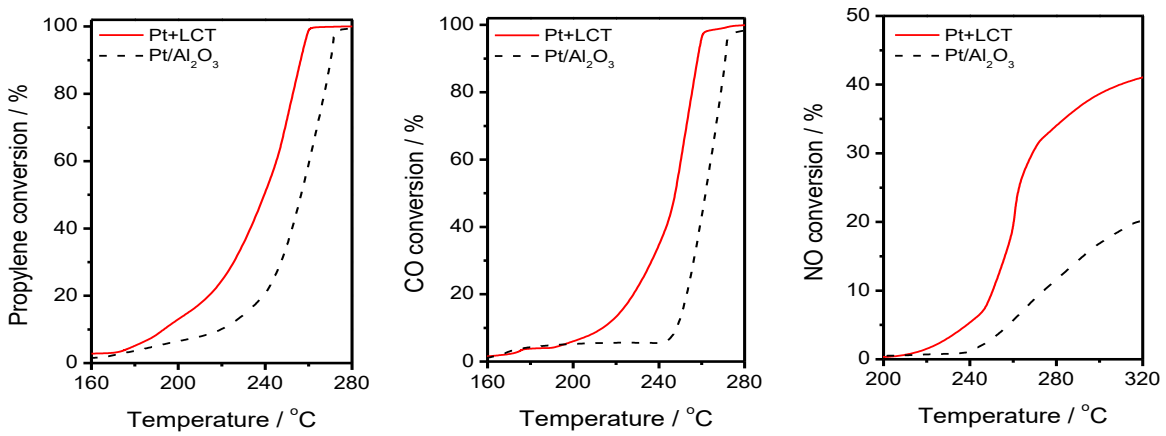

Figure 5-8: DOC (coexistence of C_3H_6 and CO+NO in feed streams) % conversion for propylene, CO and NO.

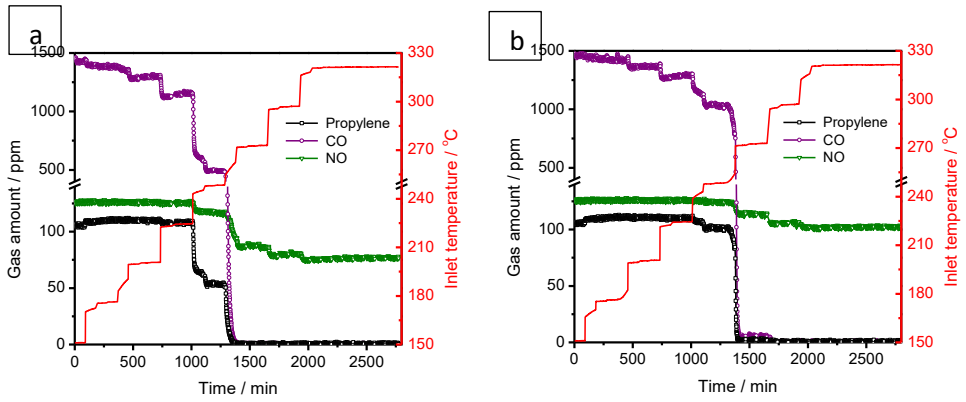

Figure 5-9 shows selected data for steady state transient reaction for DOC. Figure 5-9a shows Pt+LCT and 5-9b shows Pt/γ-Al_2O_3.

CO oxidation of Pt+LCT prepared at different temperatures with varying Pt nanoparticle size

Initial characterisation and CO screening indicated that Pt+LCT (700°C) showed the best catalytic activity in comparison to that of 0.5 wt.% Pt/γ-Al_2O_3 . In order to determine the effect of Pt nanoparticle size, CO oxidation catalysis testing was carried out on a range of particle sizes from reduction at 500-800°C, with a particle range from 4-20nm in size.

CO oxidation reaction conditions

- CO: 2%, O_2: 20% (CO: O_2 = 1: 10)
- Carrier: N_2
- Total Flow: 200 ml/min
- Catalyst: 0.2 ml (around 0.25 g), 20-40 mesh (850-425 μm)
- GHSV: 60,000 /hr
- Temp: 50-250 °C
- Reduction before the test: 300 °C at 5% H_2/Ar

GC conditions

- Column: Molsieve 5A + Haysep
- Oven: 60 °C, constant
- Carrier: Ar, 10 ml/min
- Injector: 110 °C
- TCD detector, 180 °C
- Analysis time: 10 min

In the case of CO oxidation in relation to the emerged platinum nanoparticle size, Pt+LCT 700°C > 0.5 wt.% Pt/γ-Al_2O_3 > Pt+LCT 800°C/ Pt+LCT 600°C > Pt+LCT 500°C > LCT non emerged.

The particle size directly relates to the rate of reaction and the ability for CO to oxidise over the Pt surface area. The combined ability of the perovskite surface and Pt nanoparticles amounts to a trend that would not otherwise be seen in typical autocatalysis substrates[3]. The dependence on the

nanoparticle in this case is not wholly upon a size of less than 10nm, rather, it is the combined effect of the nanoparticle and the perovskite surface chemistry. At 700°C, Pt +LCT shows advantageous catalytic ability even over commercial 0.5wt% Pt/γ-Al_2O_3.

Pt+LCT 700°C has an average size of 12-20 nm, as seen in Table 4-1. Interestingly, LBT shows some remedial activity above 250°C, indicating some activity of the perovskite itself without the active metal.

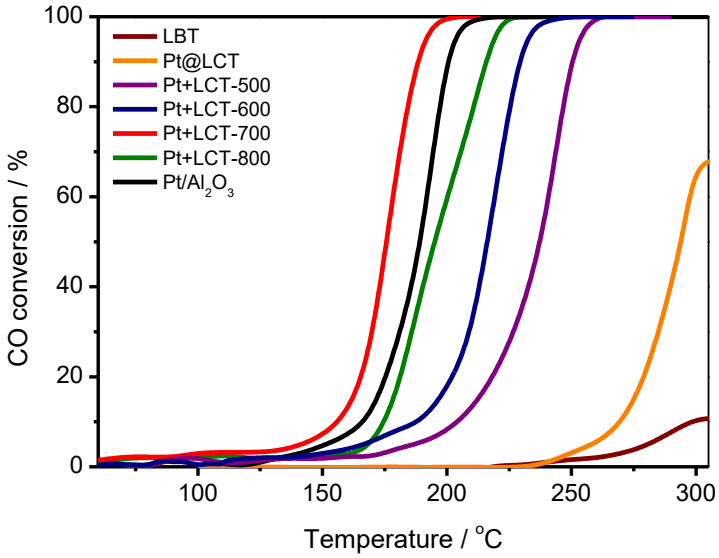

Figure 5-9 shows the light off curves for various samples recued at varying temperatures in 5%H_2Ar for 12 hours.

DOC of Pt+LCT prepared at different temperatures with varying Pt nanoparticle size

Real exhaust conditions were simulated in the SCAT 3 rig at JM (Sonning) for the diesel oxidation condition, including the addition of decane, which is a known perovskite surface deactivator.

Diesel oxidation reaction conditions

- 20000ppm in total: CO 1550ppm, H_2O 5%, CO_2 5%, NO 160 ppm, CH_4 40ppm, propylene C_3H_6 40ppm, Toluene C_7H_8 20ppm, Decane $C_{10}H_{22}$ 30ppm

- Carrier: N_2

- Total Flow: 15L/min

- Catalyst: 0.22g, 20-40 mesh (850-425 μm) 0.75g of cordurite

- Temp: 100-500 °C

Ageing-industrial oxidation ager (JM)

Realistic DOC conditions were carried out at JM (Sonning) on various Pt-LCT samples reduced in a temperature range from 500-900°C, as well as fresh and aged samples. Each sample was rapidly aged in an industrial ager. Ageing occurred in an oxidising environment.

Interestingly, Pt+LCT both before and after aging displayed little change in the activity of the catalyst for CO oxidation (in the DOC reaction) for all samples. Decane (C10) has an adverse affect on the surface chemistry of the perovskite, preventing rapid catalysis and conversion. As there was little change after ageing for all samples prepared at different temperatures, ageing has little effect on the catalytic activity of Pt+LCT (Figure 5-10).

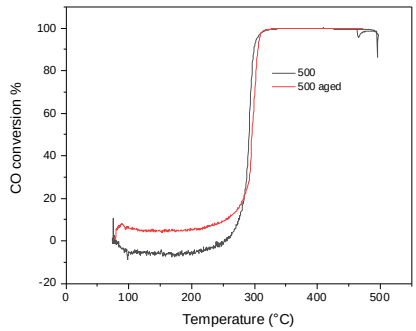

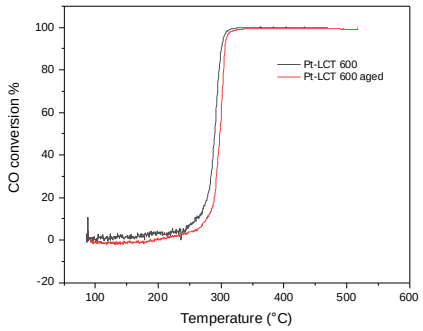
CO conversion %
Temperature (°C)
Pt-LCT 600
Pt-LCT 600 aged

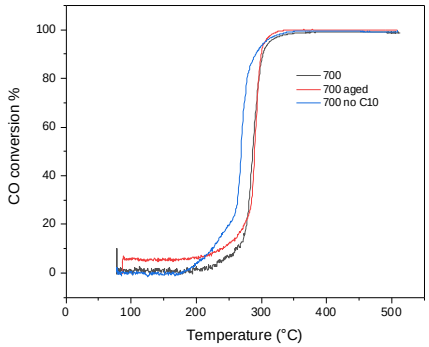
CO conversion %
Temperature (°C)
700
700 aged
700 no C10

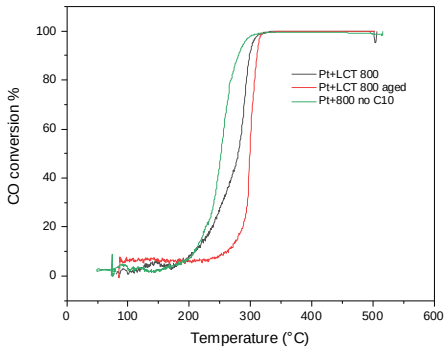
CO conversion %
Temperature (°C)
Pt+LCT 800
Pt+LCT 800 aged
Pt+800 no C10

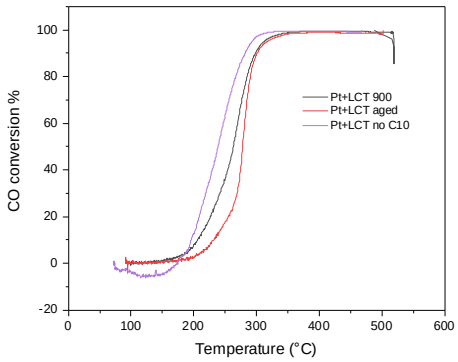

Figure 5-10 shows the catalytic activity of Pt+LCT reduced in 5%H_2/Ar at various temperatures both before and after ageing.

Overall, Pt+LCT 700 had the best activity, whilst still being affected by decane (Figure 5-11). The lack of decane, however, does mean that $C_{10}H_{22}$ has a surface chemical effect on the active sites, preventing activity of CO (Figure 5-11).

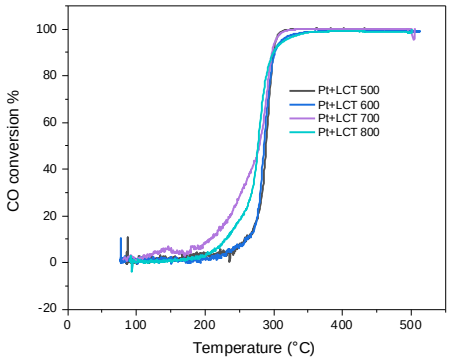

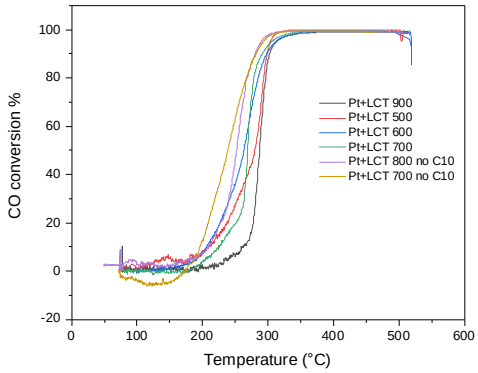

Figure 5-11 shows the CO conversion of Pt+LCT reduced at various temperatures. With both the full gas mix and without decane.

In comparison to commercial 0.5% wt.Pt-Al_2O_3 prepared by JM and conventional Pt-Al_2O_3 prepared at St Andrews, there was little difference in activity, further validating previous catalysis results that may put the conventionally made catalyst into dispute. However, after ageing, a large shift over 50°C can be seen with a higher light-off temperature for CO conversion (Figure 5-12). Although in this test reaction, 0.5wt.%Pt-Al_2O_3 displayed better catalytic properties, this can be attributed to the more complex gas feed mix and its affect on the surface chemistry of the perovskite.

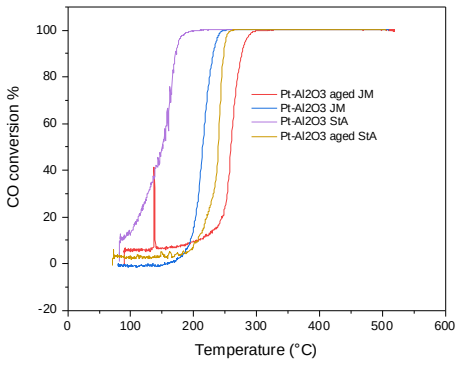

Figure 5-12 shows Pt-Al_2O_3 prepared at St Andrews and at JM. Both fresh and aged.

Total NO_x conversion (Figure 5-13) for Pt+LCT samples as prepared are low and follow the NO_2 equilibrium, the conversion of NO_x for as prepared Pt+LCT samples is inhibited by decane. NO_x conversion improves dramatically after ageing for Pt+LCT samples and especially for Pt+LCT 700°C

aged, which has a lesser light-off temperature than Pt-Al_2O_3. As expected, fresh Pt-Al_2O_3 has good NO_x conversion, but in contrast to aged Pt-LCT, the catalytic activity decreases upon ageing.

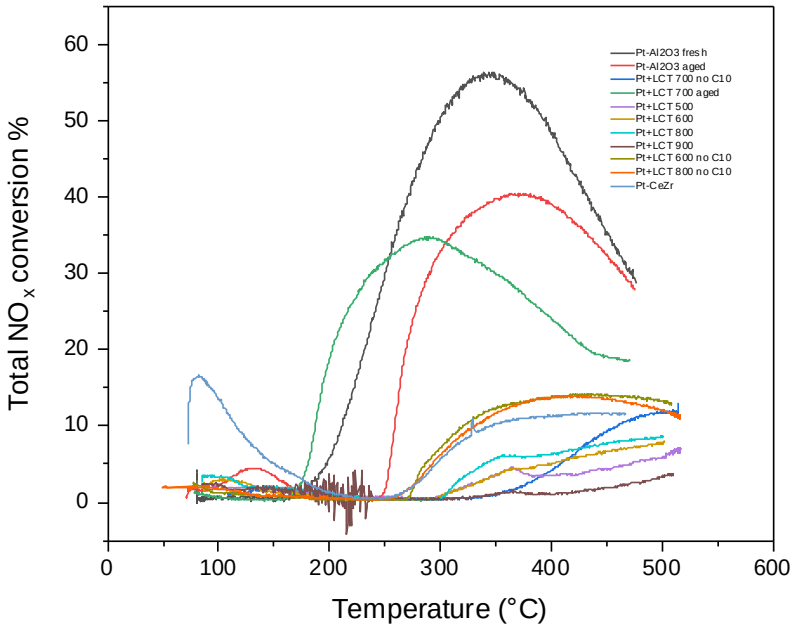

Figure 5-13 shows the total NO_x conversion for a range of reduced and fresh samples including Pt-Al_2O_3 standards, Pt+LCT reduced at various temperatures with and without decane.

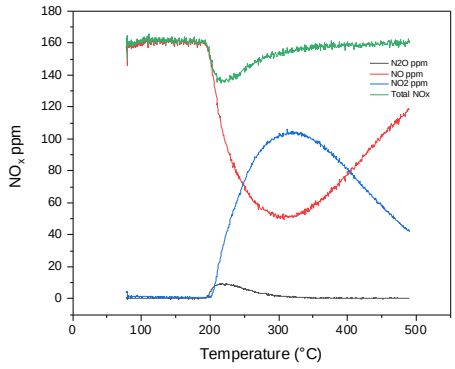

Figure 5-14 shows the total NO_x conversion in PPM for Pt+LCT at 700°C.

Interestingly, as NO_x conversion increases after aging for the perovskite catalyst and decreases for Pt-Al_2O_3, that is a strong indicator for SMSI interactions between the perovskite surface and the metallic Pt nanoparticles decoration, as well as a novel catalytic mechanism. Figure 5-14 shows the NO_x conversion in PPM for Pt+LCT 700°C. Here, more NO is formed after 400°C, which is more advantageous for the environment than N_2O, and there is also strong evidence of NO_x storage on the perovskite itself, as the release of NO_x trend is usually over 300°C. LBT (the perovskite without the active metal) has some catalytic activity, which indicates a dual purpose of the material (Figure 5-15).

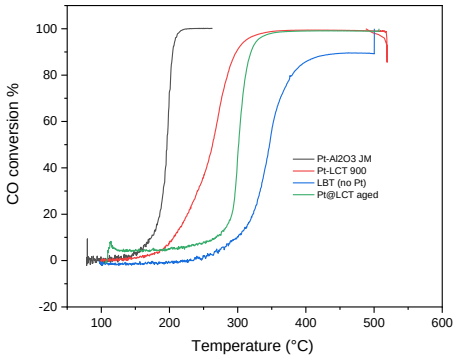

Figure 5-15 shows the difference between active metal Pt containing perovksite (Pt+LCT) and the pervoskite without active Pt metal showing catalytic activity at a higher temeprature over 400°C.

Table 5-1. Ageing conditions

Aging-1	Static ager (University of St Andrews) As seen in figure 3
H_2O	5 %
AIR	95%
Ramp rate	10 °C/min
Max. Temp.	800 °C

Aging-1	Static ager (Johnson Matthey)
H_2O	10 %
AIR	90%
Ramp rate	10 °C/min
Max. Temp.	800 °C

Aging-2	TWC hydrothermal redox ager (Johnson Matthey)	
	Base mix	+ perturbation line
Time	5 min	5 min
NO	0.1 %	
H_2O	10 %	
CO	0.5 %	
O_2	0.27 %	0.80 %
N_2	Balance	
Ramp rate	10 °C/min	
Max. Temp.	950 °C	

Table 5-2. Reaction conditions

	Lab-scale CO oxidation (St Andrews University)	***NH_3 oxidation*** (Johnson Matthey)	***CO+NO 1:1 reaction*** (Johnson Matthey)	***Diesel oxidation (1)*** (Johnson Matthey)	***Diesel oxidation (2)*** ***we will include this in the paper** (Johnson Matthey)
Gas Mix	CO 20000ppm, O_2 10.0 vol.% from air (21% O_2 and 79% N_2)	NH_3 550ppm, CO 220ppm,	CO 4000ppm, NO 4000ppm	C_3H_6 200ppm, NO 300ppm, CO 1500ppm,	20000ppm in total: CO 1550ppm, H_2O 5%, CO_2 5%,

	-Carrier: N_2 balance	4.5% CO_2, 10% O_2 5%H_2O (steam) -Carrier: N_2 balance	- Carrier: N_2 balance	4.5% CO_2, 10% O_2 5%H_2O (steam) - Carrier: N_2 balance	NO 160 ppm, CH_4 40ppm, propylene C_3H_6 40ppm, Toluene C_7H_8 20ppm, Decane $C_{10}H_{22}$ 30ppm - Carrier: N_2 balance
Flow Rate and GHSV	Total Flow: 200 $ml \cdot min^{-1}$ GHSV: 11 000/hr (assuming 3g/in3 coating)	Flow through catalyst bed: 2L/min GHSV: 110 000/h (assuming 3g/in3 coating)	Flow through catalyst bed:2L/min GHSV: 110 000/h (assuming 3g/in3 coating)	Flow through catalyst bed:2L/min GHSV: 110 000/h (assuming 3 g/in3 coating)	Flow through catalyst bed:2L/min GHSV: 110 000/h (assuming 3 g/in3 coating)
Catalyst amount, diluent and size	200 mg, (220-380 µm)	0.2g with 0.2g of cordierite (250-355 µm)	0.2g with 0.2g of cordierite (250-355 µm)	0.2g with 0.2g of cordierite (250-355 µm)	0.2g, 0.2g of cordierite (250-355 µm)
Temperature range	70-300 ºC	150-330 °C	90-500 °C	150-330 °C	100-500 °C
Ageing furnace used	Static furnace (St Andrews)	Static furnace (JM) with 10% steam	Redox ager (JM) with 10% steam	Static ager (JM) with 10% steam	Static ager (JM) with 10% steam
Analyser used	Gas Chromatography	MKS MG2000 multi-gas analyser using a FT-IR detector	MKS MG2000 multi-gas analyser using a FT-IR detector	MKS MG2000 multi-gas analyser using a FT-IR detector	MKS MG2000 multi-gas analyser using a FT-IR

Oxidation chemistry XANES/EXAFS

In this study, we sampled PT+LCT prepared at varying temperatures of reduction in XANES/EXAFS at the Diamond Light Source synchrotron (UK) near edge spectroscopic environments. A strong trend was observed for Pt+LCT. Lower temperature reduced PT+LCT from 500-600°C had a higher intensity at 16565eV (Figure 5-16), indicating a higher unoccupied density of states of Pt 5d orbital. The higher temperature reduced samples had a lower intensity peak in comparison, indicating a mix of oxidation chemistry and a metallic nature of Pt for Pt^0 . The local electronic structure for reduced Pt-LCT 700°C sits between Pt^0 and Pt^{2+} mix, and EXAFS indicates more Pt-Pt localised bonding than Pt-O for Pt-LCT reduced samples. The difference in bonding structure is a strong indication of SMSI[4,5].

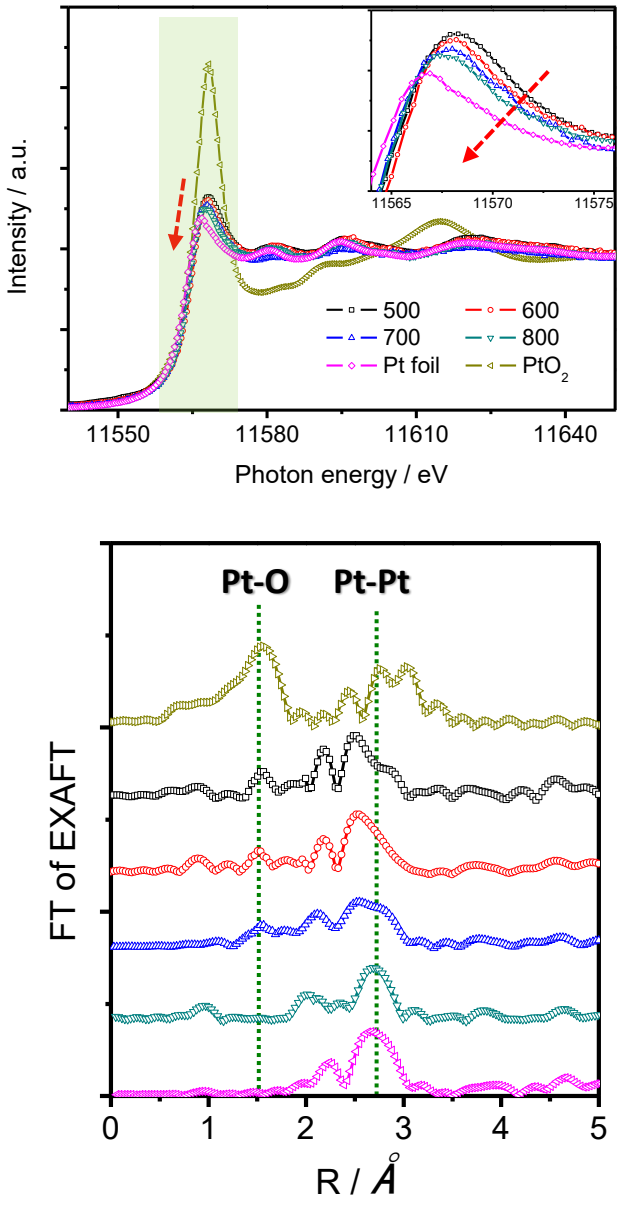

Figure 5-16 shows the XANES above and below the EXAFS spectra for Pt+LCT reduced at various temperatures and the standards including Pt/Al_2O_3.

In-situ diffuse reflectance infrared Fourier transform spectroscopy (DRIFTS)

in situ diffuse reflectance infrared Fourier transform spectroscopy (DRIFTS) was carried out at St Andrews University. Infrared spectroscopy on powdered samples allowed the study of Pt+LCT prepared at temperatures from 500-800 ^{o}C. As the perovskite itself without active Pt^{0} itself acts as a catalyst and the effect of SMSI between the Pt nanoparticles and surface, the basic catalytic mechanism of CO oxidation was studied through in situ-DRIFTS this also allowed the study of Pt+LCT without the addition of KBr, and solely the study of the powder alone. The effect of different particle size differences can be studied by incident IR wave lengths and provide a high resolution spectra.

In situ CO-DRIFTS reaction conditions

Pretreatment at air 450 ^{o}C for 1 hr.

CO+Air (O2) at 100 ^{o}C for CO oxidation. (Resolution of 4 cm^{-1} and 64 scans.)

In-situ DRIFTS was carried out on Pt+LCT for 500,600,700 and 800 ^{o}C reduced samples in 5%H_2Ar for 12 hours to study the effect of Pt nanoparticle size and catalytic properties. The CO adsorption properties, Pt active site identification and the stability were all explored using this technique. The adsorption behavior of CO on the Pt active sites differs from Pt-Al_2O_3. As the temperature of reduction increases from 500-800 ^{o}C (figure 5-17), CO is adsorbed on ionic to metallic Pt, the best catalytically active samples are in between ionic and metallic at 700 ^{o}C. At 800 ^{o}C the adsorption occurs on the Pt metallic phase. The assumption Is the the CO adsorption occurs on the Pt nanoparticles and perovskite which itself is catalytically active. After 800 ^{o}C due to the reduced nature

of the Pt nanoparticles and the perovskite, the adsorption is purely on the metallic phase. The total adsorption for Pt+LCT is slightly higher than that of commercial Pt-Al_2O_3.

The adsorption of CO by time was recorded (figure 5-19) further indicating the absorbance of CO on ionic Pt and metallic Pt for Pt+LCT reduced at 700 ºC. This dual combination can be effective catalytically as both ionic Pt and metallic clusters provide a base for catalytic reactions. The effect of this can be attributed to the emergence of the Pt from the bulk and the effect on SMSI on the ionic Pt.

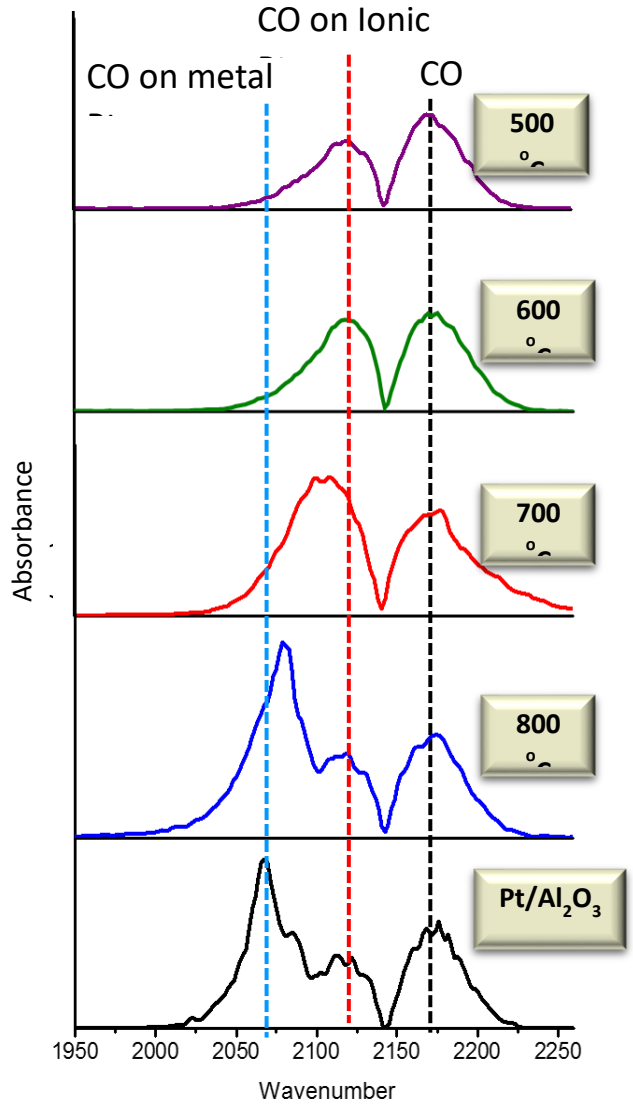

Figure 5-17 shows the FT-IR spectra where CO is bound either to ionic or metallic Pt on Pt+LCT reduced at various temperatures and 0.5 wt% Pt/Al_2O_3.

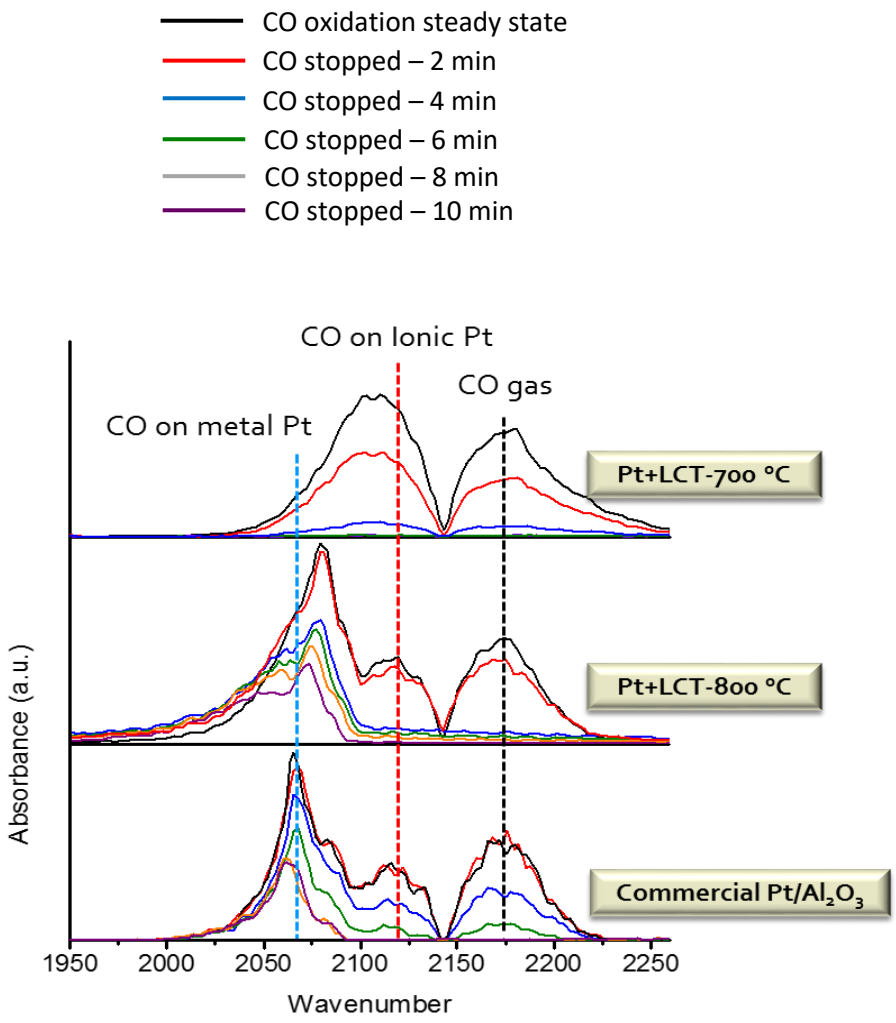

Figure 5-19 shows the adsorption of CO on Pt nanoparticles and the time of which adsorption stopped for Pt+LCT reduced at 700 and 800 °C and 0.5 wt% Pt/Al_2O_3.

Summary and Conclusion

Pt+LCT displayed increased activity over the commercial Pt/Al2O3 commercial equivalent at moderate conditions. The rate of reaction itself was higher when considering the low surface area of Pt+LCT itself. Interestingly the mixed oxide support showed oxygen storage properties that aided in catalytic oxidation of CO.

The perovskite system although not porous and non-amorphous displayed catalytically favorable results in all tests and ageing conditions. The space velocities ran in all industrial settings are in line with commercial testing at Johnson Matthey and stand up to the commercial equivalent in autocatalytic systems. The selectivity of NO compared with N_2O at lower temperatures (400°C) is favorable due in part to the environmental consequences of N_2O. The stability of Pt+LCT reduced at various temperatures can be observed via the SEM micrographs and catalytic activity combined. The operational lifetime of Pt+LCT withstands typical degradation mechanisms including oxidation in both perturbed and non-perturbed environments leading to stabilized Pt nanoparticles with a SMSI (Strong metallic support interaction toward the perovskite mixed oxide surface). Poisoning and coking of the Pt NP's in the presence of Sulphur is non existent, the Pt+LCT activity does not reduce. However there is a strong poisoning affinity of C10 toward the perovskite surface and this must be noted if Pt+LCT is to be implemented in diesel autocatalytic converters. The strength of the catalyst and size is selective for the oxidation and reduction of both CO and NH_3. The size of Pt+LCT NP's does not reduce over time and this is attributed to the SMSI effect and embedded nature of the nanoparticles.

In conclusion the Pt+LCT system is robust and shows great promise as an alternative for Pt/Al_2O_3 and other autocatalytic additives. The system can be improved significantly through porosity control and NP reduction temperatures.

References

1. Galassi, G. & Spada, G. Sea-level rise in the Mediterranean Sea by 2050: Roles of terrestrial ice melt, steric effects and glacial isostatic adjustment. *Glob. Planet. Change* **123**, 55–66 (2014).
2. Rowley, R. J., Kostelnick, J. C., Braaten, D., Li, X. & Meisel, J. Risk of Rising Sea Level to Population and Land Area. *Eos, Trans. Am. Geophys. Union* **88**, 105 (2007).
3. Alley, R. B., Clark, P. U., Huybrechts, P. & Joughin, I. Ice-sheet and sea-level changes. *Science* **310**, 456–60 (2005).
4. Cox, P. M., Betts, R. A., Jones, C. D., Spall, S. A. & Totterdell, I. J. Acceleration of global warming due to carbon-cycle feedbacks in a coupled climate model. *Nature* **408**, 184–187 (2000).
5. Corma, A. & López Nieto, J. M. *The Role of Rare Earths in Catalysis*. *Handbook on the Physics and Chemistry of Rare Earths* **29**, (Elsevier, 2000).
6. BY se G. le. 3–5 (1973).
7. Cohn, J. G. Catalytic converters for exhaust emission control of commercial equipment powered by internal combustion engines. *Environ. Health Perspect.* **10**, 159–164 (1975).
8. Farrauto, R. J., Deeba, M. & Alerasool, S. journey to cleaner air. *Nat. Catal.* **2**, 603–613 (2021).
9. Eastwood, P. *Critical topics in exhaust gas aftertreatment*. (Research Studies Press, 2000).
10. Summers, J. C., Sawyer, J. E. & Frost, A. C. The 1990 Clean Air Act and Catalytic Emission Control Technology for Stationary Sources. in *Catalytic Control of Air Pollution* **495**, 8–98 (American Chemical Society, 1992).
11. Libby, W. F. Promising Catalyst for Auto Exhaust. *Science (80-.).* **171**, 499–500 (1971).
12. Twigg, M. V. Progress and future challenges in controlling automotive exhaust gas emissions. *Appl. Catal. B Environ.* **70**, 2–15 (2007).
13. Russell, A., Epling, W. S., Russell, A. & Epling, W. S. Diesel Oxidation Catalysts Diesel Oxidation Catalysts. **4940**, (2011).
14. Twigg, M. V. Catalytic control of emissions from cars. *Catal. Today* **163**, 33–41 (2011).
15. Matthey, J. Johnson Matthey Annual Report 2018 - customers. (2018).
16. Misono, M. Mixed Oxides as Catalyst Supports. **176**, 157–173 (2013).
17. Tanaka, H. & Misono, M. Advances in designing perovskite catalysts. *Curr. Opin. Solid State Mater.* (2001).
18. Tanaka, H. *et al.* Design of the intelligent catalyst for Japan ULEV standard. *Top. Catal.* **30/31**, 389–396 (2004).
19. Screen, T. Platinum Group Metal Perovskite Catalysts. *Platin. Met. Rev.* **51**, 87–92 (2007).
20. Russell, A. & Epling, W. S. Diesel Oxidation Catalysts. *Catal. Rev.* **53**, 337–423 (2011).
21. Kröcher, O. *et al.* Investigation of the selective catalytic reduction of NO by NH3 on Fe-ZSM5 monolith catalysts. *Appl. Catal. B Environ.* **66**, 208–216 (2006).
22. Prasad, D. H. *et al.* Effect of nickel nano-particle sintering on methane reforming activity of Ni-CGO cermet anodes for internal steam reforming SOFCs. *Appl. Catal. B Environ.* **101**, 531–539 (2011).
23. Prasad, D. H. *et al.* Effect of steam content on nickel nano-particle sintering and methane reforming activity of Ni–CZO anode cermets for internal reforming SOFCs. *Appl. Catal. A Gen.* **411**–**412**, 160–169 (2012).
24. Deng, J., Cai, M., Sun, W., Liao, X. & Chu, W. Oxidative Methane Reforming with an Intelligent Catalyst: Sintering-Tolerant Supported Nickel Nanoparticles. (2013).
25. Nishihata, Y. *et al.* Self-regeneration of a Pd-perovskite catalyst for automotive emissions

control. *Nature* **418**, 164–167 (2002).
26. Tanaka, H. *et al.* An intelligent catalyst. -*SOCIETY Automot. Eng. JAPAN* (2001).
27. Kajita, N., Uenishi, M., Tan, I., Tanaka, H. & Kimura, M. Regeneration of Precious Metals in Various Designed Intelligent Perovskite Catalysts. (2002).
28. Sato, N., Tanaka, H., Tan, I., Uenishi, M. & Kajita, N. Design of a practical Intelligent catalyst. *SAE Trans.* (2003).
29. Nishihata, Y., Mizuki, J., Tanaka, H., Uenishi, M. & Kimura, M. Self-regeneration of palladium-perovskite catalysts in modern automobiles. in *Journal of Physics and Chemistry of Solids* (2005). doi:10.1016/j.jpcs.2004.06.090
30. Tanaka, H. An intelligent catalyst: the self-regenerative palladium–perovskite catalyst for automotive emissions control. *Catal. Surv. from Asia* (2005).
31. Uenishi, M., Tanaka, H., Taniguchi, M., Tan, I. & Sakamoto, Y. The reducing capability of palladium segregated from perovskite-type LaFePdO x automotive catalysts. *Appl. Catal. A* (2005).
32. Nishihata, Y., Mizuki, J., Tanaka, H. & Uenishi, M. Self-regeneration of palladium-perovskite catalysts in modern automobiles. *J. Phys.* (2005).
33. Tanaka, H., Tan, I., Uenishi, M., Taniguchi, M. & Nishihata, Y. The Intelligent Catalyst: Pd-Perovskite Having the Self-Regenerative Function in a Wide Temperature Range. *Key Eng. Mater.* (2006).
34. Taniguchi, M. *et al.* The self-regenerative Pd-, Rh-, and Pt-perovskite catalysts. in *Topics in Catalysis* (2007). doi:10.1007/s11244-007-0207-x
35. Taniguchi, M., Uenishi, M., Tan, I., Tanaka, H. & Kimura, M. Thermal Properties of the Intelligent Catalyst. (2004).
36. Tanaka, H. *et al.* Self-Regenerating Rh- and Pt-Based Perovskite Catalysts for Automotive-Emissions Control. *Angew. Chemie Int. Ed.* **45**, 5998–6002 (2006).
37. Hamada, I., Uozumi, A., Morikawa, Y., Yanase, A. & Katayama-Yoshida, H. A density functional theory study of self-regenerating catalysts LaFe1-xMxO3-y(M = Pd, Rh, Pt). *J. Am. Chem. Soc.* **133**, 18506–18509 (2011).
38. Tanaka, H. & Kaneko, K. Method for producing perovskite-type composite oxide. *US Pat. 7,381,394* (2008).
39. Katz, M. B. *et al.* Reversible precipitation/dissolution of precious-metal clusters in perovskite-based catalyst materials: Bulk versus surface re-dispersion. *J. Catal.* **293**, 145–148 (2012).
40. Malamis, S. A. *et al.* Comparison of precious metal doped and impregnated perovskite oxides for TWC application. *Catal. Today* **258**, 535–542 (2015).
41. Katz, M. Advanced Transmission Electron Microscopy Studies of Induced Interactions of Metallic Species with Perovskite Oxide Hosts. (2013).
42. Jarrige, I. *et al.* Toward optimizing the performance of self-regenerating Pt-based perovskite catalysts. *ACS Catal.* **5**, 1112–1118 (2015).
43. Hazen, R. M. Perovskites. *Scientific American* **258**, 74–81 (1988).
44. Keav, S., Matam, S., Ferri, D. & Weidenkaff, A. Structured Perovskite-Based Catalysts and Their Application as Three-Way Catalytic Converters—A Review. *Catalysts* **4**, 226–255 (2014).
45. Tejuca, L. G., Fierro, J. L. G. & Tascón, J. M. D. Structure and Reactivity of Perovskite-Type Oxides. *Adv. Catal.* **36**, 237–328 (1989).
46. Neagu, D. Materials and Microstructures for High Temperature Electrochemical Devices through Control of Perovskite Defect Chemistry Dragos Neagu. 1–257 (2012).
47. Goldschmidt, V. M. Die gesetze der krystallochemie. (1926).
48. Peña, M. A. & and J. L. G. Fierro*. Chemical Structures and Performance of Perovskite Oxides. *Chem. Rev.* **101**, 1981–2018 (2001).
49. Chynoweth, A. G. {\it Ferroelectricity in crystals} by H. D. Megaw. *Acta Crystallogr.* **11**, 754–755 (1958).
50. Allan, N. L., Dayer, M. J., Kulp, D. T. & Mackrodt, W. C. Atomistic lattice simulations of the ternary fluorides AMF3(A = Li, Na, K, Rb, Cs; M = Mg, Ca, Sr, Ba). *J. Mater. Chem.* **1**,

1035–1039 (1991).
51. Neagu, D. & Irvine, J. T. S. *Perovskite Defect Chemistry as Exemplified by Strontium Titanate*. *Comprehensive Inorganic Chemistry II* (Elsevier Ltd., 2013). doi:10.1016/B978-0-08-097774-4.00421-6
52. Duprez, D. *et al.* Perovskites as Substitutes of Noble Metals for Heterogeneous Catalysis : Dream or Reality Se b. *Chem. Rev.* **114**, 10292 (2014).
53. Shannon, R. D. Revised effective ionic radii and systematic studies of interatomic distances in halides and chalcogenides. *Acta Crystallogr. Sect. A* **32**, 751–767 (1976).
54. Neagu, D., Tsekouras, G., Miller, D. & Ménard, H. In situ growth of nanoparticles through control of non-stoichiometry. *Nat. Chem.* (2013).
55. Neagu, D. & Irvine, J. T. S. Enhancing electronic conductivity in strontium titanates through correlated A and B-site doping. *Chem. Mater.* **23**, 1607–1617 (2011).
56. Oh, T., Rahani, E., Neagu, D. & Irvine, J. Evidence and Model for Strain-Driven Release of Metal Nanocatalysts from Perovskites during Exsolution. *J.* (2015).
57. Zhu, Y. *et al.* Promotion of oxygen reduction by exsolved silver nanoparticles on a perovskite scaffold for low-temperature solid oxide fuel cells. *Nano Lett.* (2015).
58. Liu, S., Chuang, K. & Luo, J. Double layered perovskite anode with in-situ exsolution of Co-Fe alloy to cogenerate ethylene and electricity in proton conducting ethane fuel cell. *ACS Catal.* (2015).
59. Tsvetkov, D., Ivanov, I. & Malyshkin, D. Oxygen content, cobalt oxide exsolution and defect structure of the double perovskite PrBaCo 2 O 6− δ. *J. Mater.* (2016).
60. Thalinger, R., Gocyla, M. & Heggen, M. Ni–perovskite interaction and its structural and catalytic consequences in methane steam reforming and methanation reactions. *J.* (2016).
61. Miller, E. Synthesis, Characterization, and Optimization of Novel Solid Oxide Fuel Cell Anodes. (2015).
62. Liu, S., Chuang, K. & Luo, J. Erratum to “Double Layered Perovskite Anode with in Situ Exsolution of Co–Fe Alloy To Cogenerate Ethylene and Electricity in Proton-Conducting Ethane Fuel Cell”. *ACS Catal.* (2016).
63. Armor, J. N. A history of industrial catalysis. *Catal. Today* **163**, 3–9 (2011).
64. Voorhoeve, R. J. H., Remeika, J. P. & Johnson, D. W. Rare-Earth Manganites: Catalysts with Low Ammonia Yield in the Reduction of Nitrogen Oxides. *Science (80-.).* **180**, 62–64 (1973).
65. Gallagher, P. K., Johnson, D. W. & Schrey, F. Studies of some supported perovskite oxidation catalysts. *Mater. Res. Bull.* **9**, 1345–1352 (1974).
66. Bravo-Suárez, J. J., Chaudhari, R. V & Subramaniam, B. Design of Heterogeneous Catalysts for Fuels and Chemicals Processing: An Overview. in *Novel Materials for Catalysis and Fuels Processing* 3–68 doi:10.1021/bk-2013-1132.ch001
67. Misono, M. Catalysis of Perovskite and Related Mixed Oxides. *Stud. Surf. Sci. Catal.* **176**, 67–95 (2013).
68. Neagu, D., Oh, T., Miller, D., Ménard, H. & Bukhari, S. Nano-socketed nickel particles with enhanced coking resistance grown in situ by redox exsolution. *Nat. Commun.* (2015).
69. Xu, S. *et al.* Perovskite chromates cathode with resolved and anchored nickel nano-particles for direct high-temperature steam electrolysis. *J. Power Sources* (2014).
70. Tsekouras, G., Neagu, D. & Irvine, J. Step-change in high temperature steam electrolysis performance of perovskite oxide cathodes with exsolution of B-site dopants. *Energy Environ. Sci.* (2013).
71. Li, Y., Wang, Y., Doherty, W., Xie, K. & Wu, Y. Perovskite chromates cathode with exsolved iron nanoparticles for direct high-temperature steam electrolysis. (2013).
72. Sun, Y., Li, J., Zeng, Y., Amirkhiz, B. & Wang, M. A-site deficient perovskite: the parent for in situ exsolution of highly active, regenerable nano-particles as SOFC anodes. *J. Mater.* (2015).
73. Prabha, I. Current Status of Platinum Based Nanoparticles : Physicochemical Properties and Selected Applications – A Review. 122–133 (2019).
74. Da, Y. *et al.* Catalytic oxidation of diesel soot particulates over Pt substituted LaMn 1-x Pt x O

3 perovskite oxides. *Catal. Today* **327**, 73–80 (2019).
75. Li, X. *et al.* In situ exsolution of PdO nanoparticles from non-stoichiometric LaFePd0.05O3+Δ electrode for impedancemetric NO2 sensor. *Sensors Actuators, B Chem.* **298**, (2019).
76. Gao, Y. *et al.* Energetics of Nanoparticle Exsolution from Perovskite Oxides. *J. Phys. Chem. Lett.* **9**, 3772–3778 (2018).
77. Fang, C. *et al.* Highly Dispersed Pt Species with Excellent Stability and Catalytic Performance by Reducing a Perovskite-Type Oxide Precursor for CO Oxidation. *Trans. Tianjin Univ.* **24**, 547–554 (2018).
78. Fierro, J. L. G. Chemical Structures and Performance of Perovskite Oxides. (2017).
79. Zhang, S. In-situ and Ex-situ Microscopy and Spectroscopy Study of Catalytic Materials by. 217 (2017).
80. Glazer, A. M. The classification of tilted octahedra in perovskites. *Acta Crystallogr. Sect. B* **28**, 3384–3392 (1972).
81. Howard, C. J. & Stokes, H. T. Group-Theoretical Analysis of Octahedral Tilting in Perovskites. *Acta Crystallogr. Sect. B* **54**, 782–789 (1998).
82. Neagu, D., Tsekouras, G., Miller, D. D. N., Ménard, H. & Irvine, J. T. S. In situ growth of nanoparticles through control of non-stoichiometry. *Nat. Chem.* **5**, 916–923 (2013).
83. G. ROUSSEAU. No Title. *Acad. Sci. Paris* **109**, 144 (1889).
84. Statton, W. O. The phase diagram of the BaO-TiO2system. *J. Chem. Phys.* **19**, 33–40 (1951).
85. Randall, J. J. & Ward, R. The Preparation of Some Ternary Oxides of the Platinum Metals. *J. Am. Chem. Soc.* **81**, 2629–2631 (1959).
86. Haradem, P. S., Chamberland, B. L., Katz, L. & Gleizes, A. A structural model for barium platinum oxide, Ba3Pt2O7. *J. Solid State Chem.* **21**, 217–223 (1977).
87. Chaston, J. C. Reactions of Oxygen with the Platinum Metals; II-OXIDATION OF RUTHENIUM, RHODIUM, IRIDIUM AND OSMIUM. *Platin. Met. Rev.* **9**, 51–56 (1965).
88. Sharma, P. A., Brown-Shaklee, H. J. & Ihlefeld, J. F. Oxygen partial pressure dependence of thermoelectric power factor in polycrystalline n-type SrTiO3: Consequences for long term stability in thermoelectric oxides. *Appl. Phys. Lett.* **110**, (2017).
89. Kuklja, M. M., Mastrikov, Y. A., Jansang, B. & Kotomin, E. A. The intrinsic defects, disordering, and structural stability of Ba xSr 1-xCo yFe 1-yO 3-δ perovskite solid solutions. *J. Phys. Chem. C* **116**, 18605–18611 (2012).
90. Nur, A. S. M. *et al.* Phase-Dependent Formation of Coherent Interface Structure between PtO2 and TiO2 and Its Impact on Thermal Decomposition Behavior. *J. Phys. Chem. C* **122**, 662–669 (2018).

FINAL SUMMARY AND CONCLUSION

In this body of work an all-encompassing area of study was conducted from synthesis, characterisation, catalytic testing and validation in real conditions. From the off Pt has always been a very difficult element to tame. Tanaka et al (Daihatsu) method of intelligent catalyst upon redox prepared by sol-gel methods have been disproven by M.B Katz and even in this work, combustion synthesis of Pt+LCT revealed a impure and in-stable catalyst. The demonstration of Platinum for the first time being fully incorporated within a single crystal structure, synthesised at high temperature and cation tailoring to produce a system which competes with the commercial equivalent. From the catalyst perspective, looking from a traditional standpoint one could argue that a low surface area, high synthesis temperatures and difficult cation tailoring system will mean commercial failure. However considering the overwhelming ability of Pt+LCT to outperform Pt/Al_2O_3 in each commercial test it can be noted that significant improvement to the catalysts microstructure and porosity may further increase its catalytic ability. Furthermore, the sintering resistance and stability of Pt nano particles that has plague the autocatalysis community for years to provide a material that can last and perform consistently withstanding to the effects of sintering, agglomeration of active NP's has resulted in Pt+LCT displaying advantageous characteristics to meet that criteria and displaying anti-ageing characteristics with NP stabilisation, SMSI (strong metallic support interaction with the perovskite mixed oxide) a embeddedness of the Pt nanoparticles and a sintering resistance during high temperature events has resulted in a 'immortal active catalyst'.

The oxidation chemistry of the Pt nanoparticles is very significant, enabling a strong support interaction after a reduction event over 700°C to remain Pt^0. Importantly PtO_2 is not prevalent after re-oxidation.

In conclusion, we demonstrate a new approach of using a Trojan horse modified synthesis environment which has offered a perfect Pt incorporation into the perovskite structure via solid-state synthesis. Active and stable emergent Pt NPs anchored on the surface were developed, which shows a highly catalytically active configuration and is immune to the typical effects of agglomeration through a strong interaction with the bulk perovskite structure, demonstrating great potential for use in a wide variety of

catalytic reaction systems. The tailoring of the crystallinity of A-site deficient perovskite is incredibly important in order to incorporate ‘difficult’ cations (Platinum) into the structure. By creating a single crystal perovskite, the crystal structure can be studied carefully along with catalytic activity providing two modes of chemical and material characterisation combined. The range of Platinate precursors can also be further explored to evolve this line of cation incorporation chemistry. Furthermore, tailored reduction chemistry along with careful study of nanoparticle interaction through oxidation state characterisation can provide a deeper insight into the complex metal-host interaction the perovskite plays with active nanoparticles enabling more applications through rational design of combined metallic and ionic Platinum nanoparticles.

The body of this work has shown full novelty in developing a Pt perovskite that is initially fully incorporated into the crystal structure and then, upon reduction, produced well dispersed nanoparticles on the surface with strong metallic support interactions and varying oxidation chemistry in comparison to typical automotive catalysis. Despite the low surface area, Pt+LCT is comparable and better in some cases than the commercial equivalent. This combination of catalytic behaviour and material development warrants further study and possible commercialisation.

Future work includes tailoring the wt% of Pt and working on porosity through pore formers such as PMMA or glassy carbon. The incorporation of Pd has also started with promising results. Issues surrounding scale up have been discussed extensively with Johnson Matthey, one way around that is the dry and wet palletisation methods typical in the pharmaceutical industry however the cost of this is extremely expensive and therefore real scale up should be thought about carefully.

For use in tailored systems such as ultra-long life catalytic scrubbers and long-haul freight Pt+LCT as a replacement material for Pt/Al_2O_3 should be considered due to its anti ageing a sintering resistance.

There is a long way to go in this work, we have just touched the surface...

FIGURES

CHAPTER 1 BACKGROUND

CHAPTER 2 METHOD

CHAPTER 3 CRYSTAL STRUCTURE

Chapter 4 MICROSTRUCTURE

CHAPTER 5 OXIDATION AND CATALYSIS

TABLES

CHAPTER 1 BACKGROUND

CHAPTER 3 CRYSTAL STRUCTURE

Chapter 4 MICROSTRUCTURE

CHAPTER 5 OXIDATION AND CATALYSIS